JAGIELLONIAN
UNIVERSITY
IN KRAKOW

UNIVERSITÉ DE STRASBOURG

Thèse
présentée pour obtenir le grade de

Docteur de l'Université de Strasbourg
et
Docteur de l'Université Jagellonne de Cracovie

SPÉCIALITÉ : Physique de la matière condensée
École Doctorale UdS 182 - Physique et chimie physique

par

Łukasz Zosiak

Simulations of atomic and electronic structure of realistic Co and Pt based nanoalloy clusters

Simulations des structures atomique et électronique de nanoparticules d'alliage à base de cobalt et platine

---

Directrice de thèse	**Christine Goyhenex** Université de Strasbourg, Strasbourg, France
Directeur de thèse	**Rafał Kozubski** Jagiellonian University, Cracovie, Pologne
Rapporteur	**Christine Mottet** Aix-Marseille Université, Marseille, France
Rapporteur	**Jacek Majewski** Warsaw University, Varsovie, Pologne
Examinateur	**Józef Spałek** Jagiellonian University, Cracovie, Pologne
Examinateur	**Helena Zapolsky** Université de Rouen, Rouen, France

Soutenue à Cracovie le 30 septembre 2013.

Contents

Contents iii

List of Tables v

List of Figures vii

Acknowledgements xiii

Introduction 1

1 Methodology 7
- 1.1 First principles approach 7
  - 1.1.1 Hamiltonian of many-body system 7
  - 1.1.2 Density Functional Theory 9
  - 1.1.3 Approximations of the exchange-correlation functional 10
  - 1.1.4 Kohn-Sham equations 12
  - 1.1.5 Basis sets 13
  - 1.1.6 Pseudopotentials 15
  - 1.1.7 Deployment of the SIESTA method 18
- 1.2 Tight Binding approach 25
  - 1.2.1 The Tight-Binding Hamiltonian 25
  - 1.2.2 Calculation of the Local Density Of States 29
  - 1.2.3 LDOS of inhomogeneous systems 32
- 1.3 Inequivalent site classification 35

2 DFT calculations of pure systems 37
- 2.1 Elemental bulk systems 37
  - 2.1.1 Basic properties 37
  - 2.1.2 Charge redistribution analysis 40
  - 2.1.3 Band structure and the density of states 40
- 2.2 Low-coordinated systems: pure surfaces 40
  - 2.2.1 The surface energy 42
  - 2.2.2 Charge redistribution: towards the neutrality rule 43
  - 2.2.3 Density of states on surface sites 44
- 2.3 Finite size systems: pure platinum clusters 45
  - 2.3.1 Cluster configuration 45
  - 2.3.2 Energetically favored structures 46
  - 2.3.3 Charge redistribution on surfaces, edges and vertices 47
  - 2.3.4 Density of states on clusters 47
- 2.4 Conclusions 49

3 DFT calculations of mixed systems **51**
3.1 Mixed Co-Pt bulk systems 52
3.1.1 Basic properties 52
3.1.2 Magnetism and phase stability in CoPt alloys 54
3.1.3 Charge redistribution in modified chemical environment 56
3.1.4 Local magnetic properties *vs* chemical environment 60
3.1.5 Evolution of densities of states with chemical environment 62
3.2 Surfaces and thin films: the case of Co monolayer 66
3.2.1 Energetics 66
3.2.2 Charge analysis and local magnetic properties 68
3.2.3 Densities of states 70
3.3 Nanoalloys: cuboctahedral and icosahedral clusters 71
3.3.1 Charge analysis and local magnetic properties 72
3.4 Conclusions 72

4 TBA calculations of realistic systems **75**
4.1 Additional features for the use of tight-binding 75
4.2 Compatibility of the TBA and DFT results 78
4.2.1 Comparison of relative stability energies 78
4.2.2 Direct comparison of the densities of state 79
4.3 Mixed clusters: analysis of d-band position and width 82
4.4 Ordering trends in nanoalloys 87
4.5 Conclusions 89

5 General conclusions and perspectives **91**

Bibliography **95**

List of Tables

2.1 Comparison of the properties of pure fcc platinum obtained in the present work (GGA-SIESTA), calculated with LDA (SIESTA code) [1], GGA (VASP code) [2] and experimental values [3]. 38
2.2 Comparison of the properties of pure fcc cobalt obtained in the present work (SIESTA-GGA), calculated with LDA [2], hybrid LDA-GGA [4], GGA [2] and experimental values [5, 6, 7]: lattice parameter a [Å], cohesion energy $\mathrm{E_{coh}}$ [eV/atom], bulk modulus B [GPa] and spin magnetic moment μ [μ_B/atom]. 38
2.3 Comparison of the properties of pure hcp cobalt obtained in the present work with SIESTA-GGA, calculated with LDA [2], hybrid LDA-GGA [4], GGA [2] and experimental values [5, 3, 7]: lattice parameters a and c [Å], cohesion energy $\mathrm{E_{coh}}$ [eV/atom], bulk modulus B [GPa] and spin magnetic moment μ [μ_B/atom]. 38
2.4 Comparison of the charge distribution between orbitals in the case of an isolated atom and an atom inside an infinite bulk. Total site charge is given in the last column. 40
2.5 Surface energies of Pt(100), Pt(111) (nonmagnetic) and Co(0001) (magnetic) surfaces calculated in the supercell scheme with 6-layer slab. . . . 42
2.6 Comparison of the charge distribution between orbitals on the surface sites and the interior of the slab for different surface orientations. 43
2.7 Summary of the calculated cluster geometries. The table indicates, for the two considered shapes, the total number of (100) and (111) facets, edges and vertices. 46
2.8 Comparison of the charge distribution between orbitals inside the Pt cluster and on particular surface sites along with the site coordination Z. The results were obtained for a cluster of 561 atoms by averaging over all the equivalent sites (with the same coordination number). . . . 48

3.1 Comparison of calculated properties of $\mathrm{L1_0}$ CoPt and those measured experimentally. Lattice constants a enclosed in parentheses have been calculated in case of no tetragonal distortion (with assumption that $c/a = 1$). 53
3.2 Comparison of calculated properties of $\mathrm{L1_2}$ $\mathrm{Co_3Pt}$ and experimental data. 53
3.3 Comparison of calculated properties of $\mathrm{L1_2}$ $\mathrm{CoPt_3}$ and experimental data. 53
3.4 Charge distribution between orbitals on **cobalt** bulk sites. 57
3.5 Charge distribution between orbitals on **platinum** bulk sites. 58
3.6 Comparison of site charges calculated with different methods. 60

4.1 Relative stability energy ΔE_{stab} (eV/atom) between several bulk CoPt ordered alloys at different concentrations. DFT calculations were performed with (magnetic) and without (non magnetic) spin polarization. . 78

List of Figures

1 High-temperature magnetic and chemical phase diagram of the CoPt system [8]. Example L1_2 (Co$_3$Pt, CoPt$_3$) and L1_0 (CoPt) structures are shown below. 3

1.1 Self-consistent algorithm for solution of Kohn-Sham equations [9]. . . . 14

1.2 Schematic representation of the pseudopotential and valence pseudo wavefunction (dashed line) versus all electron potential and true wavefunction (solid line). 17

1.3 Visualization of all-electron (AE) wavefunctions and pseudo-wavefunctions (PS) as a function of radius (Bohr) for each orbital. One can observe that below cut-off radius (dashed line) AE wavefunction has nodes that vanish in PS case while above cut-off both functions are identical. 20

1.4 Comparison of orbital energies calculated with pseudopotential and those obtained from all-electron calculation. Differences are negligible (less than 0.5 mRy). 21

1.5 Example of basis fine-tuning. Calculation of pure platinum (fcc) lattice constant for bases generated with different orbital-confining cutoff radii. 21

1.6 Example of lattice constant calculation in case of pure fcc platinum and total energy surfaces for a range of a and c lattice constants in case of $L1_0$ CoPt. 22

1.7 Example analysis of the impact of two critical parameters: mesh cut-off and k-grid cut-off [10] on the total energy of CoPt magnetic bulk system (vertical solid lines mark the choice made for the purpose of further calculations). 25

1.8 Visualization of the possible symmetric hopping integrals between two s, p and sp orbitals (first row), d orbitals (second row) and sd, pd orbitals (last row) [1]. 28

1.9 Construction of the recursion cluster for the fcc structure (cross-section). The number of coefficients and the size of the recursion cluster are directly related to the first moments approximation. Within the Second Moment Approximation the LDOS on a given site (a) depends only on its first neighbors (b). For the Fourth- and further Moment Approximations more recursion shells need to be considered (c,d). 31

1.10 The self-consistent algorithm for LDOS determination on sites whose local environment differs from bulk. 34

1.11 In a pure bulk system all sites are equivalent (left) with atomic level ε_0. Atomic levels of surface sites (right) are shifted by $\delta\varepsilon$ due to the lower coordination. 34

1.12 Sample classification of the sites in the case of cuboctahedral fcc cluster: topological classification of sites based on the coordination Z_i numbers (left, each color corresponds to a different class) and site occupancy for binary $A - B$ $\mathrm{L1}_0$ ordered alloy (right, each color corresponds to a different atom type). The combination of those two factors give the full classification of inequivalent sites in the system (e.g. platinum site on mixed, (100) surface is classified with parameters $Z_i = 8$, $M_i = 6$, $X_i = \mathrm{Pt}$). 35

2.1 Total energy per atom for ferromagnetic (filled circles) and paramagnetic (hollow circles) fcc Co relative to the minimum energy of ferromagnetic case (left) and magnetic moment (filled squares) with respect to the unit cell volume. 39

2.2 Band structure of Pt (fcc), Co (fcc) and Co (hcp) at high-symmetry points. 41

2.3 Projected d-band density of states of pure platinum (fcc - nonmagnetic) and cobalt (fcc, hcp - magnetic). Energies are shifted by respective Fermi levels E_F. 41

2.4 Pure surface calculations: a) the supercell scheme b) the surface layer distance optimization (example result for Pt(100) slab of 10 atomic layers, ~ 1.8 nm). 42

2.5 In-depth charge redistribution analysis in the Pt(100) case: a) charge redistribution profile along the axis perpendicular to the surface, y axis represents the difference between the orbital/site charge q on a given site and the corresponding bulk value q_0; the red (blue) region marks the surface (bulk) sites. The lines are arbitrarily fitted eye-guides; b) charge changes on the surface layer with respect to its distance from the slab - in all cases the charge redistribution is negligibly small. 44

2.6 Projected d-band density of states of pure platinum and cobalt surfaces, dashed line represents bulk LDOS. Energies are shifted by respective Fermi levels E_F. 45

2.7 Low-coordinated sites in cuboctahedral and icosahedral clusters: (111) surfaces ($Z = 9$), (100) surfaces ($Z = 8$), edges ($Z = 7, 8$) and vertices ($Z = 5, 6$). 46

2.8 a) Total energy per atom of a Pt cluster (normalized to the analogous energy in bulk as a function of size b) Charge redistribution on the low-coordinated cluster sites as a function of the site coordination number for d orbitals (squares connected with solid lines) and $s + p$ orbitals (circles connected with dashed lines) for cuboctahedral (red) and icosahedral (blue) clusters. Black lines correspond to the reference bulk values. The result was obtained for a cluster of 561 atoms by averaging over all the equivalent sites (with the same coordination number). 47

2.9 Total site charge variation profile with respect to bulk for a) cuboctahedra b) icosahedra (cross section, the gray scale corresponds to the amount of charge from -3% (white) to +3% (black) of bulk value. The charge redistribution follows scheme observed in case of surfaces - there is small charge transfer from surface sites (lighter) towards lower atomic layers (darker). The charge inside cluster is not modified (gray). 48

2.10 Projected *d*-band density of states on various low-coordinated sites on pure platinum clusters. Energies are shifted by respective Fermi levels E_F. 49

3.1 Unit cells of ordered Co-Pt alloys studied in the present work. 52

3.2 Supercell geometries used for calculations of diluted systems. N denotes the total number of atoms in the supercell of volume V and C is the concentration of impurities. Supercell dimensions along x, y and z-axis are given in unit cells (4 atoms). 53

3.3 Comparison of total energies as a function of unit cell volume for: L1_2 Co$_3$Pt (left), L1_0 CoPt (center) and L1_2 Co$_3$Pt (right). Differences between minima corresponding to paramagnetic (red) and ferromagnetic (blue) calculations are marked. 54

3.4 Heats of formation of Co-Pt systems with respect to cobalt concentration. 55

3.5 Comparison of s+p (blue) and d (green) orbital charges calculated with Mulliken method on cobalt (left) and platinum sites (right) for paramagnetic systems of different cobalt concentration (and, therefore, site mixing rank). 58

3.6 Comparison of s+p (blue) and d (green) orbital charges calculated with Mulliken method on cobalt (left) and platinum sites (right) for ferromagnetic systems of different cobalt concentration (and, therefore, site mixing rank). 59

3.7 Comparison of charges on cobalt (dashed) and platinum (solid) sites calculated with Mulliken method (cyan) and from charge density with Bader (red) and Voronoi (black) approach for paramagnetic systems of different Co concentration (left). Bader volume associated with each site type as unit cell fraction with respect to cobalt concentration is also shown (right). 59

3.8 Comparison of the Mulliken total (circles) and d-orbital (squares) charges (left plot) and local magnetic moments (right plot) with respect to the site mixing rank for platinum (red) and cobalt (blue) sites. This is the average calculated over all bulk sites of all samples within CoPt slabs of different order parameter ranging from 0 to 1. Respective pure bulk values are marked with horizontal lines (dashed for d-orbital). 61

3.9 Average magnetic moments of Pt atoms (red), Co atoms (blue) and total magnetic moment (green) in mixed systems with respect to cobalt concentration (left). Two smaller plots on the right show d (upper) and s+p (lower) contributions. 62

3.10 Average magnetic moment on Pt (red) and Co (blue) atoms in the dilute system system with, respectively, one Co or Pt impurity atom - d orbital (left) and s+p orbitals contributions (right). Solid lines correspond to the values for pure bulk. 63
3.11 Local density of states (d band, paramagnetic case) of neighboring cobalt (blue) and platinum (red) sites. For comparison the corresponding pure element bulk LDOS are shown on the upper left plot. 64
3.12 Local density of states (d band, ferromagnetic case) of neighboring cobalt (blue) and platinum (red) sites. For comparison the corresponding pure element bulk LDOS are shown on the upper left plot. 65
3.13 Electronic structure in diluted systems ($M_i = 12$). Local density of states (d band) on the impurity atom for various supercell sizes denoted by color intensity (47+1, 71+1 and 107+1 atoms). $L1_0$ CoPt LDOS is shown for comparison (dots). 66
3.14 Co (purple) monolayer on top of Pt(111) surface with stacking variants: fcc (left), hcp (center) on-top (right). Fragment of (111) surface and slab cross-section. 67
3.15 Co monolayer adsorption energy with respect to the Pt(111) slab thickness in ferromagnetic (circles) and paramagnetic (squares) case. Dashed line corresponds to the mean value. Results for fcc (blue), hcp (green) and on-top (yellow) variants are presented (left picture). Fragment of STM picture taken from [11] showing Pt(111) surface covered by thin Co layer with two stacking variants: fcc and hcp (right picture). 68
3.16 Charge and magnetic moment (total and broken down by d and s+p contributions) evolution across Pt(111) slab (19 layers, blue) with Co fcc-stacked adsorbate (monolayer, green). Surface sites are marked by squares. Solid, dashed and dotted line denotes respectively values for Co bulk, surface and impurity sites. Stacking variant has no impact on these results (fcc stacking is shown). 69
3.17 Comparison of the Mulliken total (circles) and d-orbital (squares) charges (left plot) and local magnetic moments (right plot) with respect to the site mixing rank for platinum (red) and cobalt (blue) sites. This is the average calculated over all surface (Z=8) sites of all considered samples within CoPt slabs of different order parameter η ranging from 0 to 1 (in the case of $\eta = 1$ the surface is supposed to be terminated by Pt). Respective pure bulk values are marked with horizontal lines (dashed for d-orbital). A similar analysis for bulk sites has been presented earlier in Fig. 3.8. 70
3.18 Local density of states of platinum (left) and cobalt (middle) sites in the presence of Co-Pt interface between Co monolayer and Pt(111) slab (solid black) and, for reference, on pure surface (dashed blue) and inside pure slab (magenta dots). The case of a Co impurity placed into a Pt matrix is represented on the right graph (green plot). 71
3.19 Mixed cluster morphologies (from left to right): cuboctahedral $L1_0$ (with cross-section) and icosahedral onion-like (with cross-section). The cluster size is 561 at. 72

3.20 Mulliken charge redistribution (left) and local magnetic moment (right) on small clusters with respect to to the mixing rank of the site for platinum (red) and cobalt (blue) sites. Marker size correspond to the coordination number. Each point was calculated as an average over all equivalent sites (in terms of occupancy, coordination number and mixing rank) for all considered cluster morphologies, sizes and stoichiometries. . 73

4.1 Comparison of the LDOS obtained from paramagnetic TBA (dashed lines) and DFT (solid lines) calculations for cobalt (blue) and platinum (red) sites in pure and mixed infinite systems (bulk and interfaces). . . . 80

4.2 Comparison of the LDOS obtained from paramagnetic TBA (dashed lines) and DFT (solid lines) calculations for various cobalt (blue) and platinum (red) sites in cuboctahedral clusters of 309 atoms with $\mathrm{L1_0}$ ordering. 81

4.3 Averaged DOS (sp-d, non magnetic) in a cuboctahedral CoPt $L1_0$-like cluster of 147 atoms. Solid lines correspond to DFT calculations and dashed ones to TB calculations. The insertion shows the corresponding atomic structure. Color code for both curves and structure in insertion is blue for Co and red for Pt. 82

4.4 Partial d-LDOS on the geometrically inequivalent sites on a cuboctahedral Pt (a) and CoPt $L1_0$-like (b) cluster of 2869 atoms. The insert shows the corresponding atomic structures, in which the sites have been colored upon their environment (coordination, chemical). 84

4.5 Center of gravity of d-band for the geometrically inequivalent Pt (a) and Co (b) sites of cuboctahedral CoPt $L1_0$ like clusters compared respectively to pure Pt and Co clusters. Two sizes are considered: $N_{tot} = 147$ and $N_{tot} = 2869$. Straight lines correspond to linear fits (see text). Label “Co rich” (“Pt rich“) refers to concentration in Co (Pt) > 0.5. . . 85

4.6 Width of the d-band for the geometrically inequivalent Pt (a) and Co (b) sites of cuboctahedral CoPt $L1_0$ like clusters compared respectively to pure Pt and Co clusters. Two sizes are considered: $N_{tot} = 147$ and $N_{tot} = 2869$. Straight lines correspond to linear fits (see text). Label “Co rich” (“Pt rich“) refers to concentration in Co (Pt) > 0.5. 86

4.7 Variation of the *diagonal disorder* parameter in nanoalloys, δ_d^n, as a function of $N^{\frac{1}{3}}$ (representative of the diameter of a cluster containing N atoms). The continuous line represents the theoretical values given by equation (4.9). Red and blue circles represent values deduced from averaged LDOS respectively for the so-called Pt rich and Co rich ordered cuboctahedral clusters (see Fig. 4.5). 88

4.8 (N_e, δ_{nd}) ordering domains represented in the parameter space spanned by δ_{nd} and N_e for different values of δ_d and for alloys at equiconcentration. Ordering domains are delimited by black, blue, dotted green and dotted red lines corresponding respectively to $\delta_d = 2.0$, 1.0, 0.5, 0.25 eV, the area outside these domains corresponding to demixing tendency. This plot is related to an average bandwidth of pure constituents of $W_{\text{av,max}} = 6.0$ eV. The points correspond to bulk and 2869 and 147 atoms clusters. 90

Acknowledgements

I would like to thank people and institutions that made writing this thesis possible.

I especially thank my supervisors, **Dr. Christine Goyhenex** and **Prof. Rafał Kozubski**, for their support and guidance. Discussions that we carried out, enabled me to improve the understanding of the topic and stimulated me in the scientific research. Their enthusiasm and passion was contagious and motivated me to overcome the difficulties. I am particularly grateful for the constructive remarks and patience during the preparation of the manuscript.

My doctoral thesis has been prepared within *cotutelle* scheme in cooperation between M. Smoluchowski Institute of Physics in Krakow and the Institute of Physics and Chemistry of Materials of Strasbourg. My stays in France were mainly supported by the **scholarship of the French Government** for which I am very thankful. I would also like to express my deep gratitude to **Prof. Marc Drillon**, director of the IPCMS for hosting me in the Institute. My special thanks are extended to the **researchers from Department of Surfaces and Interfaces** for their kindness and creating friendly atmosphere.

This work was also supported by the **PHC Polonium** program No. 22556UC, **COST Action MP0903** "Nanoalloys as Advanced Materials: From Structure to Properties and Applications" and the **French National Agency ANR** through ETNAA Project No. ANR-07-NANO-018. Membership of the **European Doctoral College of Strasbourg** allowed me to reduce accommodation costs during my stays in Strasbourg and to cover some travel expenses.

I wish to acknowledge the help provided by the staff of the **Academic Computer Center CYFRONET** (Krakow, Poland) where most of the calculations were carried out on a 271 TFlops ZEUS cluster. Part of this work was also supported by **Institut du Developpement et des Ressources en Informatique Scientifique** through a grant of computer time (Project No. 92291).

Finally, I address my thanks to all others who, in various forms, helped me along the way. Many, many thanks!

ROBACZEK-TKACZEK MA KUBRACZEK I PLECACZEK

Introduction

General idea and motivation

This thesis presents a theoretical work of electronic structure and order tendency in transition metal nanoalloys focusing on the particular case of cobalt-platinum systems.

The interest in alloys of late transition metals arises from their potential applications in high-density magnetic storage devices where they can be used as supported nanoparticle arrays and as stable, efficient and selective catalysts in chemical processes. Presently, however, the preparation of materials with optimal properties faces a number of technological and physical restrictions. Particularly noteworthy is the so-called superparamagnetic limit [12], which restricts the minimum size of the thermally stable magnetic domain and thus, constraints the maximum density of the information storage on magnetic hard drives. On the other hand, in catalysis and electrocatalysis the major problem is to characterize the active sites and to find the correlation between specific configuration (size, shape, composition) and the catalytic properties. Therefore, comprehensive understanding of processes and phenomena resulting in the material properties interesting from the application point of view, is crucial for a successful technology. In particular, both magnetic and catalytic properties are closely related to the modifications of the local electronic structure on various sites mostly due to the differences of chemical and topological environment. This justifies the undertaking of a theoretical research in this direction. An in-depth knowledge of the interplay between structural features on the atomic level and the desired macroscopic properties will allow guidance to the best way of elaboration of dedicated nanoparticles. In particular the ordering phenomena must be well controlled. There is, however, a lack of phase diagrams for nanoalloys. For instance relatively few researchers addressed the size effect on $L1_0$ ordering tendency, much of the work concentrated on FePt systems. The experimental results [13] showed that there was no chemical ordering in FePt particles with a diameter smaller than 3 nm while in case of CoPt ordered phase is observed even at diameter of 2 nm [14].

Characterization of the Co-Pt system

Apart from their magnetic properties the nanoparticles of platinum and 3d-transition metals (such as Co, Ni, Cr) have also attracted attention as possible catalysts for the electrochemical oxygen reduction reaction [15, 16] whose slow rate is one of the obstacles in the development of polymer electrolyte membranes and direct methanol fuel cells. Electrochemical properties of bimetallic Pt-metal bulk electrodes and carbon-supported nanoparticles have been studied by various groups [15, 16, 17]. The results show, that the maximum reactivity is by about one order of magnitude higher than that of pure Pt nanoparticles. There were some experimental [18, 19] and theoretical [20, 21] attempts to explain the effect of a metallic addition on the catalytic activity and selectivity of platinum. Whereas the influence of the composition of Pt-metal alloys on their electrocatalytic activities has been studied quite extensively, the effect of particle size and morphology has up to now not been theoretically investigated. Because of the effect of ordering on the surface composition in contrast to the monotonous dependence of the catalytic activity of the monometallic Pt particles in the size range 1.5-5.0 nm [16] more complex effects are expected for bimetallic particles.

During recent years many teams worldwide synthesized Co-Pt particles with the diameters ranging from very small ones (1-2 nm) up to 10 nm [22, 23] by means of different methods (ion-sputtering, molecular beam epitaxy, redox transmetalation, gas phase cluster deposition, biochemical synthesis of protein - encapsulated grains, reduction of super-hydrides or carbonyls at a high temperature, using the reverse micelles technique and other techniques [24, 25, 26, 27]). Depending on the method used one can obtain structures of different structural and physico-chemical properties - varying in size, morphology, composition and ordering. Synthesized were both "core-shell" (containing separate layers of pure element) and "solid solution" (intermixed) variants on several substrates (graphite, silicon, inorganic oxides, etc.).

Extended characterization of Co-Pt nanoparticles performed by numerous techniques showed chemical L10-type long-range order coupled with strong ferromagnetic behavior of the intermixed nanoparticles at room temperature [28] in contrary to pure Co and Pt "core-shell" clusters which appeared superparamagnetic and exhibited strong thermal fluctuations of magnetic moments [29]. The observed high magnetic anisotropy with associated substantial magnetic susceptibility and coercivity as well as good corrosion resistance [23] lead to the conclusion that ordered CoPt nanoalloys are interesting candidates for ultrahigh-density magnetic recording media.

The bulk phase diagram of the Co-Pt system is represented in Fig. 1. The Co-Pt alloys are known to have a strong tendency for ordering so that the phase diagram is characterized by three main ordered phases, the fcc $L1_2$ ($Co_{0.25}Pt_{0.75}$ and $Co_{0.75}Pt_{0.25}$) and the fct (tetragonalized) $L1_0$ ($Co_{0.5}Pt_{0.5}$). Cobalt-rich $L1_2$ structure is significantly less marked. It is speculated that assymmetry of $L1_2$ phases' stability can be attributed to the presence of strong ferromagnetism ([8] and references therein).

One of the main questions about ordering phenomena in CoPt is about the role of magnetism which has been shown very recently to be much important [30]. We will also investigate this point using DFT calculations.

As the main current interest with CoPt is to synthesize nanoparticles with enhanced catalytic or magnetic properties (anisotropy mainly in this case), many experimental efforts till now concentrated on obtaining perfectly ordered $L1_0$ CoPt nanoparticles [22]. In this field size effects have to be closely investigated since not only properties may be modified in nanoparticles with regards to bulk alloys but also more fundamentally the phase diagram. For instance although the $L1_0$ structure is the most stable one in the bulk alloy, this statement cannot be directly extended to nanoalloys because of finite size effects. As already mentioned currently no actual phase diagram is available for nanoalloys but some evidences for possible modifications have been reported. For

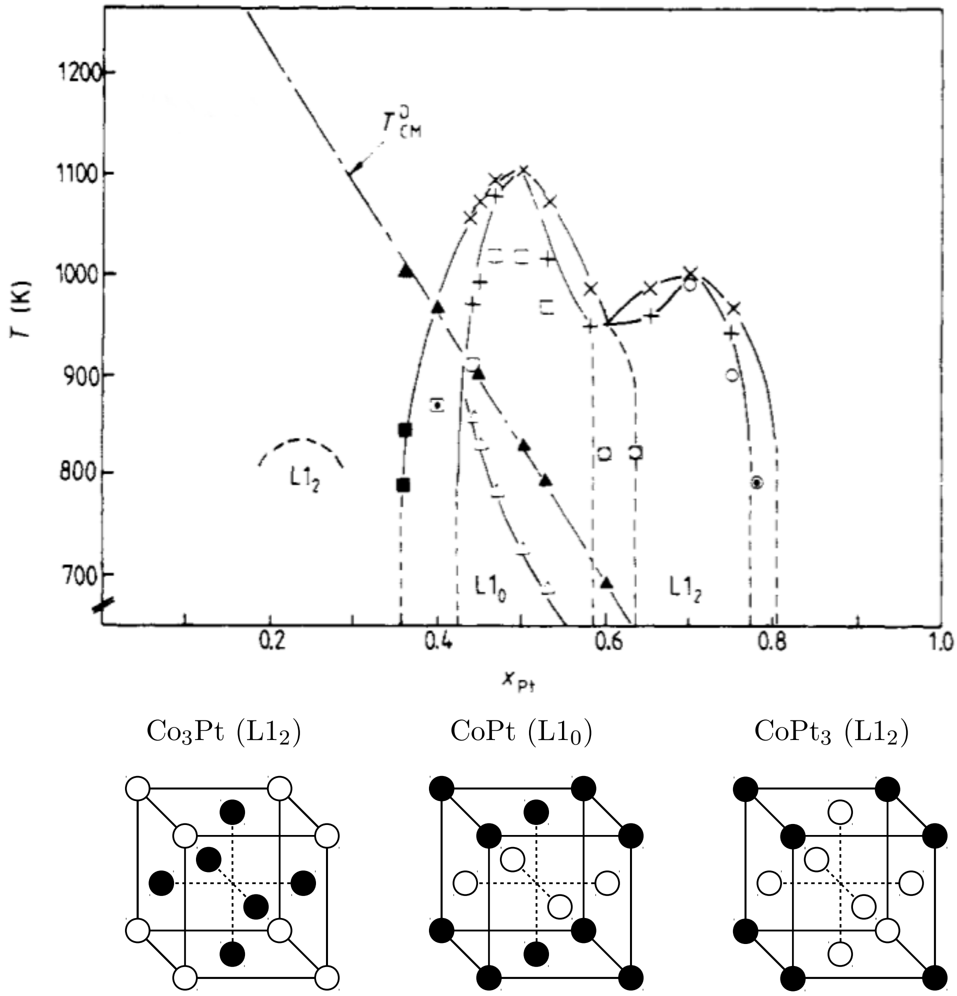

Co_3Pt ($L1_2$)　CoPt ($L1_0$)　$CoPt_3$ ($L1_2$)

Figure 1: High-temperature magnetic and chemical phase diagram of the CoPt system [8]. Example $L1_2$ (Co_3Pt, $CoPt_3$) and $L1_0$ (CoPt) structures are shown below.

instance D. Alloyeau *et al.* [14] recently found, within both experimental observations (High Resolution Transmission Electron Microscopy) and atomistic simulations (Monte Carlo), that the order-disorder transition temperature in CoPt equiatomic $2-3$ nm nanoparticles is $325-175$ K lower than the bulk material transition temperature.

In this context the need to predict ordering tendencies in nanoalloys motivated the main goal of this work. A first step in this direction proposed here consists of the development of a model able to predict the ordering tendency (basically versus phase separation) in nanoalloys on the basis of their electronic structure determined using a tight-binding scheme founded on specific DFT calculations. The choice for studying the electronic structure is tightly related to the fact that the properties of nanoalloys depend on the local electronic structure on the various inequivalent sites showing particular chemical and morphological structures.

From the methodological point of view a simplified parametrized description of the electronic structure is often necessary for studies of complex transition-metal compounds involving intricate surface, structural and chemical effects. A wide variety of currently available *ab-initio* Density Functional Theory (DFT) band structure codes are available. Up to now these codes are still applicable to relatively simple structures, and in general, cannot be used in systematic studies of thermally activated structural transformations such as e.g. order/disorder phenomena in bulk or nano-structured alloys. Such studies have been most often feasible within diverse semi-empirical approaches, among which the Tight-Binding Approximation (TBA) is particularly well suited. Depending on the problem, it allows tuning the accuracy of the electronic structure determination by handling the number of exact moments of the local densities of states (LDOS) which are calculated. In all cases, the TBA simulations require a self-consistent treatment of the link between the atomic orbital level shifts and charge redistribution on the various sites which may differ either geometrically (particular coordination in bulk or at the surface) or chemically (occupation by particular atoms).

For at least two decades the former aspect has been extensively studied in the case of pure metal surfaces in connection with the development of surface core level spectroscopy techniques. Very few studies addressed, however, multicomponent systems (alloys) and up to now, no rules for the correct and efficient treatment of charge transfer in nanoalloys have been elaborated. Such an analysis is however useful, not only for the sake of interpretation of alloy core level experiments, but more generally for the sake of enabling thermodynamic calculations based on electronic structure for which the essential data is the effect of alloying on the atomic levels (so-called here "diagonal disorder"). While usual interpolation schemes of the pure element band structure have generally become inadequate, the situation is still more complicated for late transition series elements for which not only d but also s-p electrons have to be taken into account, as already shown in the case of surfaces [31, 32]. Indeed, even though it is known from DFT approach that, in the case of a pure metal surface, the surface electronic charge is the same as in the bulk, not only per site but also per orbital [32] we do not control to the same extent how the things evolve as soon as two different elements are present.

A local neutrality rule for the CoAu system has been already investigated in [33]. The aim of the present work is to generalize such local neutrality rule for another archetypal system, CoPt, which contrary to CoAu exhibits a strong ordering tendency in bulk and whose particularity consists of the fact that a complex magnetic metal is alloyed with a late transition one for which sp-d hybridization may be important. From there the second aim will be to develop a model, based on tight-binding electronic structure calculations, for predicting ordering tendencies in nanoalloys within simple parameters.

Organization

The thesis is divided into three main parts.

In the first chapter the extensive description of the methodology is given and some technical aspects of the performed calculations are discussed. The *ab-initio* class of methods covers all approaches that start directly from the well established physical laws without imposing system-specific arbitrary models or forcing approximations that require parameter fitting. In the solid-state physics it means that the properties of the material are derived from its electronic structure calculated by solving a quantum mechanical many-body problem. Within DFT any property of a system of interacting particles in an external potential can be described by a *functional* of the ground state electron density which can be determined self-consistently. The DFT calculations have been performed with the SIESTA [34] method which uses the basis of linear combination of atomic orbitals (LCAO). The GGA (Generalized Gradient Approximation) exchange-correlation functional in the PBE [35] parametrization has been used. In the Tight Binding method every single electronic wave function can be represented as a linear combination of fixed atomic orbitals associated with particular atoms and therefore the method is the best suited for studying systems where there is no significant overlap between orbitals like transition metals studied here. The TB Hamiltonian for a binary alloy in the basis of atomic orbitals involves two types of matrix elements: diagonal atomic levels for given atom and off-diagonal hopping integrals between two orbitals on neighboring sites. In a mixed system the difference between these values for different atoms (disorder parameters) drives the redistribution of the electronic states with respect to those of pure elements. These fundamental parameters are calculated from the averaged LDOS for a given atom type obtained by the recursion method [36] as a continued fraction, whose coefficients are directly related to the moments of LDOS. These LDOS are determined from a self-consistent treatment of the environment-driven charge redistribution using a local charge neutrality rule as validated by DFT calculations. The local electronic structure within DFT and TBA methods is studied for inequivalent sites classified with respect to their local environment, up to the first nearest neighbors.

Chapters two and three of the thesis are focused on the DFT results for Co, Pt elemental systems, CoPt bulk alloys at different concentrations and CoPt systems with lower dimensionality (surfaces, nanoparticles). First the basic structural properties are calculated and compared with the data available in literature (both experimental and theoretical). Then, surface energies of pure Pt(100), Pt(111) and Co(0001) surfaces are calculated and in the case of pure clusters a simple analysis of the favorable shape with respect to the size is performed. In case of mixed systems systematic analysis of the heats of formation with respect to concentration is performed in order to investigate the importance of magnetism for stabilization of the structure. The main objective is, however, to study in detail the charge redistribution and local magnetic moments on sites in different structural and chemical environments. This analysis is performed first in the simplest case of the pure systems where only the site coordination effects are present (pure surfaces and single-component clusters). Secondly, mixed binary systems are introduced which allows to determine the charge transfers between orbitals of the two atom species both inside the bulk with only concentration-dependent chemical effects and in more intricate case of surfaces and small clusters where the effects of the site coordination and chemical environment are combined. The effect of the coordination, concentration and local chemical environment is studied in detail with the aim to verify the local neutrality rule per site, species and orbitals. Some limits to the strict generality are identified. The results obtained at this step will allow a self-consistent determination of the atomic level shifts within the TBA calculations (next chapter).

The fourth chapter is devoted to the TBA calculations which, in the context of the thesis, have been conducted only in the case of paramagnetic model systems. TBA calculations were performed first for a number of selected simple structures with the aim to compare the results with DFT calculations (pure fcc bulk, $L1_0$ CoPt, dilute systems and Co monolayer on Pt(111)). The LDOS determined for the same systems by means of DFT and TBA techniques are compared and evaluated in terms of the fulfillment of the neutrality rule. The comparison of the results obtained by DFT and TBA techniques is then extended to a small typical cuboctahedral cluster of CoPt with an $L1_0$ ordered arrangement by comparing the average Co and Pt DOS. Subsequently more realistic cluster sizes and configurations inaccessible directly by *ab-initio* approaches are analyzed. This analysis is mainly focused on model cuboctahedral shapes with $L1_0$ ordering. The LDOS on sites with different chemical environment and coordination number is studied in detail. Systematic analysis of those changes as a function of the site coordination is performed and some trends are identified. These observation is then used to predict the average atomic d-level given the cluster size, which allows to predict the basic features of the LDOS (d-band center and d-band width) by simple laws with structural and chemical terms. Following the previous work on the ordering trends in transition metal alloys [37] we propose a new way to predict the ordering tendency for any transition metal nanoalloy as a function of its size. This is achieved on the basis of the basic properties of DOS either directly calculated in the TBA framework for given structure or estimated by the simplified laws. The study is summarized with a map of ordering regions composed of the analyzed clusters which along with data available in the literature allows to determine ordering domains and to predict the ordering preference of a cluster solely by its location on the map.

In conclusion the results obtained in both approaches will be summarized and a number of improvements along with the future perspectives will be briefly discussed.

CHAPTER 1

Methodology

1.1 First principles approach

Ab-initio class of methods covers all approaches that start directly from the well established laws of physics without imposing system-specific arbitrary models or forcing approximations that require parameter fitting. In solid-state physics it means that properties of the material are derived from its electronic structure calculated by solving quantum mechanical many-body problem for a system of electrons and atomic nuclei.

1.1.1 Hamiltonian of many-body system

A system of N_n nuclei each one located at the position $\mathbf{R}_k$, having the electronic charge Z_k, mass M_k and being associated with N electrons at positions $\mathbf{r}_l$ each having a mass m_e and electronic charge e can be described by the Hamiltonian:

$$\hat{H} = -\underbrace{\sum_{i}^{N} \frac{\hbar^2}{2m_e}\nabla_i^2}_{\text{kinetic energy of electrons}} + \overbrace{\sum_{\substack{i,j\\ i<j}}^{N} \frac{e^2}{|\mathbf{r}_i - \mathbf{r}_j|}}^{\text{electron-electron interaction}} - \underbrace{\sum_{i}^{N_n} \frac{\hbar^2}{2M_i}\nabla_i^2}_{\text{kinetic energy of nuclei}} + \overbrace{\sum_{\substack{i,j\\ i<j}}^{N_n} \frac{Z_i Z_j e^2}{|\mathbf{R}_i - \mathbf{R}_j|}}^{\text{nucleus-nucleus interaction}} - \underbrace{\sum_{i}^{N}\sum_{j}^{N_n} \frac{Z_j e^2}{|\mathbf{r}_i - \mathbf{R}_j|}}_{\text{electron-nucleus interaction}}$$

The state of such system can be determined by solving the Schrödinger equation:

$$\hat{H}\Psi_n(\{\mathbf{R}_j\},\{\mathbf{r}_i\}) = E_n\Psi_n(\{\mathbf{R}_j\},\{\mathbf{r}_i\}) \tag{1.1}$$

where Ψ_n is a complete many-body wavefunction of the system state with energy E_n.

Because of the electrostatic nature of all interactions in the system the forces on both electrons and nuclei are of the same order of magnitude. Since typically nuclei are by 5 orders of magnitude more massive than electrons they move with much smaller velocities and the time-scales of nuclear and electronic motion will be well separated. This separation, known as *adiabatic* or Born-Oppenheimer approximation [38], allows to find the electronic ground-state under the assumption that nuclei are stationary and then to evaluate system energy and solve the problem of nuclear motion. Neglecting the nuclear kinetic energy and the nucleus-nucleus interaction terms the Hamiltonian is written as:

$$\hat{H} = \overbrace{-\sum_{i}^{N} \frac{\hbar^2}{2m_e}\nabla_i^2}^{\hat{T}} + \overbrace{\sum_{\substack{i,j\\ i<j}}^{N} \frac{e^2}{|\mathbf{r}_i - \mathbf{r}_j|}}^{\hat{V}_{\text{int}}} - \overbrace{\sum_{i}^{N}\sum_{j}^{N_n} \frac{Z_j e^2}{|\mathbf{r}_i - \mathbf{R}_j|}}^{V_{\text{ext}}} \tag{1.2}$$

The problem is now simplified compared to 1.1, but due to the many-body nature of electron-electron interactions it is still too complicated to be solved for $N \geq 3$.

Independent electron approximations

In order to further simplify the problem instead of dealing with the motion of N electrons in the ionic potential of N_n nuclei one can take a *mean field* approach by replacing the interaction between a given electron with all the remaining ones with effective potential V_{eff}. This leads to the "non-interacting", one-electron Hamiltonian without explicit electron-electron interaction term. The effective potential can be expressed in terms of the electron density:

$$\rho(\mathbf{r}) = \sum_{\sigma}\sum_{i} f_i^{\sigma} |\Psi_i^{\sigma}(\mathbf{r})|^2 \quad f_i \text{ - Fermi-Dirac distribution} \quad \sigma \in \{\uparrow, \downarrow\} \text{ - spin} \tag{1.3}$$

With V_{eff} defined as averaged Coulomb interaction the Hamiltonian 1.2 now writes:

$$\hat{H} = -\sum_{i}^{N} \frac{\hbar^2}{2m_e}\nabla_i^2 + \underbrace{e^2 \int \mathrm{d}\mathbf{r}' \, \frac{\rho(\mathbf{r}')}{|\mathbf{r} - \mathbf{r}'|}}_{V_{\text{eff}}} - \sum_{i}^{N}\sum_{j}^{N_n} \frac{Z_j e^2}{|\mathbf{r}_i - \mathbf{R}_j|} \tag{1.4}$$

In this approximation, proposed in 1927 by D.R. Hartree, the true N-electron wavefunction $\Psi(\{\mathbf{r}_i, \sigma_i\})$ is replaced by a product of single-electron wavefunctions $\psi_i(\mathbf{r}_i, \sigma_i)$:

$$\Psi(\{\mathbf{r}_i, \sigma_i\}) = \frac{1}{\sqrt{N}} \prod_{i}^{N} \psi_i(\mathbf{r}_i, \sigma_i) \qquad \sigma_i \text{ - spin of the electron} \tag{1.5}$$

Solution of the Schrödinger equation 1.1 for the Hamiltonian 1.4 requires *a priori* knowledge of the $\rho(\mathbf{r})$. One must, therefore, employ an iterative procedure and construct an effective potential from the density obtained in the preceding step starting with some postulated, initial $\rho(\mathbf{r})$. This algorithm continues until *self-consistency* is reached.

The Hartree factorization 1.5 clearly does not take into account the antisymmetry of the fermionic wavefunctions and therefore totally neglects the exchange interactions coming from the exclusion principle. The solution is to define the *Slater determinant*:

$$\Psi(\{\mathbf{r}_i, \sigma_i\}) = \frac{1}{\sqrt{N!}} \begin{vmatrix} \psi_1(\mathbf{r}_1, \sigma_1) & \cdots & \psi_1(\mathbf{r}_N, \sigma_N) \\ \vdots & \ddots & \vdots \\ \psi_N(\mathbf{r}_1, \sigma_1) & \cdots & \psi_N(\mathbf{r}_N, \sigma_N) \end{vmatrix} \tag{1.6}$$

which leads to *Hartree-Fock* approximation where the Hamiltonian 1.4 contains an additional state-dependent exchange term $V_{\mathrm{EX}}^{i,\sigma}$ that damps the potential V_{eff} for equal spins:

$$V_{\mathrm{EX}}^{i,\sigma} = -\Big[\sum_j \int \mathrm{d}\mathbf{r}' \, \frac{\psi_j^*(\mathbf{r}',\sigma)\psi_j(\mathbf{r}',\sigma)}{|\mathbf{r}-\mathbf{r}'|}\Big] \frac{\psi_j(\mathbf{r},\sigma)}{\psi_i(\mathbf{r},\sigma)} \tag{1.7}$$

Besides the fact that the Hartree-Fock approximation yields equations hard to solve in all but a few special cases (spherically symmetric atoms, homogeneous electron gas) it is still a mean-field approximation that does not properly account for the correlated motion of electrons. Several post-Hartree-Fock methods aiming at overcoming this limitation were proposed [39] and are widely used in quantum chemistry.

1.1.2 Density Functional Theory

Fundamental observation that led to one of the most successful theories that is until today most widely used in *ab initio* calculations is similar to those previously discussed: any property of a system of interacting particles in external potential can be described by a *functional* of the ground state electron density. The existence proof for such functional, without, however any suggestions concerning the exact methodology for its construction was given in 1964 by Hohenberg and Kohn [40].

The Hohenberg-Kohn theorems

Theorem 1: For any system of interacting particles in an external potential V_{ext}, the potential V_{ext} is determined uniquely, except for a constant by the ground state particle density $\rho(\mathbf{r})$ which means that the Hamiltonian is fully determined as well.

Theorem 2: A universal functional for the system energy $E[\rho]$ can be defined in terms of the density $\rho(\mathbf{r})$ corresponding to any external potential V_{ext} and for which the exact ground state of the system is the global minimum of functional $E[\rho]$. The density $\rho(\mathbf{r})$ which minimizes the functional is the exact ground state density $\rho_0(\mathbf{r})$.

An alternative formulation of Levy and Lieb [41, 42] provides an operational definition of the functional. The total energy for any many-body state Ψ can be written with 1.2 as:

$$E = \langle\Psi|\,\hat{T}\,|\Psi\rangle + \langle\Psi|\,\hat{V}_{\mathrm{int}}\,|\Psi\rangle + \int \mathrm{d}^3\mathbf{r}\, V_{\mathrm{ext}}(\mathbf{r})\rho(\mathbf{r}) \tag{1.8}$$

One can define the unique lowest energy for particular electronic density $\rho(\mathbf{r})$ by minimizing the expression 1.9 over all states Ψ that have the same density $\rho(\mathbf{r})$:

$$E[\rho] = \overbrace{\min_{\Psi\rightarrow\rho(\mathbf{r})} \big[\, \langle\Psi|\,\hat{T} + \hat{V}_{\mathrm{int}}\,|\Psi\rangle \,\big]}^{F[\rho(\mathbf{r})]} + \overbrace{\int \mathrm{d}^3\mathbf{r}\, V_{\mathrm{ext}}(\mathbf{r})\rho(\mathbf{r})}^{E_{\mathrm{ext}}} \tag{1.9}$$

The first part of the expression 1.9 defines the Levy-Lieb functional $F[\rho(\mathbf{r})]$ that does not depend on the V_{ext}. The exact analytical form of this functional is not known, but it may be expressed in terms of the kinetic energy of a non-interacting electronic gas T_s, the electron density self-interaction Hartree term E_H and the many-body exchange-correlation energy E_{XC}:

$$F[\rho] = \overbrace{\frac{1}{2}\sum_{\sigma,i}|\nabla\Psi_i^\sigma|^2}^{T_s[\rho]} + \overbrace{\frac{1}{2}\int \mathrm{d}^3\mathbf{r}\,\mathrm{d}^3\mathbf{r}'\,\frac{\rho(\mathbf{r})\rho(\mathbf{r}')}{|\mathbf{r}-\mathbf{r}'|}}^{E_H[\rho]} + \overbrace{\int \mathrm{d}^3\mathbf{r}\,\rho(\mathbf{r})\varepsilon XC(\mathbf{r})}^{E_{\mathrm{XC}}[\rho]} \tag{1.10}$$

where $\varepsilon XC(\mathbf{r})$ denotes the exchange-correlation *energy density* (energy per particle).

1.1.3 Approximations of the exchange-correlation functional

The main difficulty is now to properly approximate the εXC term as a local or nearly-local functional of the electron density. Over the years, diverse approximations have been developed. Starting with a relatively simple variant based on the local density only one can incorporate increasingly complex components accounting for the environment and mimic features of the true, exact functional. Some of them can be quite sophisticated and designed to deal with highly specific set of problems. This is sometimes referred to as a *Jacob's ladder* of density functional approximations for the exchange-correlation energy [43] with the ideal exact-exchange at the "heaven" level.

Local (Spin) Density Approximation

The simplest form of such approximation has been proposed by Hohenberg, Kohn and Sham [40, 44]. The εXC is assumed to be identical to the exchange-correlation energy density $\varepsilon XC^{\mathrm{HEG}}$ corresponding to a homogeneous electron gas (HEG) of the same density. While the analytical formula for the exchange energy density $\varepsilon X^{\mathrm{HEG}}$ of HEG is available ($\propto \sqrt[3]{\rho}$), the correlation part $\varepsilon C^{\mathrm{HEG}}$ can be approximated by Wigner correlation functional [45] following directly from HEG model, calculated by a means of quantum Monte Carlo simulations [46] or estimated using various analytical forms (see e.g. Vosko, Wilk and Nusair (VWN) [47], Perdew and Zunger (PZ81) [48]). The notion of *locality* stems from the fact, that the functional at a given point is fully defined by the electron density at that particular point. The LSDA approximation is a simple spin-wise generalization of LDA with spin density ρ_σ:

$$\varepsilon XC^{\mathrm{LSDA}}[\rho_\uparrow,\rho_\downarrow] = \varepsilon XC^{\mathrm{HEG}}[\rho_\uparrow,\rho_\downarrow] \equiv \varepsilon X^{\mathrm{HEG}}[\rho_\uparrow,\rho_\downarrow] + \varepsilon C^{\mathrm{HEG}}[\rho_\uparrow,\rho_\downarrow] \tag{1.11}$$

The rationale for the local approximation is that the range of the exchange-correlation effects for typical electron densities in solids is relatively short. This assumption is especially valid for nearly-free-electron metals reasonably described in terms of the standard electron-gas model. Worse results should be expected for systems with more localized electrons like late transition metals and where magnetism plays significant role.

Generalized-Gradient Approximations

The accuracy of the L(S)DA for systems with highly inhomogeneous electron density can be improved by taking into account the density gradient. In real materials with large variations of ρ the parametrization of exchange - correlation functional only in terms of ρ and magnitude of its $|\nabla\rho_\sigma|$ at each point (low-order gradient expansion [44, 49, 50]) appears insufficient and does not lead to consistent improvement over L(S)DA sometimes yielding worse results [9]. The solution is the *generalized*-gradient expansion (GGA) where the special dimensionless functional $F_{\text{XC}}[\rho, |\nabla\rho|, \ldots]$ is introduced to modify the behavior of large electron density gradients:

$$\varepsilon XC^{\text{GGA}}[\rho_\uparrow, \rho_\downarrow] = \varepsilon X^{\text{HEG}}[\rho_\uparrow, \rho_\downarrow]\, F_{\text{XC}}[\rho_\uparrow, \rho_\downarrow, |\nabla\rho_\uparrow|, |\nabla\rho_\downarrow|, \ldots] \tag{1.12}$$

The exchange part F_{X} of this GGA *enhancement factor* F_{XC} can be expressed in terms of the Seitz radius r_s which equals to the average distance between electrons and the dimensionless reduced density gradients of k-th order defined as [9]:

$$s_k = \frac{|\nabla^k \rho|}{(2k_F)^k\, \rho} \quad \text{where } k_F \text{ denotes Fermi wave vector} \quad k_F = \frac{3\sqrt[3]{2\pi/3}}{r_s} \tag{1.13}$$

Numerous formulas for F_{XC} have been proposed. The most common ones include those of Becke (B88) [51], Perdew and Wang (PW91) [52], Becke [51], Lee, Yang and Parr [53] (BLYP) and Perdew, Burke and Enzerhof (PBE) [35] which has been used for the purpose of the present work. The PBE formula used in the present work involves a simplified form of the PW91 F_{X} factor:

$$F_{\text{X}}^{\text{PBE}}(s \equiv s_1) = 1 + \kappa - \frac{\kappa}{1 + \mu s^2/\kappa} \quad \mu = 0.21951 \quad \kappa = 0.804 \tag{1.14}$$

The parameters μ and κ were introduced in order to recover the linear response form of the local approximation and satisfy the Lieb-Oxford bound [54]. Since $F_{\text{X}} \geq 1$ per definition 1.14, PBE-GGA leads to the exchange energy lower than in LDA which results in a reduction of the binding energy and the correction of its overestimation typical for LDA. The correlation factor F_{C} is usually expressed in terms of the exchange $\varepsilon X^{\text{LDA}}$ and the correlation $\varepsilon C^{\text{LDA}}$ energy densities stemming from LDA [55, 56, 35] (PW91, PBE). Alternatively, the orbital-dependent Colle-Salvetti correlation-energy formula is sometimes used [53] (LYP). In all cases F_{C} vanishes with $s \to \infty$.

Strategy for the choice of the optimum E_{XC} approximation

GGA functionals are commonly considered as an improvement over LDA [43] but the choice of the XC potential always depends on the studied system and its particular properties to be calculated. For instance, LDA tends to overestimate the bond strength leading to underestimated lattice constants and overestimated bulk moduli while GGA exhibit opposite behavior [57]. This tendency is particularly well marked in the case of 3d metals, especially magnetic ones since magnetization strongly depends on interatomic distances and decreases with lattice contraction. A very well known example is the case of phase diagram of iron - LDA calculations indicate that the most stable phase should be paramagnetic fcc instead of ferromagnetic bcc. However, there is no general rule that allows to unambiguously choose the XC functional for given system other than comparison of the results of test calculations between each other and with available experimental data. This "strategy" will be indeed applied in the case of Co and Pt in the next chapter. The choice of particular parametrization is also important in view of the considerable effect of the proportion between the magnitudes of the exchange and correlation components on the accuracy of the result where specific kind of interactions play significant role [58]. GGA has been successfully applied in several related works [59, 60, 61]. PBE parametrization, in turn, is considered most universal (thus not specifically designed for solids/molecules) which is important in this work. For complete review and extensive tests see [62, 58, 63].

1.1.4 Kohn-Sham equations

The idea of the Kohn-Sham approach consists of replacing a complex many-body interacting systems with an auxiliary non-interacting system showing the same ground-state density. Combining the formula 1.9 with 1.10 the energy functional may be expressed as a sum:

$$E_{\mathrm{KS}} = T_s[\rho] + E_{\mathrm{ext}} + E_H[\rho] + E_{\mathrm{XC}}[\rho] \tag{1.15}$$

The ground-state solution for the auxiliary system can be found through the variational minimization of 1.15 with respect to a set of electronic one-particle electron states ψ_i^σ:

$$\frac{\delta E_{\mathrm{KS}}}{\delta \psi_i^{\sigma *}} = \frac{\delta T_s}{\delta \psi_i^{\sigma *}} + \left[\frac{\delta E_{\mathrm{ext}}}{\delta \rho} + \frac{\delta E_H}{\delta \rho} + \frac{\delta E_{\mathrm{XC}}}{\delta \rho}\right] \frac{\delta \rho}{\delta \psi_i^{\sigma *}} = 0 \tag{1.16}$$

Setting $\delta T_s / \delta \psi_i^{\sigma *} = -\frac{1}{2}\nabla^2 \psi_i^\sigma$, $\delta E_{\mathrm{ext}}/\delta\rho = V_{\mathrm{ext}}$ and $\delta\rho/\delta\psi_i^{\sigma *} = \psi_i^\sigma$ one can make use of the Lagrange multiplier method with multipliers ε_i^σ to satisfy orthonormality constraints of ψ_i^σ and write 1.16:

$$\left(-\frac{1}{2}\nabla^2 + V_{\mathrm{ext}} + \frac{\delta E_H}{\delta \rho} + \frac{\delta E_{\mathrm{XC}}}{\delta \rho} - \varepsilon_i^\sigma\right)\psi_i^\sigma = 0 \tag{1.17}$$

The above Kohn-Sham equations define an effective potential:

$$V_{\mathrm{KS}}(\mathbf{r}) = V_{\mathrm{ext}}(\mathbf{r}) + \frac{1}{2}\int \frac{\rho(\mathbf{r})}{|\mathbf{r}-\mathbf{r}'|}\mathrm{d}\mathbf{r}' + \frac{\delta E_{\mathrm{XC}}}{\delta \rho(\mathbf{r})} \tag{1.18}$$

In this formulation the effective potential is composed of the external potential V_{ext} the Hartree term and exchange-correlation potential defined as a functional derivative of E_{XC}. Since LDA and GGA yield E_{XC} as a *function* of the electron density and its gradients at a given point the corresponding XC potential is expressed explicitly [9].

Solving the Kohn-Sham equations

Formula 1.17 defines a set of coupled Schrödinger equations for independent particles in effective potential depending self-consistently on the electron density ρ. Therefore, the algorithm for solving this set of equations requires an iterative procedure like the one discussed in section 1.1.1 for Hartree approach. Fig. 1.1 shows a scheme of such procedure.

① The initial shape of $\rho(\mathbf{r})$ is set. Proper guess of initial electronic density facilitates the convergence of the algorithm. Depending on the problem this can be achieved by simply superimposing the charge densities of isolated atoms, through some *a priori* chemical knowledge, from previous unconverged iteration or from calculations performed for a slightly different geometry [64, 65].

② The effective potential V_{eff} for the current electronic density $\rho(\mathbf{r})$ is constructed using the selected exchange-correlation functional containing the Hartree term and the external potential V_{eff} of the nuclei. The strong nuclear Coulomb potentials are usually replaced by effective ionic **pseudopotentials** that account for the screening effects of the tightly-bound core-electrons and excludes them from explicit calculations.

③ The most computationally demanding step is the numerical solution of the Kohn-Sham equation for given *probe* potential determined by the current electron density $\rho(\mathbf{r})$. The procedure involves expansion of the eigenvectors $\psi_i(\mathbf{r})$ in terms of a basis of functions showing particular properties. This **choice of a basis** leads to distinct but equivalent descriptions of the underlying electronic structure. Each method has its advantages, disadvantages and applicability constraints.

④ The solution of step 3 is now used to calculate the next-iteration electron density $\rho(\mathbf{r})$ and the steps 2 and 3 are repeated until self-consistency between obtained after algorithm iteration electronic density $\widetilde{\rho}(\mathbf{r})$ and $\rho(\mathbf{r})$ used before for potential construction. Convergence is usually verified through the condition $\max_{ij}(\widetilde{\rho}_{ij}, \rho_{ij}) < T$ evaluated on density matrix elements ρ_{ij}. The arbitrarily chosen tolerance T determines the accuracy of calculations.

⑤ If the self-consistency was not reached a new value of the density is chosen using currently calculated $\widetilde{\rho}(\mathbf{r})$ and previous values of $\rho(\mathbf{r})$. The way the choice is made can seriously affect the convergence and the possibility to achieve self-consistency quickly. The simplest form of the density **mixing scheme** is linear mixing shown on the diagram which leads to the "steepest descent" direction for minimization of the energy. Several numerical mixing schemes have been developed, most notably the modified Broyden method [66, 67] and Pulay [68] mixing.

1.1.5 Basis sets

The solution of Kohn-Sham equations 1.17 involves finding the eigenvectors and respective eigenvalues. The procedure is to expand the eigenvectors in terms of functions of known properties. Ensemble of such functions f_k form a basis in which $\psi_i(\mathbf{r})$ writes:

$$\psi_i(\mathbf{r}) = \sum_k c_{ik} f_k(\mathbf{r}) \tag{1.19}$$

The basis can be chosen in a number of ways, each having some advantages and disadvantages. Most important criteria for the choice of basis include: the asymptotic completeness, computational complexity, efficiency and achievable accuracy of the calculations, conceptual simplicity and ease of implementation, meaningfulness of the physical interpretation and its relevance for a particular problem. Existing methods can be classified into one of the three families [9, 69]:

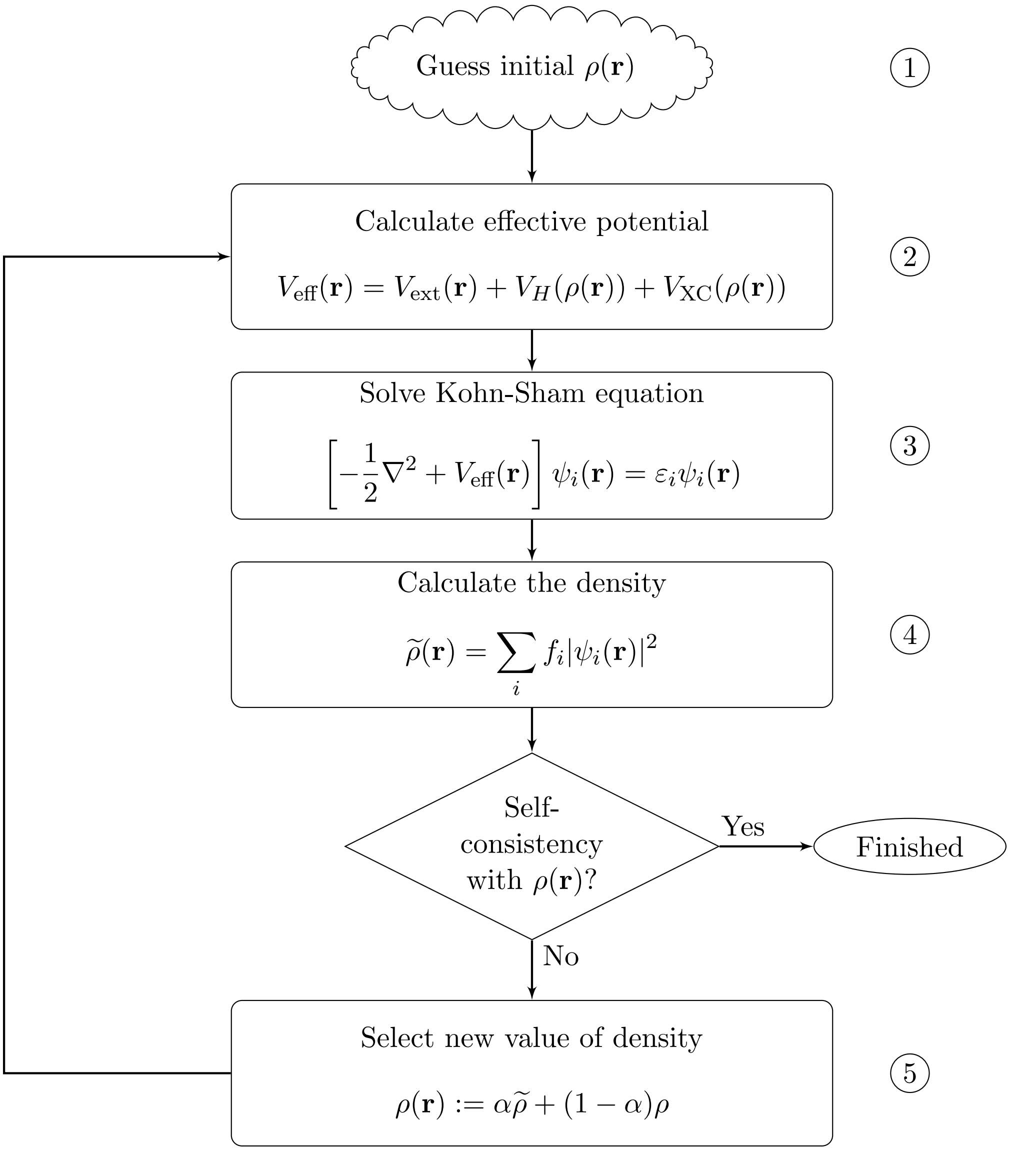
Guess initial $\rho(\mathbf{r})$
①
Calculate effective potential
$V_{\text{eff}}(\mathbf{r}) = V_{\text{ext}}(\mathbf{r}) + V_H(\rho(\mathbf{r})) + V_{\text{XC}}(\rho(\mathbf{r}))$
②
Solve Kohn-Sham equation
$\left[-\frac{1}{2}\nabla^2 + V_{\text{eff}}(\mathbf{r})\right]\psi_i(\mathbf{r}) = \varepsilon_i\psi_i(\mathbf{r})$
③
Calculate the density
$\widetilde{\rho}(\mathbf{r}) = \sum_i f_i|\psi_i(\mathbf{r})|^2$
④
Self-consistency with $\rho(\mathbf{r})$?
Yes
Finished
No
Select new value of density
$\rho(\mathbf{r}) := \alpha\widetilde{\rho} + (1-\alpha)\rho$
⑤

Figure 1.1: Self-consistent algorithm for solution of Kohn-Sham equations [9].

- **plane wave and grids**
  Plane wave methods are very widely used due to their conceptual simplicity (Fourier transforms) and generality achieved by not making assumptions regarding the specific features of the eigenvectors. This also means, that they are not tailored to represent any function in particular and hundreds of plane waves per atom are necessary to achieve good accuracy. Real-space grids are appealing alternative for finite systems, but essentially suffer from the same problems.

- **localized basis sets**
  Plane wave approach also lacks the locality and straightforward physical interpretation which is a strong point of localized methods and specifically of a basis of localized atomic-like orbitals (LCAO). In this case the basis consists of relatively few, atom-centered functions with radial component and spherical harmonic. Several representation schemes are available (e.g. Gaussian-based, Slater orbitals or Numerical Atomic Orbitals). The LCAO approach is closely related to the Slater-Koster Tight-Binding method and due to the small number of well suited functions offers excellent efficiency and potential accuracy. The main drawback is the lack of systematic rules for selecting proper basis functions for given system.

- **atomic sphere methods**
  This is a family of most general methods offering hybrid description with smoothly varying functions between atoms and efficient representation of atomic-like features near nuclei (augmentation). Notable members of this family are Korringa-Kohn-Rostoker method, Augmented Plane Waves approach and muffin-tin orbitals. These methods are ones of the most accurate in DFT, but non-linear (with linearization possibility), difficult to implement and numerically expensive.

Numerical Atomic Orbitals implemented in SIESTA code are constructed as numerical solution of Kohn-Sham equations of isolated pseudo atom using Numerov method on logarithmic grid which is more dense close to the nucleus. The basis functions are then defined by the adjustable radial component and well defined spherical harmonic for given orbital. The radial part is composed from one (single-ζ) or more (double-ζ, triple-ζ, . . .) radial functions. Additionally, since in the solid there is no real spherical symmetry additional angular momenta must be introduced through artificial polarization functions that are not present in the minimal basis of the atom [9].

1.1.6 Pseudopotentials

A typical solid state system contains two basic categories of electrons:

- *core electrons* - chemically inert, described by localized wavefunctions and tightly bound to the nuclei on very deep energy levels

- *valence electrons* - responsible for the formation of atomic bonds, almost delocalized (electron gas in metals) and having most impact on the material properties

$$\textbf{Co}\text{: } \underbrace{1s^2 2s^2 2p^2 3s^2 3p^6}_{\text{core electrons}} \overbrace{4s^2 3d^7}^{\text{valence electrons}} \qquad \textbf{Pt}\text{: } \underbrace{1s^2 2s^2 2p^2 3s^2 3p^6 3d^{10} 4s^2 4p^6 5s^2 4d^{10} 5p^6 4f^{14}}_{\text{core electrons}} \overbrace{5d^9 6s^1}^{\text{valence electrons}}$$

Since the predominant effect brought about by the core electrons is screening of the nuclear potential there was an idea to exclude core electrons from the current calculations and to account for their effect by constructing effective *pseudopotentials* (PS). Within this procedure, the related all-electron wavefunctions $\psi_i(\mathbf{r})$ are replaced by pseudo-wavefunctions $\psi_i^{\mathrm{PS}}(\mathbf{r})$ that are identical to $\psi_i(\mathbf{r})$ outside the core region. The problem is now how to generate a replacement that would maintain the accuracy and transferability of the full, all-electron (AE) solution. The notion of transferability is here of a crucial interest as it guarantees that the pseudopotential constructed in particular environment (usually an isolated atom in the ground or excited state) will be reliably applicable in another environment (condensed matter, molecules, ions). There are several requirements for a "good" pseudopotential [70, 9]:

1. AE and PS eigenvalues are in mutual agreement for given reference configuration
2. AE and PS wavefunctions completely overlap beyond a chosen core radius R_c
3. logarithmic derivatives of AE and PS wavefunctions are equal at R_c
4. integrated charges inside R_c equal for AE and PS (norm conservation)
5. agreement of energy derivatives of the logarithmic derivatives

While the all-electron potential diverges close to nucleus and the true electron wavefunctions oscillate rapidly in the core region (necessary in order to satisfy the orthogonality constraints), the behavior of pseudopotential and pseudo wavefunctions below R_c is more smooth (see visualization in Fig. 1.2) - nodes of the wavefunction vanish while conserving the charge (thus norm conservation) and the singularity of the potential is replaced by a shallow minimum - the strong nuclear potential is screened by core-electrons.

Generation of norm-conserving pseudopotentials

In order to *ab initio* generate a pseudopotential one starts with a choice of the atomic configuration and performs the all-electron calculations independently for each $|l, m\rangle$ state of an isolated atom (or an atomic-like state) by self-consistently solving radial Schrödinger equation in terms of the all-electron atomic wavefunctions with given angular momenta. The Hamiltonian is composed of a Laplacian (in spherical coordinates), the nuclear Coulomb interaction term V_{ext}, the Hartree term $V_H(r)$ and the exchange-correlation potential $V_{XC}(r)$ (Hartree units):

$$\left[-\frac{1}{2}\frac{\mathrm{d}^2}{\mathrm{d}r^2} + \frac{l(l+1)}{2r^2} - V_{\mathrm{ext}}(r) + V_H(r) + V_{XC}(r)\right] \psi_{n,l}^{AE}(r) = \varepsilon_{n,l}\psi_{n,l}^{AE}(r) \qquad (1.20)$$

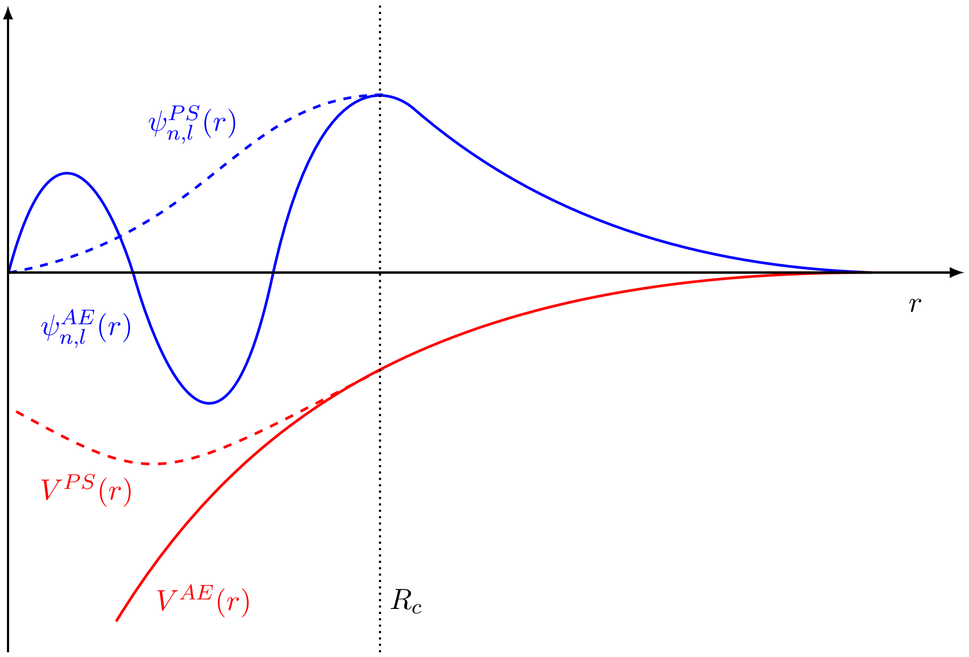

Figure 1.2: Schematic representation of the pseudopotential and valence pseudo wavefunction (dashed line) versus all electron potential and true wavefunction (solid line).

Subsequently, valence states are identified and a pseudo wavefunction $\psi^{PS}_{n,l}(r)$ is selected for the calculated all-electron wavefunction $\psi^{AE}_{n,l}(r)$ so that it satisfies the previously mentioned criteria for the arbitrarily chosen core radius R_c (sometimes also called *pseudoisation* radius). The exact form of the pseudopotential is therefore not unique which allows to select it with regard to optimum computational properties. The choice of R_c which is done separately for each l channel is especially important: while its smaller values lead to so-called "hard" potentials that provide better accuracy and transferability being, however, more computationally demanding, relatively large values of R_c lead to "soft" potentials with smooth wavefunctions that in plane-wave approach can be described with as few basis functions as possible and therefore tend to be more computationally efficient.

Several procedures of pseudopotential generation have been developed. Bachelet, Haman, Schlüter [71] and later Vanderbilt [72] assumed generic parametrized form of the pseudopotential and subsequently performed parameter-fitting procedure to obtain wavefunction with desired properties. Another approach detailed by Christiansen et al. [73] and Kerker [74] is to start with such pseudo-wavefunction ψ^{PS} and find the pseudopotential using inverted Schrödinger equation with all-electron energy. General tendency in solid-state applications is to make pseudo-wavefunctions as smooth as possible. Kerker assumed following analytic form of pseudo wavefunction:

$$\psi^{\mathrm{PS}}_{r<R_c}(r) = \mathrm{e}^{p(r)} \qquad p(r) \text{ - fourth order polynomial} \tag{1.21}$$

This approach has been extended by Troullier and Martins [75] through the use of higher order polynomial with coefficients selected to match derivatives of all-electron wavefunction and satisfy the constraint of norm-conservation. A number of other schemes evolved, most notably the dual-space Gaussian pseudopotentials [76]. The quality of the pseudopotential can be also improved by incorporating the scalar relativistic effects and the spin-orbit interactions. The approach of Troullier-Martins has been followed in the present work because of its conceptual simplicity and compatibility with the SIESTA code.

Tests of pseudopotentials

Apart from the verification of the compliance with the discussed earlier list of requirements it is always good practice and absolute necessity for custom-generated pseudopotentials to perform test calculations in selected, well-known situations and compare with available experimental data and other calculations.

Important feature of a pseudopotential is that while being generated for just one specific atomic configuration it is, at the same time, supposed to be transferable. The transferability means that it can still provide adequate description of an atom when the valence electronic configuration is varying within the limits that can be expected in the system in question [77]. Therefore, a number of different trial configurations must be tested by performing calculations with a chosen pseudopotential and comparing the results with the all-electron calculations conducted for the same trial configurations. The particular choice of trial configurations should be conditioned by the possibility of their occurrence in the target system. By considering all-electron calculation of these different configurations as a reference, one should check whether the pseudopotential calculation yields reasonable energies of valence states and properly reproduce the relative total energy differences between trial configurations which should be not affected by the choice of particular calculation scheme.

All choices made during the procedure of pseudopotential generation, in particular the electronic configuration of the atom, cut-off pseudoization radii and all other advanced features like core corrections must be verified by performing initial calculations for simpler systems with well known properties and adjusted accordingly. Finally it is also important to maintain the balance between accuracy and related computational overhead.

1.1.7 Deployment of the SIESTA method

SIESTA [34] is a widely used method (several thousands of users all over the world) to perform efficiently standard self-consistent Kohn-Sham DFT electronic structure calculations of molecules and solids. Its efficiency is tightly related to the use of localized basis sets. It can be used with a wide variety of exchange-correlation functionals (including GGA-PBE used in the present work) and besides the standard way of solving the generalized eigenvalue problem by direct diagonalization it also offers various order-N algorithms relying heavily on sparsity of Hamiltonian and overlap matrices. The latter feature, however, was not used in the present calculations. SIESTA is also capable of structural relaxation by moving the atoms in the aim to minimize the forces acting on them. Several algorithms are available e.g. conjugate-gradients and Broyden.

SIESTA calculations work flow

Practical implementation of DFT calculations with SIESTA is an iterative procedure that consists of the following steps [77] - some of them will be discussed in detail later:

1. selection of typical bulk configurations for testing: in case of a Co-Pt mixed systems the natural choice was pure Pt (fcc), pure Co (fcc/hcp) and CoPt ($L1_0$)
2. choice of exchange correlation functional and its particular parametrization
3. choice the basis set and associated parameters
4. preparation of pseudopotentials that conform to all the basic requirements detailed in previous section - this is to be done for all atoms separately
5. a number of test calculations for selected configurations with lattice constant(s) near the expected (experimental) values within a window of tolerance - for the magnetic systems spin-polarized calculations should be performed.
6. choose most energetically favorable value(s) by fitting Birch-Murnaghan equation of state to the energy *vs* unit cell volume relation
7. final relaxed calculations starting from the newly found lattice constants and derivation of basic bulk properties (bulk modulus, magnetic moment, energetical quantities, charges, densities of states)
8. comparison of the results with well known features of sample systems, results obtained from similar calculations and respective experimental data

These steps have to be repeated should the need for improvements arises. It is important to note that there is no *fitting the parameters* to experimental data - the choices that are made here are meant only to find a compromise between computational feasibility and the accuracy of calculations. Last, but not least while the real test for ab-initio method is always the comparison of the calculations with experimental data it is also advisable to perform some purely numerical tests where the convergence of self-consistent calculations can be verified.

Pseudopotentials for Co and Pt

For the ion-electron interactions, the core electrons are replaced by norm-conserving, improved Troullier-Martins pseudopotentials [75] with core corrections, factorized in the Kleinman-Bylander form [78] including scalar-relativistic effects. Pseudopotentials were generated with the aid of the program ATOM [79] developed by S. Froyen, N. Troullier, J. Martins and A. Garcia. This program was also used to perform basic tests. Atomic configurations and cutoff radii (in Bohrs ≈ 0.529Å) used for subsequent calculations:

Pt: [Xe] $\mathbf{4f^{14}}$ $\mathbf{5d^{9}}$ $\mathbf{6s^{1}}$ $\mathbf{6p^{0}}$ $\mathbf{5f^{0}}$

relativistic rc_s=2.65, rc_p=2.47, rc_d=1.53, rc_f=2.32

Co: [Ar] $4s^2$ $4p^0$ $3d^7$ $4f^0$

spin polarized rc$_s$=1.8, rc$_p$=1.9, rc$_d$=0.7, rc$_f$=0.2.

Core correction was provided with pseudo core charge density given by $r^2 \exp(a+br^2+cr^4)$ outside r_{pc}. For Co relevant parameters were $r_{pc} = 1.152$, $a = 4.630$, $b = -3.042$ and $c = 0.316$ (pseudo core charge of 10.1489 e) and for Pt $r_{pc} = 1.308$, $a = 4.730$, $b = -2.278$, $c = 0.171$ (pseudo core charge of 17.1443 e).

Fig. 1.3 and Fig. 1.4 illustrate the comparison between the results of all-electron and pseudopotential calculations performed for reference atomic configuration.

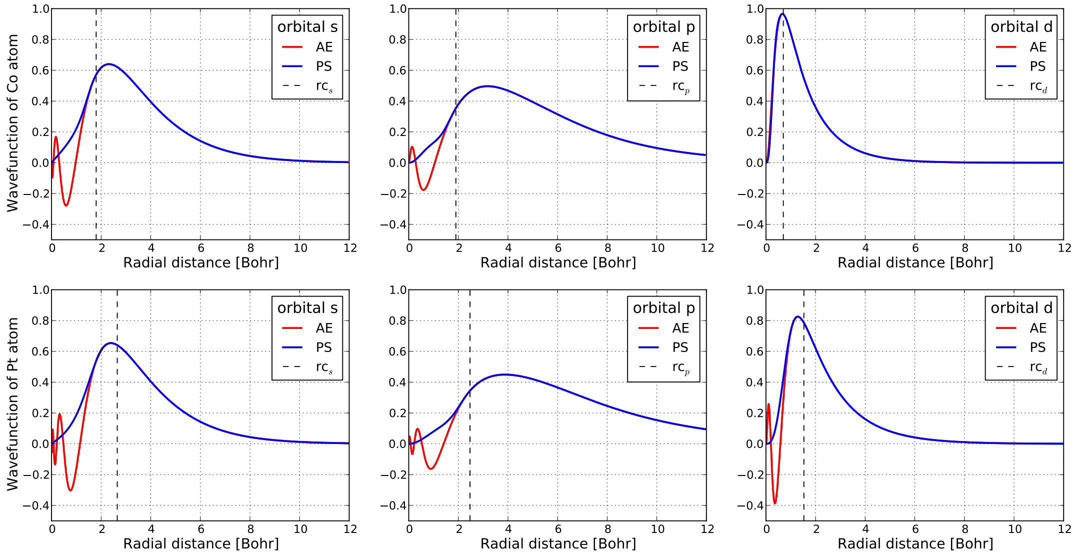

Figure 1.3: Visualization of all-electron (AE) wavefunctions and pseudo-wavefunctions (PS) as a function of radius (Bohr) for each orbital. One can observe that below cut-off radius (dashed line) AE wavefunction has nodes that vanish in PS case while above cut-off both functions are identical.

The choice of basis

Valence states are described using double-ζ polarized basis sets. For Pt, a DZP basis was used with two different radial functions to represent the 6s and 5d orbitals and one polarization 6p shell. For cobalt, a DZP basis was used with two different radial functions to represent the 4s and 3d orbitals and one polarization 4p shell.

Pt: 6s (double-ζ, polarized) 6p (single-ζ) 5d (double-ζ)

Co: 4s (double-ζ, polarized) 4p (single-ζ) 3d (double-ζ)

Fig. 1.5 illustrates the basis fine-tuning, here in the case of orbital-confining cutoff radii checked with the calculation of Pt bulk lattice parameter.

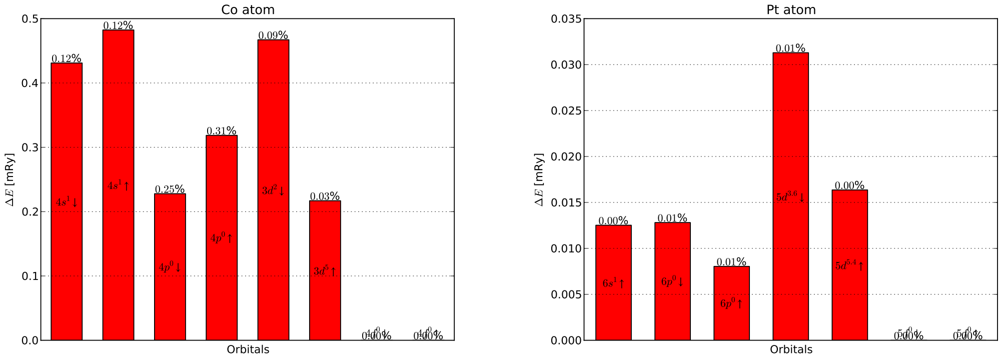

Figure 1.4: Comparison of orbital energies calculated with pseudopotential and those obtained from all-electron calculation. Differences are negligible (less than 0.5 mRy).

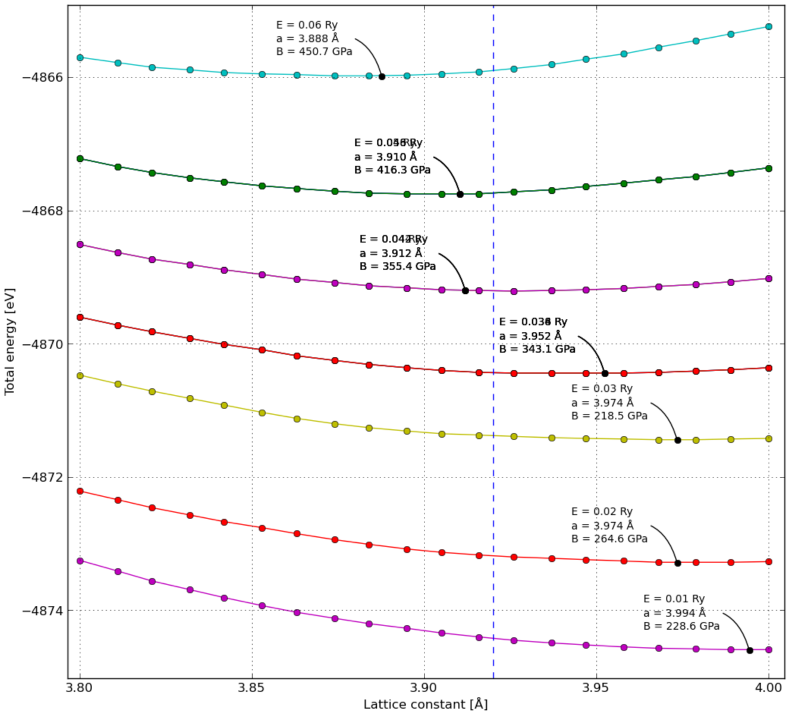

Figure 1.5: Example of basis fine-tuning. Calculation of pure platinum (fcc) lattice constant for bases generated with different orbital-confining cutoff radii.

Determination of lattice constants

In order to calculate the lattice constant let us consider the simplest case of pure fcc platinum. Several calculations of the total energy were performed for various values of the lattice constant taken within a few percent of tolerance around expected value. The relation between the unit cell volume and its energy is analyzed. This analysis is performed by fitting the integrated Birch - Murnaghan [80, 81] equation of state:

$$E(V) = E_0 + \frac{9V_0B_0}{16}\left\{\left[\left(\frac{V_0}{V}\right)^{\frac{2}{3}} - 1\right]^3 B_0' + \left[\left(\frac{V_0}{V}\right)^{\frac{2}{3}} - 1\right]^2 \left[6 - 4\left(\frac{V_0}{V}\right)^{\frac{2}{3}}\right]\right\} \tag{1.22}$$

where B_0 is bulk modulus and B_0' its pressure-derivative. The curve has a minimum at V_0 which corresponds to the optimized lattice constant (Fig. 1.6). Examples of the calculations in case of the complicated structures with more than one lattice constant can be found in literature e.g. [82, 4].

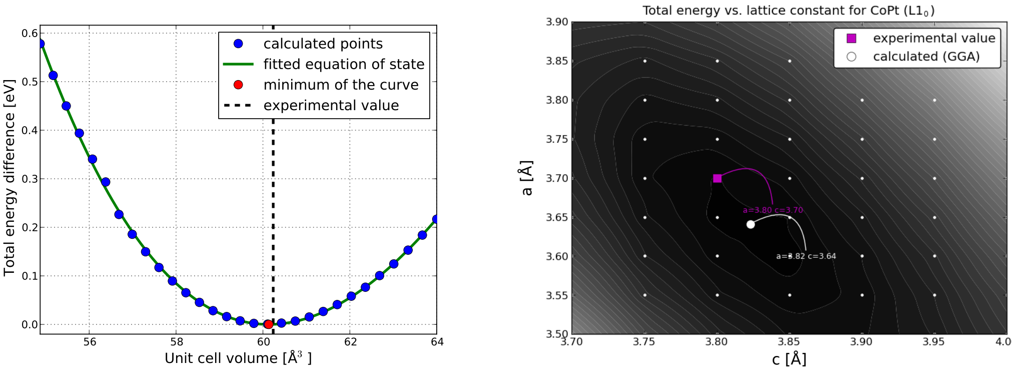

Figure 1.6: Example of lattice constant calculation in case of pure fcc platinum and total energy surfaces for a range of a and c lattice constants in case of $L1_0$ CoPt.

Charge analysis: Mulliken populations

The attribution of charge to a specific atom within DFT calculations is always somewhat arbitrary and one must remember that *pseudo*charge can only be calculated which is based on Kohn-Sham electronic density. There are no real atoms; there are only nuclei and a wavefunction and a charge density of electrons in the field of those nuclei. From the obtained spatial charge density, there are several different schemes of partitioning this charge density into sites or ”atoms” (see e.g. [83] for a more complete overview) and it is worth comparing the results from different methods in order to better understand what *”really happens”* in the system and to get some idea on the accuracy that can be achieved when willing to make charge analysis per sites (and possibly orbitals) with DFT. The two following methods, accessible within the use of Siesta, were considered:

- **Mulliken analysis** - since LCAO basis was used it is possible to simply project the charge on the basis functions associated with given atom and obtain the orbital charge directly [84]. In practice, the corresponding matrix elements of density and overlap matrices are multiplied to form the population matrix in such way, that electronic density from overlap matrix is partitioned equally between atoms. This method has the great advantage of simplicity and efficiency. Since it requires the use of an atom centered basis, the main drawback of this method will be its high sensitivity to the choice and optimization of that basis. It works best for small basis sets and in order to allow for charge comparisons the same basis sets must be used for all calculations. Mulliken populations can be obtained directly within SIESTA.

- **Bader analysis** - another approach that can only be used to calculate total charge on the atomic site is to take the spatial distribution of charge density and integrate it inside volumes corresponding to the sites. These volumes can be chosen either arbitrarily (e.g. spheres of certain radius, equal Voronoi tessellation) or based on Bader approach used in molecular calculations which is to find zero flux charge-density surfaces to divide atoms [85]. A program of A. Arnaldsson, W. Tang, S. Chill and G. Henkelman has been used [86, 87, 88].

The analysis of local magnetic moment also requires calculation of the charges associated with spin up and spin down electronic populations and will be performed within the Mulliken formalism. Additionally, since the distinction between spin up and spin down populations is purely conventional we will assume that spin up is represented by the majority of electronic population, that is, the total magnetic moment is always positive. This convention, applied universally, does not affect the generality of analysis and still can lead to negative local contributions to the magnetic moment.

Supercell scheme and periodic boundary conditions

The DFT calculations with SIESTA always involve the application of periodic boundary conditions due to the use of the supercell scheme. Therefore, in order to perform calculations for finite or spatially confined systems (clusters, surfaces) one must introduce proper amount of vacuum inside the supercell in order to exclude, unless intended, the interactions between periodic images of the same system. This is particularly important in SIESTA where default size of the supercell equals to the size of the system and, therefore, periodic boundary conditions are implied in all directions. This issue will be discussed in detail on the example of pure surface calculations in the next chapter.

Geometry optimization

The aim of this procedure is to find most energetically favorable atomic structure from arbitrary starting point. This is in fact the attempt to reincorporate into the calculations the movement of nuclei that was neglected within Born-Oppenheimer approximation. Atomic structure optimization is usually performed in three steps:

1. mentioned above determination of reference lattice constants for the bulk systems
2. for inhomogeneous systems a series of trial configurations are prepared and a configuration with lowest energy is used - the choice of these configurations depends heavily on the system in question e.g. in case of surface the starting point

would be to use proper bulk lattice constant for all sites and the distance between surface layer and deeper layers can be varied perpendicular to the surface

3. short-distance geometry fine-tuning can also be performed by a series of single point energy calculations in which the forces on nuclei are calculated using Hellman-Feynman theorem [89] and later used in the integration of equations of motion for nuclei allowing to move them towards equilibrium structure

The last step of geometry optimization is error prone due to the two factors. First, in case of incomplete basis set or changes of the supercell shape an error is introduced known as the Pulay force [90] and must be taken into account. Secondly, because of restrictions of multivariate optimization algorithms care must be taken i.e. one has to choose a starting point that leads to a global rather than a local minimum. Therefore all the above steps must be performed and last step is meant mainly for fine-tuning. It is common to perform initial structure determination with classical molecular dynamics.

Convergence of calculations and numerical tests

In numerical calculations there is always a trade-off between accuracy and computational resources spent on solving given problem. In order to make optimal choice one must conduct several tests. The aim of the convergence study is to determine the minimal (in the sense of least associated computational effort) value for given parameter of calculations that will not affect the accuracy. This can be done by analyzing the relevant system parameters (e.g. total energy or other relevant property of the system) as a function of the parameter of calculations. The value that does not yield further improvements should be chosen for subsequent calculations. One of the most important parameters in SIESTA are k-grid cutoff and mesh cutoff. The first one governs the fineness of the k-grid used for Brillouin zone sampling [10] using the method of choosing optimal grid developed by Moreno and Soler [91]. The second one is the equivalent for a plane wave energetical cutoff for the grid [10]. Example of the aforementioned analysis performed for those two parameters is given in Fig. 1.7 - convergence in terms of the total energy can be observed for increased mesh cutoff and k-mesh density.

The proper choice of the k-point sampling depends on the geometry of the system. For the most simple symmetrical bulk unit cell, in principle, as many as possible same number of k-points are taken in the three directions of the cell in order to describe the Brillouin zone. However considering asymmetrical slabs with surfaces, in the supercell scheme, one has to take different k-points numbers in order to keep a same density of k-points in the three directions of the system. Typically the first Brillouin zone of a surface is flat then it is sufficient to choose a two-dimensional mesh of $N_x \times N_y \times 1$ with an appropriate choice of N_x and N_y upon the dimensions of the cell. Finally for clusters, or more generally for isolated systems, the Γ point contains all the information and is sufficient to cover the first Brillouin zone. Considering more k points would lead to take into account the artificial periodicity of the system.

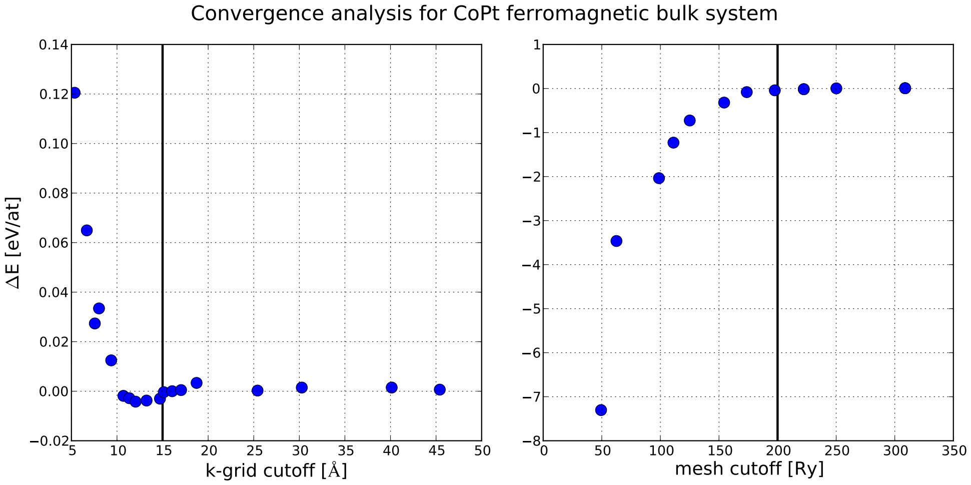

Figure 1.7: Example analysis of the impact of two critical parameters: mesh cut-off and k-grid cut-off [10] on the total energy of CoPt magnetic bulk system (vertical solid lines mark the choice made for the purpose of further calculations).

Another question is the convergence of self-consistent algorithm which can be improved by e.g. the choice of mixing scheme. In SIESTA three mixing schemes are available: linear mixing, Pulay convergence accelerator [68] and Broyden-Vanderbilt-Louie-Johnson mixing scheme [92]. Through mixing weight parameter one can control the proportions between the input and output density matrices in the density matrix to be used in next SCF cycle and for mixing schemes that use information from more than one SCF cycle the number of past cycles to consider [10].

1.2 Tight Binding approach

The tight binding method relies on the possibility to describe the electronic structure of a solid-state system by treating electrons as *tightly bound* to the atoms they belong. Every single electronic wavefunction can be represented as a linear combination of fixed atomic orbitals associated with particular atoms and therefore the method is best suited for studying systems where there is no significant overlap between orbitals (like *sp* valence electrons of semiconductors and *d* states of transition metals). The method was first developed by Bloch [93] for the simplest case of *s*-orbitals and then extended by several authors [94, 95].

1.2.1 The Tight-Binding Hamiltonian

An effective potential of N_n atoms can be approximated by a superposition of potentials associated with isolated, neutral atoms. Within this approximation the Hamiltonian of a single electron can be written in the following form:

$$\hat{H} = -\frac{1}{2}\nabla^2 + \sum_i^{N_n} V(|\mathbf{r} - \mathbf{R}_i|) = \hat{T} + \sum_i^{N_n} \hat{V}_i \qquad (1.23)$$

where $\hat{T}$ denotes the kinetic energy operator and $\hat{V}_i$ is spherically symmetric potential centered on site i located at $\mathbf{R}_i$. Within Tight-Binding Approximation (TBA) any one-electron delocalized wavefunction $\Psi_n(\mathbf{r})$ given by the Schrödinger equation $\hat{H}\Psi_n(\mathbf{r}) = E_n\Psi_n(\mathbf{r})$ can be expressed in terms of a linear combination of atomic orbitals (LCAO):

$$\Psi_n(\mathbf{r}) = \sum_{i,\lambda} c^n_{i,\lambda}\psi_\lambda(\mathbf{r}-\mathbf{R}_i) = \sum_{i,\lambda} c^n_{i,\lambda}\,|i,\lambda\rangle \tag{1.24}$$

where the index $\lambda = \{n,l,m\}$ enumerates atomic orbitals on site and $\psi_\lambda(\mathbf{r}) = \chi_{nl}(r)Y_{lm}(\hat{\mathbf{r}})$ is an atomic function with radial function $\chi_{nl}(r)$ multiplied by spherical harmonic $Y_{lm}(\hat{\mathbf{r}})$. The Schrödinger equation can be rewritten in the basis 1.24:

$$\sum_{i,\lambda} c^n_{i,\lambda}\hat{H}\,|i,\lambda\rangle = E_n\sum_{i,\lambda} c^n_{i,\lambda}\,|i,\lambda\rangle \tag{1.25}$$

The coefficients $c_{i,\lambda}$ can be determined by projecting $\langle j,\mu|$ on 1.25.

$$\sum_{i,\lambda} c^n_{i,\lambda}\underbrace{\langle j,\mu|\,\hat{H}\,|i,\lambda\rangle}_{H^{\lambda\mu}_{ij}} = E_n\sum_{i,\lambda} c^n_{i,\lambda}\underbrace{\langle j,\mu|i,\lambda\rangle}_{S^{\lambda\mu}_{ij}} \tag{1.26}$$

and solving for $|H^{\lambda\mu}_{ij} - ES^{\lambda\mu}_{ij}| = 0$. Usually a weak overlap of the orbitals is postulated where the overlap integrals $S^{\lambda\mu}_{ij}$ are vanishing quickly with the inter-site distance.

The Hamiltonian 1.23 can now be written down in the new basis $|i,\lambda\rangle$ and subsequently separated into two terms representing intra-atomic and interatomic interactions:

$$\hat{H} = \sum_{i,j}\sum_{\lambda,\mu}|j,\mu\rangle\,H^{\lambda\mu}_{ij}\,\langle i,\lambda| = \overbrace{\sum_{i}\sum_{\lambda,\mu}|i,\mu\rangle\,H^{\lambda\mu}_{ii}\,\langle i,\lambda|}^{\text{intra-atomic term}} + \overbrace{\sum_{\substack{i,j\\ i\neq j}}\sum_{\lambda,\mu}|j,\mu\rangle\,H^{\lambda\mu}_{ij}\,\langle i,\lambda|}^{\text{interatomic term}} \tag{1.27}$$

where the matrix element $H^{\lambda\mu}_{ij}$ can be expressed in the following way:

$$H^{\lambda\mu}_{ij} = \langle j,\mu|\,\hat{H}\,|i,\lambda\rangle = \langle j,\mu|\,\hat{T}+\hat{V}_i\,|i,\lambda\rangle + \langle j,\mu|\sum_{k\neq i}\hat{V}_k\,|i,\lambda\rangle \tag{1.28}$$

Since for an isolated atom the $|i,\lambda\rangle$ fulfill the Schrödinger equation $(\hat{T}+\hat{V}_i)\,|i,\lambda\rangle = \varepsilon_{i,\lambda}\,|i,\lambda\rangle$ the orthonormality of the basis $\langle j,\mu|i,\lambda\rangle = \delta_{i,j}\delta\lambda,\mu$ allows the above formula for the matrix element to be written in the following form:

$$H^{\lambda\mu}_{ij} = \varepsilon_{i\lambda}\delta_{ij}\delta_{\lambda\mu} + \langle j,\mu|\sum_{k\neq i}\hat{V}_k\,|i,\lambda\rangle \tag{1.29}$$

The matrix elements of the Hamiltonian contain three-component integrals involving two orbital states $|i,\lambda\rangle$, $|j,\mu\rangle$ and the potential V_k. These matrix elements can be classified to one of the following categories depending on the location of the atomic sites, on which they are centered:

- *one-center* - both orbitals and the potential are centered on the same site: e.g. $\langle i,\mu|\,\hat{V}_i\,|i,\lambda\rangle$ (the terms have symmetry of an isolated atom)
- *two-center* - (i) the orbitals are located on two different sites and the potential is calculated on one of them: e.g. $\langle i,\mu|\,\hat{V}_i\,|j,\lambda\rangle$ or (ii) both orbitals are centered on a single site and the potential is centered on a different one: e.g. $\langle i,\mu|\,\hat{V}_k\,|i,\lambda\rangle$
- *three-center* - both the orbitals and the potential are centered on different sites: e.g. $\langle i,\mu|\,\hat{V}_k\,|j,\lambda\rangle$ (these terms can be neglected here, V_k vanishes quickly with $\mathbf{r}$)

It is assumed that the *three-center* integrals can be neglected since the interaction over the orbitals centered on two different single sites and the potential centered on the third single site tends to be small compared to the *two-center* integral where it exerted directly on same site [96]. Within this assumption all the intra-atomic terms depend only on the displacement between two sites.

$$H_{ij}^{\lambda\mu} \underset{i\neq j}{\approx} \langle j,\mu|\sum_{i\neq j}\hat{V}_i\,|i,\lambda\rangle \tag{1.30}$$

Combining 1.27 with expression 1.29 one obtains the final form of the Hamiltonian:

$$\hat{H} = \sum_{i,\lambda}|i,\lambda\rangle\left(\varepsilon_{i\lambda}+\alpha_\lambda\right)\langle i,\lambda| + \sum_{\substack{i,j\\ i\neq j}}\sum_{\lambda,\mu}|j,\mu\rangle\,\beta_{ij}^{\lambda\mu}\,\langle i,\lambda| \tag{1.31}$$

where:

$\alpha_\lambda = \sum_{k\neq i}\sum_{\mu}\langle i,\mu|\,\hat{V}_k\,|i,\lambda\rangle$	-	shift of the atomic level due to the presence of the *crystal field* but usually neglected since it leads only to a small shift in the energy levels
$\beta_{ij}^{\lambda\mu} = \langle j,\mu|\,\hat{V}_k\,|i,\lambda\rangle$	-	interaction between the orbitals on different sites, also called *hopping integral* depending on the distance between the sites i, j and the orientation of the orbitals λ, μ.

When modelling end of transition series metals like Co and Pt one can restrict further considerations to orbitals s, p and d. In the case of two-center integrals there is a single axis of symmetry which connects both sites. Each orbital can be expressed as a linear combination of possible orthogonal orientations λ_γ with different angular momenta γ relative to this axis. The number of distinct alignments γ (denoted traditionally by σ, π and δ) depends on the symmetry of the orbitals involved. Therefore, it is possible to express $\beta_{ij}^{\lambda\mu}$ using integrals between the orbitals λ and μ for given alignment γ denoted $\lambda\mu_\gamma$ e.g. ddπ, spσ (see Fig. 1.8). This parametrization was first proposed by Slater and Koster [95].

The calculation of the hopping integrals $\beta_{ij}^{\lambda\mu}$ is usually restricted to the nearest-neighbors and therefore $\hat{H}$ can be represented by symmetric block matrix where the

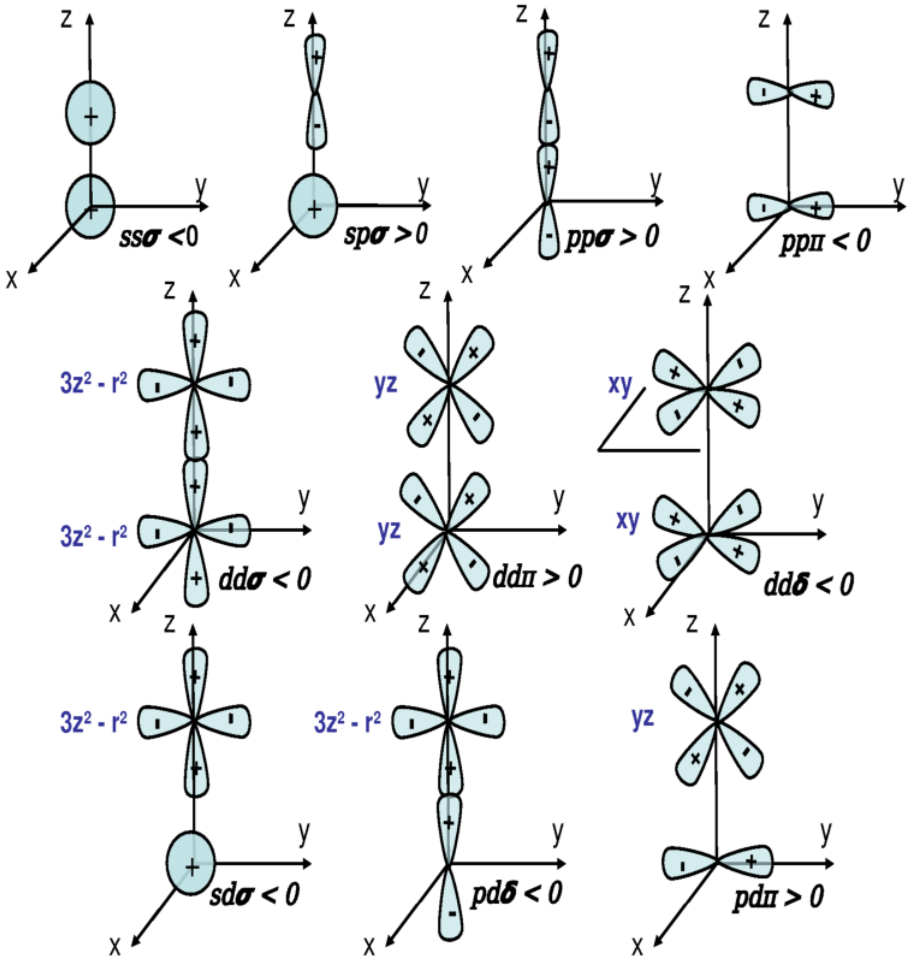

Figure 1.8: Visualization of the possible symmetric hopping integrals between two s, p and sp orbitals (first row), d orbitals (second row) and sd, pd orbitals (last row) [1].

blocks are defined for pairs of sites i, j so that they vanish when i and j are not first neighbors, for example:

$$\hat{H} = \begin{bmatrix} \varepsilon & \boldsymbol{\beta} & \mathbf{0} & \boldsymbol{\beta} & \dots \\ \boldsymbol{\beta} & \varepsilon & \mathbf{0} & \mathbf{0} & \dots \\ \mathbf{0} & \mathbf{0} & \varepsilon & \mathbf{0} & \dots \\ \boldsymbol{\beta} & \mathbf{0} & \mathbf{0} & \varepsilon & \dots \end{bmatrix} \tag{1.32}$$

where rows and columns correspond to atomic sites and each matrix block consists of a matrix with rows and columns corresponding to orbitals on the given sites. In the $sp-d$ case their dimensions are 9×9 (one s orbital, three p ones and five d ones):

0 - a zero matrix for sites located too far one from each other

$\boldsymbol{\varepsilon}_i$ - diagonal block of elements $\varepsilon_{\lambda\mu} = \epsilon_\lambda \delta_{\lambda\mu}$ where each ϵ_λ denotes the atomic level associated with the orbital λ on the site i

$\boldsymbol{\beta}_{ij}$ - a block of Slater parameters corresponding to the mutual alignment of orbitals on sites i and j, for the configurations where z-axis of the orbital functions contains i and j the block is diagonal, otherwise a rotation matrix must be applied

The $\boldsymbol{\beta}_{ij}$ block for two z-aligned d orbitals can be written down using Slater-Koster parameters:

$$\begin{bmatrix} dd\delta & 0 & 0 & 0 & 0 \\ 0 & dd\pi & 0 & 0 & 0 \\ 0 & 0 & dd\pi & 0 & 0 \\ 0 & 0 & 0 & dd\delta & 0 \\ 0 & 0 & 0 & 0 & dd\sigma \end{bmatrix} \tag{1.33}$$

The most important advantage of this method is the possibility to work in direct space and account for specific atomic configurations in a parametrized fashion without being forced to make use of the Bloch theorem.

1.2.2 Calculation of the Local Density Of States

The local density of states (LDOS) $n_i(E)$ for a given site i can be derived from $Tr\delta(E-H)$ using a projection of the Green function $G(z) = (z\hat{I} - \hat{H})^{-1}$ on $|i,\lambda\rangle$:

$$n_i(E) = \lim_{\eta \to 0^+} \left[-\frac{\mathrm{Im}}{\pi} \sum_\lambda \langle i,\lambda|\, G(E+i\eta)\, |i,\lambda\rangle \right] \tag{1.34}$$

Such projection of can be expressed in terms of a continued fraction [97, 98, 99]:

$$G_{ii}^{\lambda\lambda} = \langle i,\lambda|\, G(z)\, |i,\lambda\rangle = \cfrac{1}{z - a_1 - \cfrac{b_1^2}{z - a_2 - \cfrac{b_2^2}{z - a_3 - \cfrac{b_3^2}{\cdots}}}} \tag{1.35}$$

with coefficients a_n, b_n which can be derived either from the knowledge of the *first moments* of the density of states $n_i(E)$ or directly by tridiagonalizing Hamiltonian by means of *recursion method* which will be followed in the present work. The larger is the number of the coefficients used the better the formula 1.35 approximates $G_{ii}^{\lambda\lambda}$.

The "first moments" method

It is a well-known fact [100, 101] that a distribution can be derived from a finite number of moments, therefore $n_i(E)$ can be reconstructed from the knowledge of its p-order moments [97, 98]:

$$m_p(i) = \int_{-\infty}^{+\infty} E^p n_i(E) dE = \sum_{\lambda} \langle i, \lambda | \hat{H}^p | i, \lambda \rangle \tag{1.36}$$

Multiplying 1.36 by $\sum_{j,\mu} |j, \mu\rangle \langle j, \mu| = 1$ one finds that the moments of increasing order may be calculated by counting closed paths of the length p starting from the site i. The first moments of $n_i(E)$ possess simple physical meanings: m_0 is the total number of states (norm), m_1 describes the center of a gravity of the band, m_2 is associated with the mean width of the band and m_3 with its asymmetry and so on.

An increasing number of moments taken into account will allow obtaining an increasingly detailed LDOS. The advantage of this approach is that it gives the possibility to choose the level of accuracy depending on the treated problem. For instance, second moment approximation is sufficient to provide atomic interactions for use in atomistic simulations (Molecular Dynamics, Monte-Carlo). Going to fourth moment will allow more accurate studies of alloying effects possibly again in atomistic simulations, mainly Monte Carlo. In the present work higher levels of moments will be considered in order to study in more details the electronic structure in relation to structural (coordination) and alloying (chemical environment) effects.

The recursion method

The Hamiltonian $\hat{H}$ defined by 1.32 considerably simplifies when being represented in a new orthogonal basis of *pseudo-orbitals* $|n\}$. By means of the iterative Lanczos algorithm a basis is found that tridiagonalizes the $\hat{H}$ so that the matrix elements $\{n| \hat{H} |m\}$ are equal to zero for $n \in \{m-1, m, m+1\}$. One can assume the following form of the $\hat{H}$-matrix (elements are zero unless specified otherwise):

$$\hat{H} = \begin{bmatrix} a_1 & b_1 & 0 & & & \\ b_1 & a_2 & b_2 & 0 & & \\ 0 & b_2 & a_3 & b_3 & 0 & \\ & \ddots & \ddots & \ddots & \ddots & \ddots \\ & & 0 & b_{n-1} & a_n & b_n \\ & & & 0 & b_n & a_{n+1} \end{bmatrix} \tag{1.37}$$

which can be also written down in a compact form:

$$\hat{H} = \sum_n \big(|n\} \, a_n \, \{n| + |n\} \, b_n \, \{n+1| + |n-1\} \, b_{n-1} \, \{n| \big) \tag{1.38}$$

with coefficients $a_n = \{n| N |n\}$ and $b_n = \{n| H |n+1\}$ where $\{n| H |n+2, 3, \dots\} = 0$. The basis of $|n\}$ can be constructed recursively starting with $|1\} = |1\rangle$ (here, for the simplicity of notation only one orbital per site is considered) and following iteratively:

$$|n+1\} = \hat{H} |n\} - a_n |n\} - b_{n-1}^2 |n-1\} \tag{1.39}$$

The vectors determined in the above way need to be normalized by means of the factor $\sqrt{\{n|n\}}^{-1}$.

In the new basis the matrix $z\hat{I} - \hat{H}$ is also tridiagonal and can be easily inverted. Therefore, the matrix elements of $G(z) = (z\hat{I} - \hat{H})^{-1}$ can be expressed in terms of the coefficients a_n, b_n like in the 1.35 allowing the determination of the LDOS on given site.

The calculation of a_n, b_n coefficients is usually performed by constructing a recursion cluster around the site on which the LDOS is to be calculated. Such a cluster is composed of the shell of the nearest-neighbors of the site and the consecutive shells that are added to the cluster are build of nearest-neighbors of the sites from shell added previously (see Fig. 1.9). At each step of the recursion 1.39 a new pair of (a_n, b_{n-1}) coefficients is calculated and, therefore, for N pairs of coefficients a cluster of N shells must be constructed.

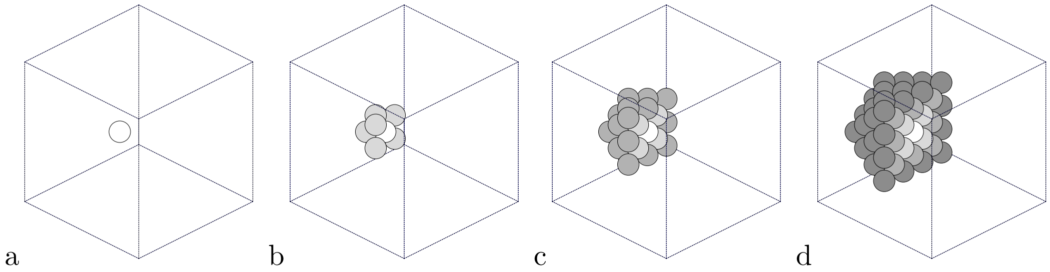

Figure 1.9: Construction of the recursion cluster for the fcc structure (cross-section). The number of coefficients and the size of the recursion cluster are directly related to the first moments approximation. Within the Second Moment Approximation the LDOS on a given site (a) depends only on its first neighbors (b). For the Fourth- and further Moment Approximations more recursion shells need to be considered (c,d).

In the case of infinite or semi-infinite systems the series of coefficients a_n, b_n is known to converge asymptotically towards a_∞, b_∞ respectively. Concrete calculations require that a practical and efficient termination is defined. It can be done by replacing the denominator of b_n in 1.35 with $\Gamma(z)^{-1} = z - a_\infty - b_\infty^2 \Gamma(z)$ and solving the second degree equation for $\Gamma(z)$:

$$\Gamma(z) = \frac{z - a_\infty - \sqrt{(z - a_\infty)^2 - 4b_\infty^2}}{2b_\infty^2} \quad \text{where} \quad z = \lim_{\eta \to 0} E + i\eta \tag{1.40}$$

Since LDOS is non-zero for E where $G_{ii}^{\lambda\lambda}$ has a non-zero imaginary part (compare 1.34) and the expression under the square root in 1.40 is negative the LDOS band edges can be easily determined: $a_\infty - 2b_\infty < E < a_\infty + 2b_\infty$ which defines a_∞ and b_∞.

The situation is somewhat different in the case of finite crystals. Indeed, in that case, the continuous density of states is replaced by a series of delta functions (atomic-like states), the number of which increases with the number of atoms N in the cluster. This implies that, in this case, instead of converging towards bulk asymptotic value b_∞, the b_n coefficients vanish beyond a given level N_c ($N_c < 9N$ for a spd system), which truncates the fraction at level N_c, leading to a discrete spectrum. However, for sufficiently large clusters, N_c is of the order of a few hundred of levels and the decrease of b_n coefficient only undergoes after a wide plateau around the value b_∞. Therefore, from a technical point of view, it is legitimate to use the bulk asymptotic values to terminate the continued fraction instead of truncating it at a level at which it would not be justified. Obviously this leads to a continuous density of states instead of a dense ensemble of delta peaks, which is numerically better conditioned to perform the integration involved in the calculations of both band fillings and energies.

The parameters ε and β are usually taken from the compilation of D.A. Papaconstantopoulos [102] designed for pure elemental solids. In the mixed A-B systems the hopping integrals β are calculated as average from those of pure metals [103] which is usual practice in the treatment of the electronic structure of alloys.

1.2.3 LDOS of inhomogeneous systems

The calculation scheme presented in the previous section is not complete for inhomogeneous systems with inequivalent sites having different LDOS where possible charge redistribution effects induced by the perturbation of LDOS must be considered. The site inequivalency with respect to the bulk site can be both due to a different coordination (surfaces, edges, vertices) and due to changes in the chemical environment brought about by the alloying effects. The charge changes modify the potential and affect the parametrization of the hopping integrals leading to the transferability problems. Some of the proposed solutions of this problem include: an explicit consideration of interatomic electron-electron interactions [104, 105, 106, 107], an application of self-consistent Green-function technique based on the TB-LMTO-ASA method [108], an implementation of the Ewald technique to account for the charge transfer [109] and an inclusion of long ranged Hartree contributions within a self-consistent adjustment of site-dependent occupation numbers [110].

Another approach, well known for its efficiency, is based on a second-order expansion of the DFT Kohn-Sham total energy with respect to charge density fluctuations and is known as the self-consistent charge density functional tight-binding (SCC-DFTB) method [111]. In this framework it is possible to fully account for the proper distribution of charge. One simpler approach is to use a local neutrality rule per site and orbital (s, p and d) of the system under study. Such rule has been successfully applied to the surfaces of transition metals [32] and extended to mixed cobalt-gold systems from DFT calculations [33]. It will be an important part of this thesis work to verify if such a rule applies to complex cobalt-platinum based systems. This should indeed significantly simplify the calculations and allow considering in an easier and more efficient way complex systems like nanoalloys. This choice is also motivated by the fact that the principle of charge neutrality has been widely used in literature in the derivation of alternative TB potentials e.g. within the Second Moment Approximation [112, 97, 98, 99, 113].

Self-consistent treatment of LDOS in the case of a surface

In the first approximation it can be assumed that in order to reach the self-consistency of charge it is sufficient to adjust only the atomic levels $\varepsilon_{i\lambda}$ [114] (Fig. 1.11). The task is to determine the shifts $\delta\varepsilon_{i\lambda}$ of the pure bulk atomic levels $\varepsilon_{0\lambda}$ so that the effective atomic level $\varepsilon_{i\lambda} = \varepsilon_{0\lambda} + \delta\varepsilon_{i\lambda}$ for each inequivalent site i satisfies the rules of self-consistency. Once the λ-projected LDOS $n_{i\lambda}(E)$ is calculated for a given $\varepsilon_{i\lambda}$ the total valence band filling per site N_i can be found by integrating of $n_{i\lambda}(E)$ up to the Fermi level E_F:

$$N_i = \sum_\lambda N_{i\lambda} = \sum_\lambda \int_{-\infty}^{E_F} n_{i\lambda}(E)dE \tag{1.41}$$

In addition, the total band filling per an inequivalent site can be defined: $N_i = \sum_\lambda N_{i\lambda}$ and the corresponding N_0 occupancies in bulk can be obtained using formula 1.41 for $n_{i\lambda} = n_{0\lambda}$ where LDOS $n_{0\lambda}(E)$ is calculated for an unshifted atomic level $\varepsilon_{0\lambda}$.

In the case of a pure surface built of an element for which only d electrons can be taken into account, it is sufficient to assume that regardless of the location of the site i (surface, step, stacking fault, ...) the d-band filling remains the same as in a pure bulk $N_{i,d} = N_{0,d}$ (the local charge neutrality) [114]. It has also been shown that all the inner electron energy levels rigidly follow this d-band shift (core level shifts) which has been evidenced by photoemission experiments [115, 116]. *Ab-initio* calculations concerning the Pd surfaces [32] shown that in the case of the late transition metals, where different types of orbitals and $sp-d$ hybridization must be taken into account, the neutrality rule has to be applied separately for s, p and d orbitals ($N_{i\lambda} = N_{0\lambda}$ for $\lambda \in \{s, p, d\}$). Therefore in all TB calculations presented hereafter these spd hybridizations will be taken into account (chapter 4).

In the self-consistent algorithm whose block diagram is shown in Fig. 1.10 the values of $\delta\varepsilon_{i\lambda}$ are varied until the calculated band fillings meet the above mentioned charge neutrality rules which can be defined eg. per site ($N_i = N_0$) and per orbital ($N_{i\lambda} = N_{0\lambda}$). In the simplest case of pure surfaces which is discussed here the Fermi level is given simply by the corresponding bulk value.

The method can be directly extended to pure clusters by applying the self-consistent procedure for each site of different coordination (core, facet, vertex and apex) [117]. The situation is more complicated in mixed A-B systems for which a rule of charge distribution has to be derived accounting not only for structural effects but also for alloying ones e.g. for all changes in chemical environment. As mentioned previously, it will be the aim of the following chapters to verify if a neutrality rule can be applied specifically to cobalt-platinum based systems, not only per site and orbital but also per species. This will be done by performing an extensive study of several cobalt-platinum based systems with the DFT-SIESTA method (chapters 2 and 3).

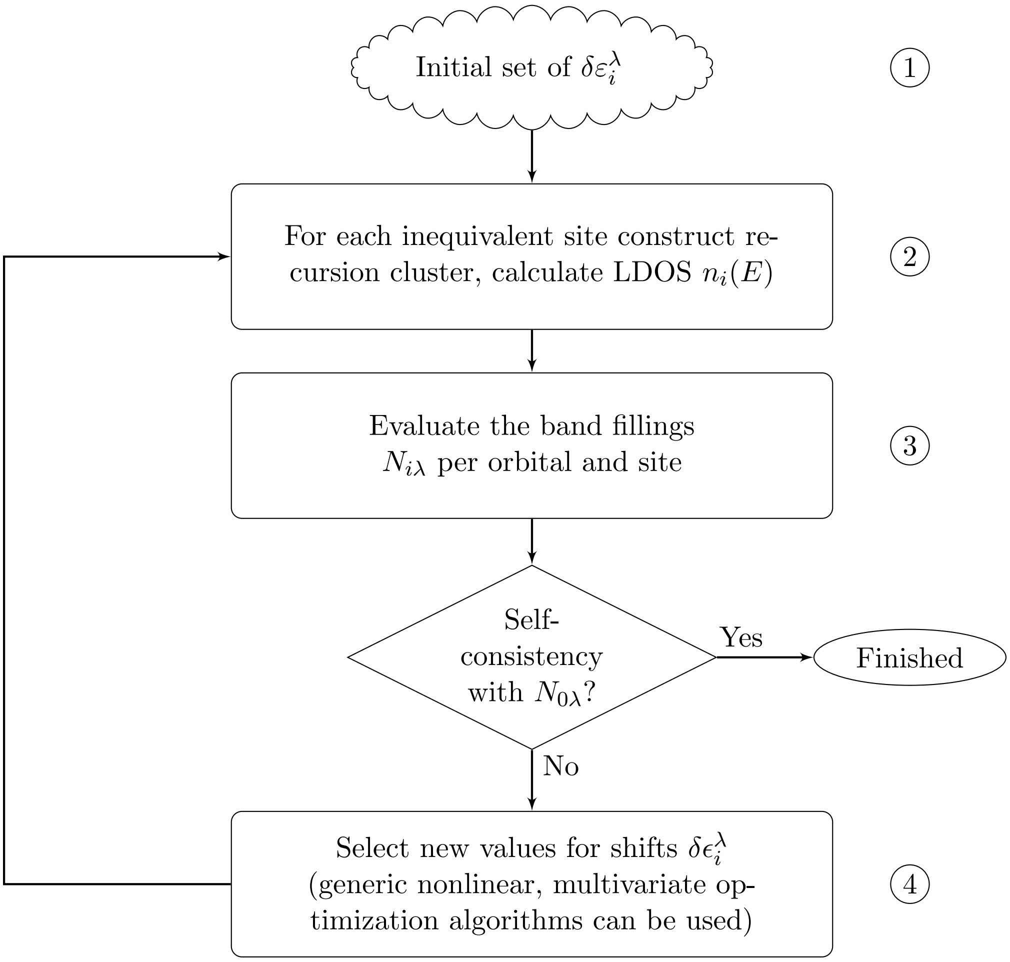
Initial set of $\delta\varepsilon_i^\lambda$
①
For each inequivalent site construct recursion cluster, calculate LDOS $n_i(E)$
②
Evaluate the band fillings $N_{i\lambda}$ per orbital and site
③
Self-consistency with $N_{0\lambda}$?
Yes
Finished
No
Select new values for shifts $\delta\epsilon_i^\lambda$ (generic nonlinear, multivariate optimization algorithms can be used)
④

Figure 1.10: The self-consistent algorithm for LDOS determination on sites whose local environment differs from bulk.

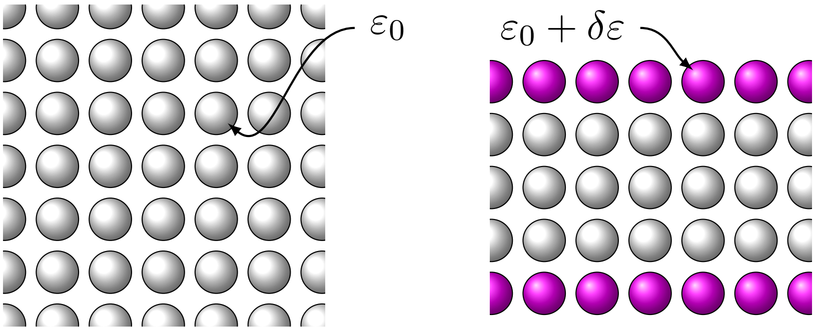
ε_0
$\varepsilon_0 + \delta\varepsilon$

Figure 1.11: In a pure bulk system all sites are equivalent (left) with atomic level ε_0. Atomic levels of surface sites (right) are shifted by $\delta\varepsilon$ due to the lower coordination.

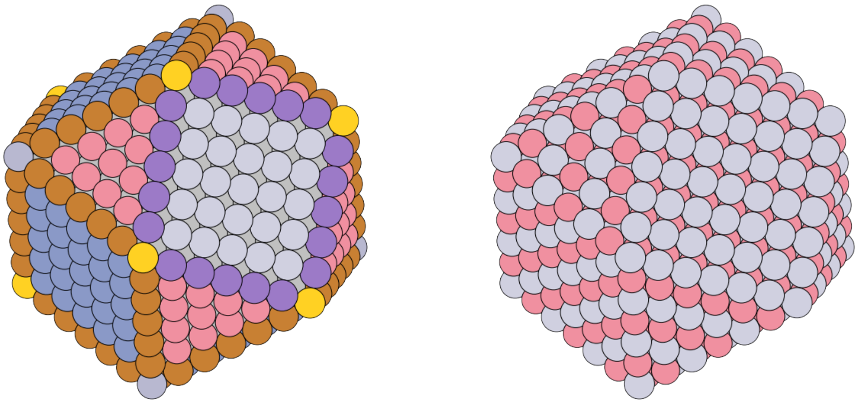

Figure 1.12: Sample classification of the sites in the case of cuboctahedral fcc cluster: topological classification of sites based on the coordination Z_i numbers (left, each color corresponds to a different class) and site occupancy for binary $A-B$ L1_0 ordered alloy (right, each color corresponds to a different atom type). The combination of those two factors give the full classification of inequivalent sites in the system (e.g. platinum site on mixed, (100) surface is classified with parameters $Z_i = 8$, $M_i = 6$, $X_i = \mathrm{Pt}$).

1.3 Inequivalent site classification

In order to account for different inequivalent sites in complex systems a systematic site classification rule must be applied. The approach adopted in the present work involves an analysis of the site neighborhood within the nearest-neighbors. For each site in the system three parameters are taken into account (see Fig. 1.12):

- the standard *site coordination number* Z_i - number of sites in first co-ordination shell, e.g. 12 - fcc bulk, 9 - fcc (111) surface, 5 - vertex of cuboctahedral cluster
- the *mixing rank* M_i - number of the nearest-neighbor sites around i-one occupied by atoms of a type different than the one residing on i, $M_i \leq Z_i$, e.g.. 6 - L1_0 bulk site, 4 - L1_0 alloy (100) pure surface, 6 - L1_0 alloy mixed (001) surface
- the *site occupation parameter* X_i - type of the atom that occupies given site

Results of DFT calculations performed independently for inequivalent sites show no significant variation of local electronic structure among sites classified as equivalent with respect to their first coordination shell which proves that the proposed method is sufficient. This classification will be therefore used for the analysis of DFT results (chapter 3) and for applying the self-consistent procedure in nanoalloys (chapter 4).

CHAPTER 2

DFT calculations of pure systems

In the following chapter the results of calculations performed for elemental cobalt and pure platinum systems will be presented. The calculations were performed systematically first for infinite bulk systems with fcc (Pt, Co) and hcp (Co) structure and later also for the spatially confined systems like Pt(111), Pt(100), Co(0001) surfaces and platinum clusters of sizes ranging from 13 to 561 atoms (up to 2.8 nm of diameter). The main objective was to study first the effect of the site coordination on the electronic structure: first separately from the alloying effects in mixed systems. The latter phenomena will be considered in the next chapter.

2.1 Elemental bulk systems

The results for bulk systems were treated mostly as a verification of the method and later used as a reference in the further analyses of more complex structures. It was therefore out of the scope to go into much detail into the study of elemental solids. The work presented here is rather focused on few basic properties and on the site charge distribution.

2.1.1 Basic properties

A number of properties were calculated and compared with available data gathered from the literature (both experimental and calculated with DFT). The results are summarized in the Tabs. 2.1, 2.2 and 2.3. Lattice constants were determined by minimization of the energy per unit cell volume (without thermal corrections). In order to obtain the bulk moduli the described earlier fitting of the Birch-Murnaghan equation of state was performed. The cohesive energies were calculated by subtracting from the obtained total energy per atom the value of the energy of an isolated atom. The calculations of an isolated atom involve definition of large, empty supercell with just single atom inside. In order to improve the accuracy it is advisable to include so-called *ghost atoms* in the positions normally occupied by the nearest-neighbors (typically, the correction is of the order of 0.1 - 0.3 eV). The zero-point vibrational energy contribution was neglected.

Comparison of our calculations (SIESTA-GGA) with the experimental values shows an overall reasonable agreement in terms of lattice constants, c/a ratio of hexagonal structure, magnetic moments and bulk moduli. The most notable discrepancies are the larger bulk moduli of Co hcp (by over 50%) and the systematically overestimated magnitude of cohesive energies.

Pt (fcc)	GGA-SIESTA	LDA	GGA	experimental
lattice constant [Å]	3.981	3.93	3.99	3.92
bulk modulus [GPa]	240	296.0		278
cohesive energy [eV/atom]	−6.38	−7.40	−5.55	−5.84

Table 2.1: Comparison of the properties of pure fcc platinum obtained in the present work (GGA-SIESTA), calculated with LDA (SIESTA code) [1], GGA (VASP code) [2] and experimental values [3].

Co fcc	Non magnetic			Magnetic			
	a	E_{coh}	B	a	E_{coh}	B	μ
LDA [2]	3.37	-8.03		3.43	-8.10		1.53
LDA-GGA [4]	3.46		260	3.53		216	1.64
GGA [2]	3.45	-5.01		3.52	-5.18		1.61
SIESTA-GGA	3.45	-7.59	285	3.51	-5.84	248	1.61
Experiment				3.55			1.61

Table 2.2: Comparison of the properties of pure fcc cobalt obtained in the present work (SIESTA-GGA), calculated with LDA [2], hybrid LDA-GGA [4], GGA [2] and experimental values [5, 6, 7]: lattice parameter a [Å], cohesion energy E_{coh} [eV/atom], bulk modulus B [GPa] and spin magnetic moment μ [μ_B/atom].

Co hcp	Non magnetic					Magnetic					
	a	c	c/a	E_{coh}	B	a	c	c/a	E_{coh}	B	μ
LDA [2]	2.39	3.86	1.62	-8.02		2.43	3.91	1.61	-8.13		1.50
LDA-GGA [4]	2.45	3.97	1.62		262	2.50	4.05	1.62		221	1.60
GGA [2]	2.45	3.95	1.61	-4.99		2.49	4.02	1.61	-5.20		1.58
SIESTA-GGA	2.44	3.95	1.62	-7.64	304	2.47	4.02	1.63	-5.85	263	1.57
Experiment						2.41	4.07	1.62	-4.50	191	1.58

Table 2.3: Comparison of the properties of pure hcp cobalt obtained in the present work with SIESTA-GGA, calculated with LDA [2], hybrid LDA-GGA [4], GGA [2] and experimental values [5, 3, 7]: lattice parameters a and c [Å], cohesion energy E_{coh} [eV/atom], bulk modulus B [GPa] and spin magnetic moment μ [μ_B/atom].

Looking closer to all data, the usual known differences between the use of GGA with regards to L(S)DA are found like the increase of lattice constant which is usually underestimated in L(S)DA calculations, the counterpart of this increasing being sometimes an overestimation of lattice parameter (see case of Pt here).

Another expected improvement related to the use of GGA with regards to L(S)DA is the reducing of the bulk moduli (usually overestimated in LDA by more than 10% for d-metals) and a much better estimation of total energies and energy of atoms leading to a reducing of the cohesion energies so that on the overall a better description of cohesive properties is achieved with GGA [118]. Cohesion energies are indeed, although still overestimated, lowered when using GGA or hybrid LDA-GGA [4]. Regarding bulk modulus B, for Pt a reduced value is indeed obtained with regards to LDA but now somewhat much reduced with regards to experiments. Conversely, for Co hcp, SIESTA-GGA still gives a much higher value of bulk modulus B than experiment (by about 50%). So far we could not explain this discrepancy. We can just mention here the extensive study of cohesive properties performed by G. Y. Guo and H. H. Wang [4] within an hybrid LDA-GGA method. Although their calculated value of B is also larger (by about 15%) than the experimental value, the authors neither give some explanation of this discrepancy.

GGA is also known to be more realistic for magnetic phases. For instance LDA is predicting a wrong ground state for iron, fcc instead of bcc [119, 120]. Spin magnetic moment is usually underestimated with LSDA which is to be paralleled with the reduced distances knowing that a general behavior in magnetic d-metals is an increase of spin magnetic moment with increasing interatomic distance. Finally, as already mentioned in the chapter describing methodologies, LDA is giving reasonable results if the electronic density is uniform but may lead to errors when the density is varying too much for instance for more open systems like small clusters in which we are particularly interested. For all these reasons we choose to use the GGA approximation in all the following studies.

We can observe also, in the case of Co, that magnetism has some influence on structural parameters since accounting for it leads to an increased parameter systematically whatever the method of calculation. It reduces also the bulk modulus. Things are less clear concerning cohesion energy. Regarding the evolution of the properties from non magnetic to magnetic state one can better see the effects of magnetism on structure through total energy *vs* volume curves as represented in Fig. 2.1. The results show that under sufficient pressure the ferromagnetic configuration of fcc Co is no more preferred over paramagnetic one - the difference between respective energies as well as magnetic moment decrease with unit cell volume.

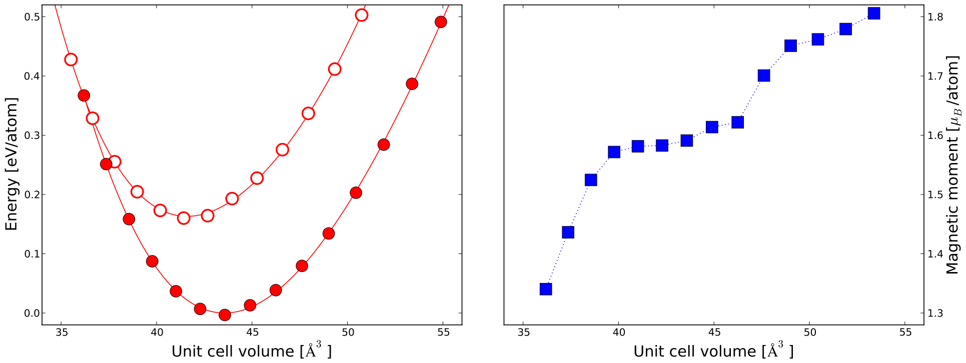

Figure 2.1: Total energy per atom for ferromagnetic (filled circles) and paramagnetic (hollow circles) fcc Co relative to the minimum energy of ferromagnetic case (left) and magnetic moment (filled squares) with respect to the unit cell volume.

2.1.2 Charge redistribution analysis

The investigation of charge redistribution is one of the main objectives of this part of the work. Partial atomic charges associated with each valence orbital s, p and d have been estimated using the Mulliken population analysis separately for each spin in the case of magnetic systems (Tab. 2.4). The placement of an atom in the crystalline lattice results in the interatomic charge transfer between orbitals. In the case of cobalt 70% of the charge associated with the s orbital is transferred to p and d orbitals. In the case of platinum the p charge in bulk consists of about 50% of the s charge and a small contribution from the d orbital. The total charge that is transferred between orbitals inside an atom is of the order of one electron. Since all the atoms in the fcc and hcp lattices are in equivalent positions there is no charge transfer between sites. Interestingly, the geometrical differences between the cobalt fcc and hcp lattices do not affect the charge redistribution.

		s [e]	p [e]	d [e]	$\sum$ [e]
Co (magnetic)	isolated	2.00 1.00↑ 1.00↓	0.00 0.00↑ 0.00↓	7.00 5.00↑ 2.00↓	9.00 6.00↑ 3.00↓
	fcc bulk	0.59 0.28↑ 0.31↓	1.09 0.51↑ 0.58↓	7.32 4.51↑ 2.81↓	8.99 5.30↑ 3.80↓
	hcp bulk	0.61 0.29↑ 0.32↓	1.06 0.49↑ 0.57↓	7.33 4.51↑ 2.82↓	9.00 5.28↑ 3.72↓
Co (non magnetic)	isolated	1.81	0.00	7.19	9.00
	fcc bulk	0.60	1.04	7.35	9.00
Pt (non magnetic)	isolated	1.34	0.00	8.66	10.00
	fcc bulk	0.65	0.97	8.39	10.00

Table 2.4: Comparison of the charge distribution between orbitals in the case of an isolated atom and an atom inside an infinite bulk. Total site charge is given in the last column.

2.1.3 Band structure and the density of states

The calculated band structures (Fig. 2.2) correctly predict metallic character of the investigated systems. The density of states of cobalt (Fig. 2.3b) exhibits a strong ferromagnetic behavior as the minority spin (spin down) band is shifted towards higher energies and partially unoccupied while the majority spin (spin up) band is full. There are no significant differences between cobalt densities of state in fcc and hcp variants.

2.2 Low-coordinated systems: pure surfaces

The infinite bulk considered in the previous section is, of course, an approximation and idealization of a real, spatially confined solid state system in which the interface between the body and its surroundings (vacuum in the simplest case) need to be taken into account. The existence of a surface modifies the structural and electronic properties of the material. Understanding of these modifications is a key step towards the studies of nanometer-sized clusters where surface effects are expected to

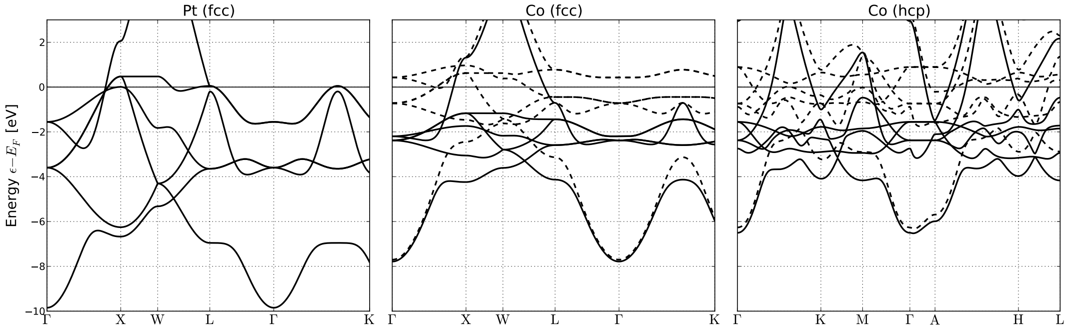

Figure 2.2: Band structure of Pt (fcc), Co (fcc) and Co (hcp) at high-symmetry points.

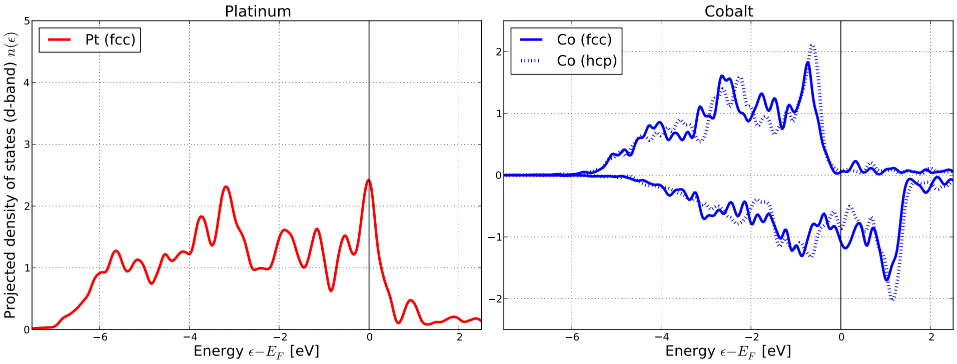

Figure 2.3: Projected d-band density of states of pure platinum (fcc - nonmagnetic) and cobalt (fcc, hcp - magnetic). Energies are shifted by respective Fermi levels E_F.

be predominant. Pure surfaces have been already studied in many works, theoretically and experimentally [121, 116]. Considering them also here opens an opportunity of comparison with available literature data and of justifying the transferability of the present calculations.

The following surfaces were chosen for analysis: Pt(100), Pt(111) and Co(0001). The calculations were performed for slabs of the thickness varying from 4 to 10 atomic layers (up to $1.8 - 2.0$ nm depending on the system). The supercell scheme (Fig. 2.4a) was applied with periodic boundary conditions defined in such a way that the amount of vacuum between the images ruled out the self-interaction. The exact vacuum size has been chosen after several test calculations. The total energy of a 10-layer slab of Pt(111) calculated with 1, 3, 4 and 6 nm of vacuum was slightly decreasing up to 4 nm. The total variation was, however, less than 0.6 meV and finally, the vacuum size of 4 nm was chosen for further calculations[1]. The number of atomic layers in the slab should be also sufficiently large to ensure that the interaction between its two symmetrical surfaces is negligible through the slab. The critical thickness was found to be of six atomic layers. Since the considered surfaces do not undergo significant reconstruction only the distance between the surface layers and the rest of the slab has been optimized with respect to the energy for each slab thickness - the procedure is detailed in Fig. 2.4b. Only in the case of Pt(100) the relaxation of the surface layer occurs within a significant amount with an inward relaxation by almost 1% of the bulk interlayer. This result slightly varied with the slab thickness.

---

[1] the enlargement of the unit cell only slightly increases the calculation time in the case of the use of localized basis sets, it was then advisable to take some safety margin in the choice of vacuum size

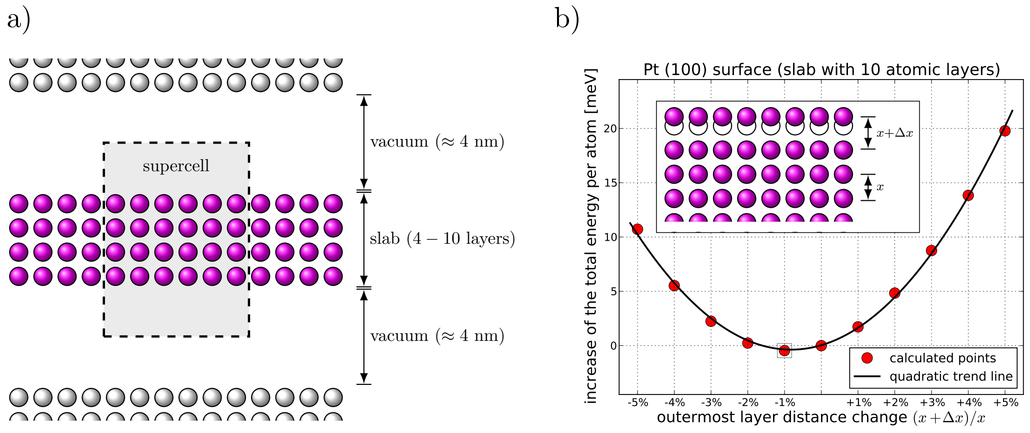

Figure 2.4: Pure surface calculations: a) the supercell scheme b) the surface layer distance optimization (example result for Pt(100) slab of 10 atomic layers, ∼ 1.8 nm).

2.2.1 The surface energy

Surface can be considered as a defect and it is associated with an increase of the total energy of the system. This extra surface energy γ of a clean surface can be calculated in the supercell scheme as the difference per unit area between the total energy of the slab E_{slab} and the total energy of the corresponding bulk E_{bulk} with the same number of atoms.

$$\gamma = \frac{1}{2A}(E_{\text{slab}} - E_{\text{bulk}}) \tag{2.1}$$

where A is surface area of a single slab facet, the factor 2 being associated to the presence of two symmetric surface in the chosen slab geometry.

surface	γ [eV/at]	γ [J/m^2]	γ_{exp} [J/m^2]
Pt(100)	1.10	2.22	2.48 [122]
Pt(111)	0.79	1.85	
Co(0001)	1.06	3.19	2.55 [122]

Table 2.5: Surface energies of Pt(100), Pt(111) (nonmagnetic) and Co(0001) (magnetic) surfaces calculated in the supercell scheme with 6-layer slab.

While the relations between surface energies ($\gamma^{\text{Co}}_{(0001)} > \gamma^{\text{Pt}}_{(100)}$ and $\gamma^{\text{Pt}}_{(100)} > \gamma^{\text{Pt}}_{(111)}$) are correctly reproduced (in J/m2) the absolute values are underestimated for Pt and overestimated for Co compared to the experimental data which might be related to the fact that only the relaxation for surface layer was performed and the obtained values are prone to numerical errors due to the comparison of large numbers whose difference is three orders of magnitude smaller. While on one hand close agreement between DFT calculations and experimental values could hardly be expected even between different types of ab initio calculations a wide spectrum of values is observed. On the other hand, the experimental value is a macroscopic average quantity obtained in the liquid state at low temperature and then extrapolated using a phenomenological approach developed by A. R. Miedema *et al.* [122]. Thus uncertainties about the determination of a single exact value of a surface energy are present on both experimental and theoretical sides. This topic is extensively discussed in the work of S. Karoui [123].

2.2.2 Charge redistribution: towards the neutrality rule

It is a well known fact that in the case of a pure metal the electronic charge on the surface is the same as the charge in the bulk not only per site but also per orbital [32]. This conclusion is also validated in the present work for Co and Pt cases. Tab. 2.6 compares the Mulliken charges associated with an atom on the surface and another one inside the slab, located the nearest possible to the geometrical center of the supercell. The first observation is that the charges calculated inside the slab are perfectly consistent with those derived previously from the bulk calculations (see Tab. 2.4) which justifies the choice of the slab thickness. While estimating the accuracy of the method around 0.1 eV and admitting that a variation of charge of this order is negligible, it can be stated that for all calculated systems the total charge on the site does not change with its coordination. There is, however a small charge redistribution between p and d orbitals. In the case of Co(0001), the local magnetic moment at the surface is increased by 0.17 μ_B/atom compared to the bulk which is evidently related to the loss of coordination at the surface.

		s [e]	p [e]	d [e]	$\sum$ [e]
Pt (100)	surface	0.68	0.80	8.45	9.93
	interior	0.65	0.97	8.39	10.00
Pt (111)	surface	0.68	0.83	8.43	9.94
	interior	0.65	0.97	8.39	10.00
Co (0001)	surface	0.71 0.34↑ 0.37↓	0.99 0.45↑ 0.54↓	7.31 4.58↑ 2.73↓	9.01 5.37↑ 3.64↓
	interior	0.61 0.29↑ 0.32↓	1.06 0.49↑ 0.57↓	7.33 4.51↑ 2.83↓	9.00 5.28↑ 3.72↓

Table 2.6: Comparison of the charge distribution between orbitals on the surface sites and the interior of the slab for different surface orientations.

An example of charge redistribution profile between sites located along the z axis (perpendicular to the surface) in the case of Pt(100) is shown in Fig. 2.5a. It allows to get a deeper insight into how the site charge is modified by the surface and in particular, what is the scale and the range of this effect. As it was already pointed out the total charge of sites slightly decreases near the surface, but is still inside the tolerance region of 0.1 eV. Clearly, the charge is simply shifted to the sites located deeper inside the slab and only the first three layers seem to be affected. There is also small charge transfer taking place between orbitals on a single surface site, but it is also negligible. It is worth pointing out that the relaxation of the surface layer does not affect the charges (see Fig. 2.5b) and therefore, the process is mainly due to the change of the site coordination and not the distance between sites.

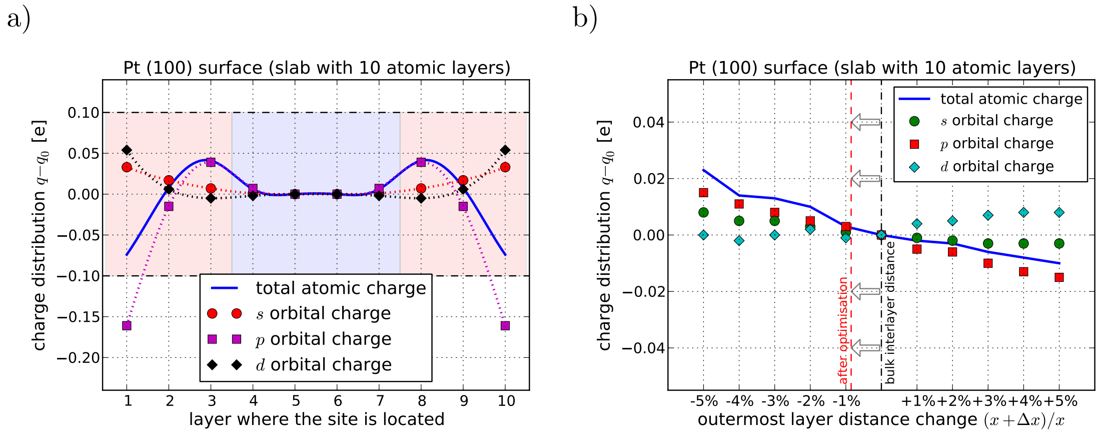

Figure 2.5: In-depth charge redistribution analysis in the Pt(100) case: a) charge redistribution profile along the axis perpendicular to the surface, y axis represents the difference between the orbital/site charge q on a given site and the corresponding bulk value q_0; the red (blue) region marks the surface (bulk) sites. The lines are arbitrarily fitted eye-guides; b) charge changes on the surface layer with respect to its distance from the slab - in all cases the charge redistribution is negligibly small.

2.2.3 Density of states on surface sites

The lower site coordination is reflected by the changes of the local electronic structure. Differences between the d-band LDOS (which is the most significant in case of transition metals) calculated on the surface sites and inside the slab are shown in Fig. 2.6. In the case of platinum the center of gravity of the LDOS (marked by vertical line of the same style) is noticeably shifted towards higher energies - 0.72 eV in case of Pt(100) and 0.55 eV for Pt(111). This shift is clearly due to the fact that the charge has to be preserved at the surface with regard to bulk (neutrality). The reducing of bonds number at the surface leads itself to the decrease of band width which without any associated band shift towards higher energies would lead to an excess of charge at the surface. This rationale holds for all d-metals having in the bulk a more than half filled d-band. For metals with less than half filled bands the shift occurs toward lower energies. In case of Co(0001) surface the first LDOS peak is more emphasized at the expense of flattening of the second one.

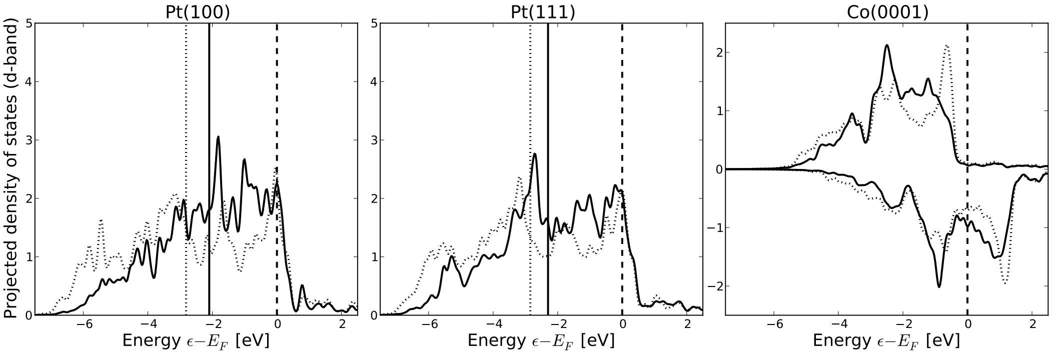

Figure 2.6: Projected d-band density of states of pure platinum and cobalt surfaces, dashed line represents bulk LDOS. Energies are shifted by respective Fermi levels E_F.

2.3 Finite size systems: pure platinum clusters

Study of surfaces presented in the previous section was an important intermediate step towards the investigation of finite size systems namely clusters or nanoparticles. In the supercell scheme used in DFT the system is therefore a cluster of atoms placed in a vacuum of sufficiently large spans in all directions in order to effectively isolate it from its images introduced by the application of the periodic conditions inherent to DFT procedure of calculation. In the present work a cubic supercell of fixed dimensions $14 \times 14 \times 14$ nm was used which resulted in at least 12 nm of spacing between the periodic cluster images in each direction[2]. Because the main objective here is to study charge distribution, which, as previously shown is negligibly affected by near-surface relaxations (Fig. 2.5b), highly symmetric, model configurations were considered with no structural optimization the latter increasing considerably computational time.

2.3.1 Cluster configuration

The calculations were performed for cuboctahedral and icosahedral clusters of N atoms built by growing around a central atom n shells of first neighbors while obeying the following law for closed shells clusters:

$$N = \frac{1}{3}\left(10n^3 + 15n^2 + 11n + 3\right) = 13,\ 55,\ 147,\ 309,\ 561,\ \ldots \qquad (2.2)$$

The above restriction indeed guarantees the possibility to construct perfect, n-shell clusters of desired shape with fcc structure (see Tab. 2.7). In the case of icosahedra the fcc lattice, however, is distorted and the distances between $30-40\%$ of neighboring sites are decreased by 5.1% (see [124] for discussion of the structure). The presented calculations were performed for relatively small clusters (up to $n = 5$ which corresponds to a cluster of 561 atoms with a diameter lower than 3 nm).

Several low-coordinated sites can be classified on the cluster surface depending on the geometry: surfaces of various orientations, edges and vertices (Fig. 2.7). Due to

---

[2] cluster calculations are very time-consuming, therefore instead of systematic analysis of the amount of vacuum the supercell size was chosen with large margin of safety after simple charge density analysis

	cuboctahedron	**icosahedron**
crystal structure	fcc (nearest-neighbor shells)	fcc (Mackay variant)
(100) square facets	6	-
(111) triangular facets	8	20
edges / vertices	24/12	30/12

Table 2.7: Summary of the calculated cluster geometries. The table indicates, for the two considered shapes, the total number of (100) and (111) facets, edges and vertices.

the different local environment the particular sites are expected to modify electronic structure as it was already observed in the case of simple surfaces. Such modifications are responsible for higher local reactivity that leads to interesting catalytic properties of pure platinum clusters [125].

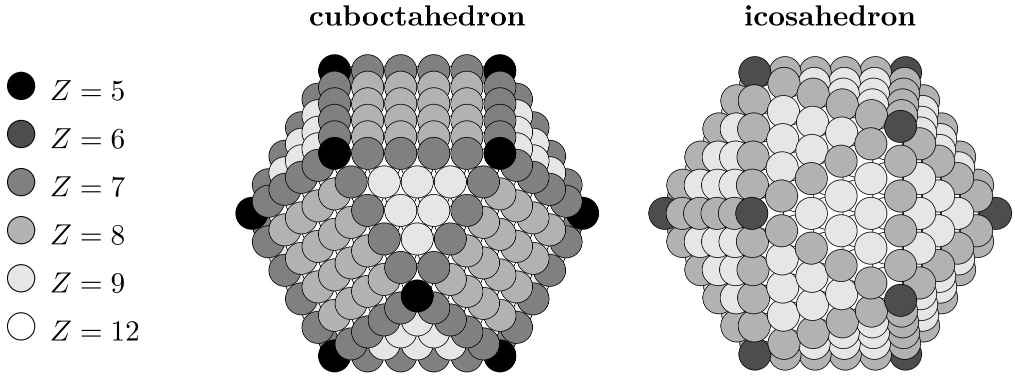

Figure 2.7: Low-coordinated sites in cuboctahedral and icosahedral clusters: (111) surfaces ($Z = 9$), (100) surfaces ($Z = 8$), edges ($Z = 7, 8$) and vertices ($Z = 5, 6$).

2.3.2 Energetically favored structures

With two alternative morphologies for a given cluster size a natural question raises on which morphology is energetically favored. Since the fcc structure inside icosahedral clusters is distorted one can expect that for large clusters, where the bulk-like contribution to the total energy is larger the cuboctahedra should be preferred; the distorted structure being more favorable for smaller clusters e.g. [126]. In fact, the preference for fivefold symmetry structures in case of small particles instead of fcc structure found in bulk metals is a very typical case of size effect. Icosahedral or decahedral shapes and their truncated variants with surfaces consisting of only (111), close-packed faces tend to be more energetically favorable than shapes in which also (100) faces are present. On the other hand, clusters fcc crystal lattices tend to have octahedral or truncated octahedral shapes. In the case of octahedral clusters pure (111) surfaces are observed as well, but these shapes have significantly lower volume to surface area ratio. This ratio is improved for truncated shapes, like cuboctahedra, but at the price of highly energetic (100) faces [127]. Results of the calculations support this reasoning - in the case of clusters smaller than 147 atoms the total energy per atom for the icosahedral shape is lower than for the cuboctahedra (Fig. 2.8).

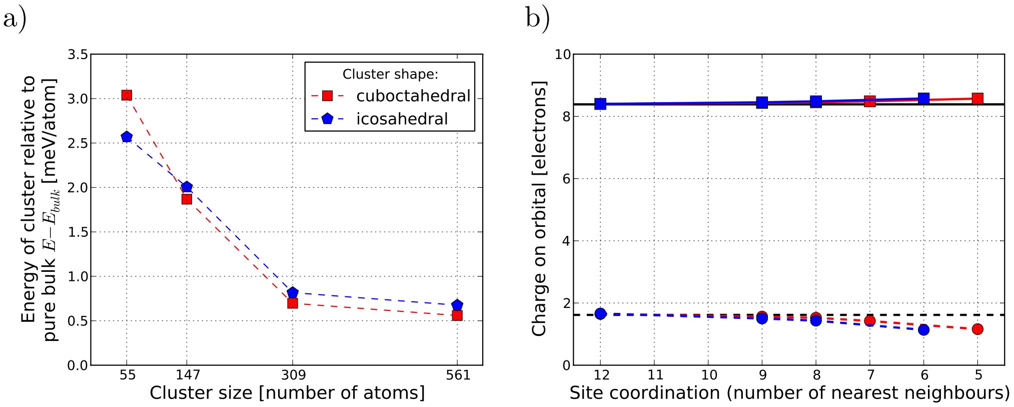

Figure 2.8: a) Total energy per atom of a Pt cluster (normalized to the analogous energy in bulk as a function of size b) Charge redistribution on the low-coordinated cluster sites as a function of the site coordination number for d orbitals (squares connected with solid lines) and $s + p$ orbitals (circles connected with dashed lines) for cuboctahedral (red) and icosahedral (blue) clusters. Black lines correspond to the reference bulk values. The result was obtained for a cluster of 561 atoms by averaging over all the equivalent sites (with the same coordination number).

2.3.3 Charge redistribution on surfaces, edges and vertices

The most significant charge modification is expected on the lowest coordinated sites with $Z \leq 8$ (edges and vertices). The Mulliken analysis results summarized in Tab. 2.6 support this hypothesis, however, even for these sites the total charge is decreased in the worst case by less than 0.3 electron compared to the charge on fully coordinated site inside the cluster. Edges and vertices are more subject to charge transfer and the charge that is transferred from these sites originates mostly from the p orbital. Small fraction of the p orbital charge (less than 0.2 electron) is also transferred to the d orbital on the same site. In order to visualize the charge transfer from the different surface sites towards underlying sites a sectional view of two Pt clusters, respectively cuboctahedral and icosahedral, is represented in Fig. 2.9. We then observe that charge redistribution follows the scheme observed in case of surfaces - there is a small charge transfer from surface sites (lighter) towards the lower atomic layers (darker) mainly the two first underlayers. The charge inside cluster is not modified (gray).

2.3.4 Density of states on clusters

Typical densities of states (d-band PDOS) of such clusters are represented in Fig. 2.10 for a Pt cuboctahedron and a Pt icosahedron both of 561 atoms. These PDOS present a narrowing with decreasing site coordination (from facets to edges and vertices) and

	cuboctahedron					icosahedron				
	Z	s [e]	p [e]	d [e]	$\sum$ [e]	Z	s [e]	p [e]	d [e]	$\sum$ [e]
interior	12	0.67	0.98	8.40	10.05	12	0.67	0.99	8.40	10.06
(111) surface	9	0.71	0.85	8.43	9.99	9	0.69	0.82	8.45	9.95
(100) surface	8	0.69	0.83	8.45	9.98	-	-	-	-	-
edge	7	0.70	0.72	8.48	9.91	8	0.69	0.74	8.48	9.92
vertex	5	0.71	0.45	8.57	9.73	6	0.69	0.45	8.58	9.71

Table 2.8: Comparison of the charge distribution between orbitals inside the Pt cluster and on particular surface sites along with the site coordination Z. The results were obtained for a cluster of 561 atoms by averaging over all the equivalent sites (with the same coordination number).

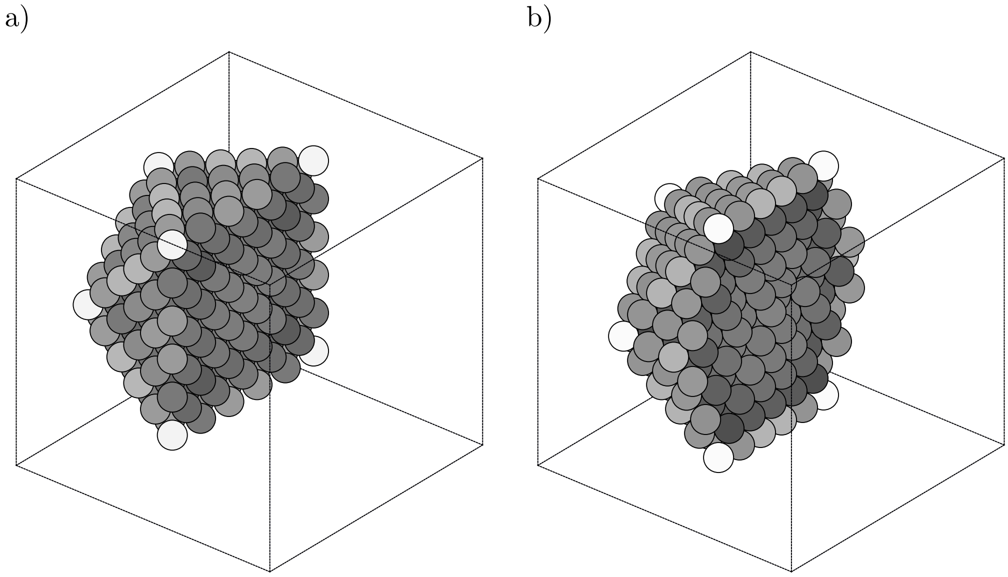

Figure 2.9: Total site charge variation profile with respect to bulk for a) cuboctahedra b) icosahedra (cross section, the gray scale corresponds to the amount of charge from -3% (white) to +3% (black) of bulk value. The charge redistribution follows scheme observed in case of surfaces - there is small charge transfer from surface sites (lighter) towards lower atomic layers (darker). The charge inside cluster is not modified (gray).

are significantly modified near the Fermi level. The density of states at the Fermi level $n(E_F)$ remains, however, unchanged. These modifications are some of the indicators that local properties (magnetic or catalytic) may change when going from bulk to nanoalloys and probably also when changing the size of clusters. These densities are in qualitative agreement with those calculated by C. Mottet [117] with Tight-Binding formalism using a local neutrality rule per site and orbital. This is already an indication that the local neutrality rule verified for surfaces is also extendable to pure clusters with different inequivalent sites upon coordination.

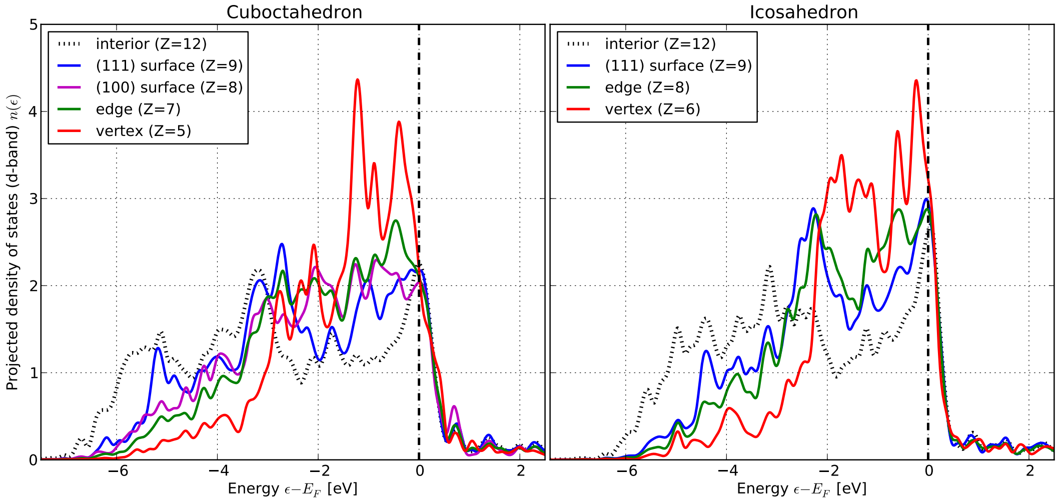

Figure 2.10: Projected d-band density of states on various low-coordinated sites on pure platinum clusters. Energies are shifted by respective Fermi levels E_F.

2.4 Conclusions

The calculated basic properties of pure bulk systems show an overall reasonable agreement with the experimental data and other calculations. The results obtained in the case of cobalt correctly predict a decrease of the magnetic moment with pressure leading eventually to the paramagnetic transition. In the case of pure surfaces the mutual relationships between surface energies were correctly reproduced. In this framework we have discussed the differences between the values usually obtained with the GGA and L(S)DA which allowed to explain some of the observed discrepancies and to justify the choice of GGA. Additionally, the study of the energetics of pure Pt clusters properly identified that the icosahedral shape is preferred over the coboctahedral one in the case of small clusters while for larger structures this preference is reversed. We have then systematically studied the charge redistribution in systems with low-coordinated sites. The analyses performed in the case of pure surfaces allows to conclude that within a tolerance region of c.a. 0.1 eV the charge transfer between the bulk and the surface sites is negligible. We have also verified that the relaxation of the distance between the surface layer and the bulk does not affect the charges attributed to the atoms. The analysis of the results obtained for pure clusters shows that except for the lowest-coordinated sites located on the vertices the charge redistribution is also negligible, however, even in these most extreme cases the total charge decreases only by less than 3% of the pure bulk value. It is worth pointing out, that in case of the most important d-orbital charge these modifications are much smaller. The results obtained in this chapter allowed to get more insight into the effect of site coordination on the electronic structure separately from the alloying effects and to conclude, that in terms of pure metals the local neutrality rule is generally obeyed.

CHAPTER 3

DFT calculations of mixed systems

The analysis performed in the previous chapter was focused on site coordination effects in pure systems. In the aim to further study nanoalloys the obvious extension is to investigate mixed systems and introduce complex alloying effects related to the modified local chemical environment. In the first part bulk CoPt systems of varying concentration and chemical ordering will be studied. Since the main objective is to derive general rules of electronic structure modifications and charge redistribution in such cases the study will be focused on a few most typical and useful configurations. Calculations on stoichiometrical $L1_0$ and $L1_2$ ordered alloys and a set of diluted systems were performed. In addition some disordered systems were considered. This will allow to study the mixing effects independently from coordination effects which will be introduced in the second part of this chapter where results of calculations in the case of mixed systems with spatially reduced dimensions will be presented. The calculations were performed for surfaces and thin films: Co monolayer on Pt(111) surface and CoPt slabs with different degrees of order, ranging from disordered to perfectly ordered $L1_0$. In the third part finite-size mixed systems will be investigated - nearly stoichiometrical clusters of sizes up to 561 atoms: $L1_0$ ordered cuboctahedra and icosahedra with alternating Co/Pt shells [61]. This variety of systems allowed an extensive analysis of the interplay between alloying and coordination effects and accounting for modifications of electronic structure and charge redistribution.

More precisely, the outline of this chapter is then the following: In the first section mixed bulk systems will be investigated. We will cover first the basic properties like lattice constants, bulk moduli and magnetic moments and compare them with available experimental data. We will then detail on the role of the magnetism on phase stability in CoPt alloys including diluted systems. The next step will be the in-depth analysis of charge distribution calculated with different methods and the notion of mixing rank will be introduced. We will then consider the charge redistribution and local magnetic moments on sites with different mixing rank and for various concentrations. Finally calculated local densities of state will be discussed. In the next section mixed systems with surfaces will be investigated using the example of one Co overlayer on a Pt(111) substrate. First the adsorption energies for different stacking variants will be analyzed and compared with experimental observations. We will then analyze again the charge redistribution and local magnetic properties, this time in the presence of surface. In the end the densities of state will be compared with those obtained for pure systems. The chapter will be supplemented by the similar analysis of the charge and spin magnetic moments in case of small clusters.

3.1 Mixed Co-Pt bulk systems

Three ordered phases of bulk Co-Pt alloy have been studied (Fig. 3.1): Co_3Pt ($L1_2$), CoPt ($L1_0$) and $CoPt_3$ ($L1_2$). In order to allow for systematic analysis of broader range of concentrations diluted A(B)[1] systems had to be considered as well. The calculations were performed for large supercells (32 - 256 atoms) of pure element with one atom of impurity which due to the application of periodic boundary conditions resulted in different effective impurity concentrations ranging from 0.4% to 3.1% (Fig. 3.2). Because of the computational limitations for the size of the supercell the effective concentration of impurities is relatively high with regards to an ideal diluted system and the impurity atoms are periodically distributed in the infinite bulk system modeled in this way. Because of the possible interaction between impurity atoms and possible geometrical artifacts of periodicity, especially in case of the non-cubic supercells with artificial anisotropy of impurity distribution the most reliable results are expected for the largest, cubic supercells. Relaxation of the positions of atoms were in the taken into account, however, the improvements of the total energy, changes of the local electronic structure and in the charge redistribution were negligible.

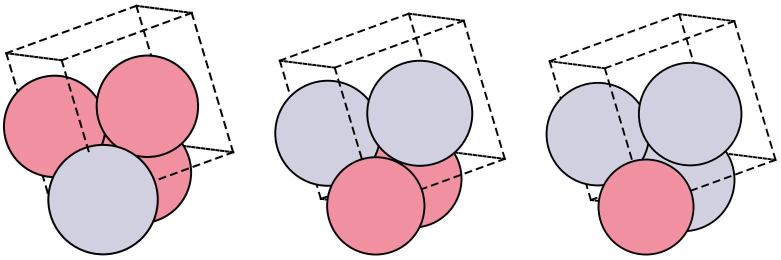

$L1_2$ Co_3Pt $L1_0$ CoPt $L1_2$ $CoPt_3$

Figure 3.1: Unit cells of ordered Co-Pt alloys studied in the present work.

3.1.1 Basic properties

Similarly to previous chapter also in the case of CoPt mixed systems a number of properties were calculated and subsequently compared with the available experimental data. All calculations were performed both in paramagnetic and ferromagnetic cases. In the case of $L1_0$ CoPt the tetragonal distortion of structure was taken into account.

The main results are summarized in the Tabs. 3.1, 3.2 and 3.3.

Comparison with the experimental values in case of $L1_0$ CoPt shows an overall good agreement in terms of lattice constants, bulk modulus and magnetic moments although the local magnetic moment on Co sites in the $L1_0$ ordered phase is rather overestimated. However the evolution of the total magnetic moment is consistent to what is expected in the CoPt systems. Since in this compound cobalt is the magnetic element one finds

---

[1] where A(B) denotes pure A crystal with B impurity atoms for A,B ∈ {Co,Pt}

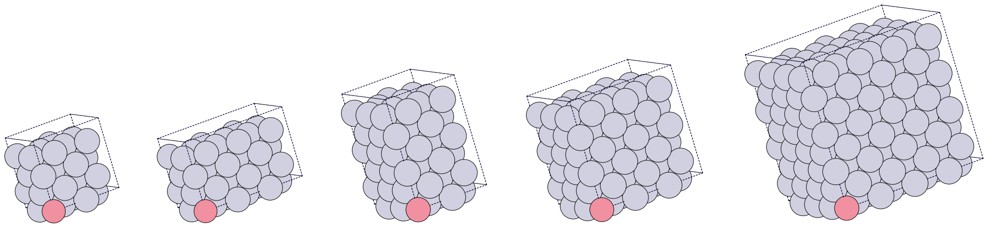

N	32	48	72	108	256
C	3.1%	2.1%	1.4%	0.9%	0.4%
V	0.50 nm^3	0.76 nm^3	1.13 nm^3	1.70 nm^3	4.04 nm^3
	$2 \times 2 \times 2$	$2 \times 2 \times 3$	$2 \times 3 \times 3$	$3 \times 3 \times 3$	$4 \times 4 \times 4$

Figure 3.2: Supercell geometries used for calculations of diluted systems. N denotes the total number of atoms in the supercell of volume V and C is the concentration of impurities. Supercell dimensions along x, y and z-axis are given in unit cells (4 atoms).

CoPt (L1$_0$)	paramagnetic	ferromagnetic	experimental
lattice constant a [Å]	3.823 (3.749)	3.821 (3.784)	3.81 [8, 128]
lattice constant c [Å]	3.641	3.703	3.69 [8, 128]
distortion (c/a ratio)	0.952	0.969	0.955 [8, 128]
bulk modulus [GPa]	250.5	229.4	229 [129]
total magnetic moment [μ_B/atom]	–	1.155	1.11 [130] 1.20 [128]
local mag. mom. Co/Pt [μ_B/atom]	–/–	1.965/0.255	1.76/0.35 [131]

Table 3.1: Comparison of calculated properties of L1$_0$ CoPt and those measured experimentally. Lattice constants a enclosed in parentheses have been calculated in case of no tetragonal distortion (with assumption that $c/a = 1$).

Co$_3$Pt (L1$_2$)	paramagnetic	ferromagnetic	experimental
lattice constant [Å]	3.612	3.661	3.67 [128]
bulk modulus [GPa]	299.0	259.6	
total magnetic moment [μ_B/atom]	–	1.405	1.46 [128]

Table 3.2: Comparison of calculated properties of L1$_2$ Co$_3$Pt and experimental data.

CoPt$_3$ (L1$_2$)	paramagnetic	ferromagnetic	experimental
lattice constant [Å]	3.870	3.890	3.87 [128]
bulk modulus [GPa]	268.4	254.4	
total magnetic moment [μ_B/atom]	–	0.742	0.67 [128]

Table 3.3: Comparison of calculated properties of L1$_2$ CoPt$_3$ and experimental data.

indeed that total magnetic moment is increasing with cobalt concentration. Conversely the local magnetic moment on Co site is increased with regard to bulk elemental Co when it is surrounded by Pt atoms upon alloying. At the same time Pt is acquiring a small local magnetic moment upon alloying (see Tab. 3.1 for $L1_0$ phase).

3.1.2 Magnetism and phase stability in CoPt alloys

Observations from the previous section raise the fundamental issue of the importance of magnetism in the evaluation of phase stability in ordered CoPt alloys. To answer this question first a simple total energy analysis has been performed. From Fig. 3.3 it is clear that introduction of spin polarized calculations leads to lower total energies of the system which insures preference for ferromagnetic configuration in these systems. One can also notice that for all systems in case of ferromagnetic calculations total energy minima correspond to the larger energetically preferred unit cell volumes (and subsequently lattice constants) compared to the paramagnetic case which is related to the existence of additional ferromagnetic interactions that, due to their repulsive nature, lead to increase of the interatomic distances.

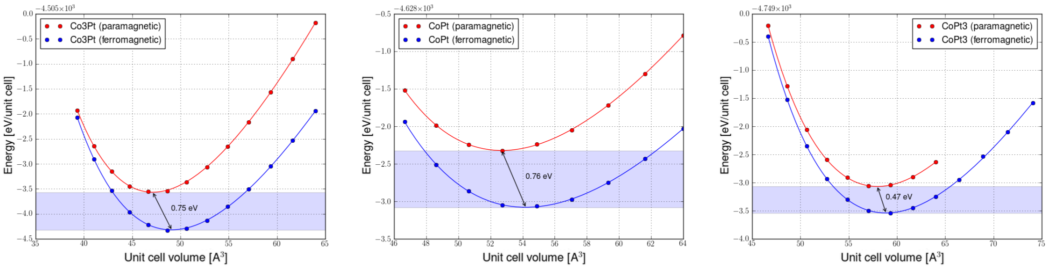

Figure 3.3: Comparison of total energies as a function of unit cell volume for: $L1_2$ Co_3Pt (left), $L1_0$ CoPt (center) and $L1_2$ Co_3Pt (right). Differences between minima corresponding to paramagnetic (red) and ferromagnetic (blue) calculations are marked.

In order to assess the ordering tendency and its relation with magnetism, systematic analysis of heat of formation with respect to cobalt concentration have been performed. Heats of formation were determined using the following formula:

$$\Delta H = E(\mathrm{Co}_x\mathrm{Pt}_{1-x}) - x \cdot E(\mathrm{Co}) - (1-x) \cdot E(\mathrm{Pt}) \tag{3.1}$$

where x denotes concentration and E(system) total energy of the system per atom. This is simply the difference between total energy of a system and sum of the energies of its constituents calculated separately. Using formula presented above heats of formation of mixed systems were calculated in both spin-polarized and non spin-polarized variants. There is, however, some ambiguity in the choice of reference states for pure metals, namely, the crystalline structure (if there is more than one possibility) and spin-polarization variant. Regarding the first problem fcc structure for pure Co and Pt metals has been used. Second problem is more intricate - one approach, adopted in the work of Karoui *et al* [30], is to choose, the same spin-polarization variant both for alloy and pure bulk calculations so that elemental non magnetic Co is used as reference for non magnetic alloy and elemental ferromagnetic Co for ferromagnetic. Another approach, utilized in the present work, is to use always the same reference system, spin-polarized for magnetic metals and non spin-polarized otherwise i.e. ferromagnetic Co and non magnetic elemental Pt. The latter method has the advantage of common reference levels for all calculations which simplifies interpretation of results and it is also supposed to better capture the spirit of the definition of heat of formation - it compares the energy of the formed alloy (in given magnetic variant) to the energies of its free constituents the latter being taken here in a single ground state (magnetic for Co and non magnetic for Pt).

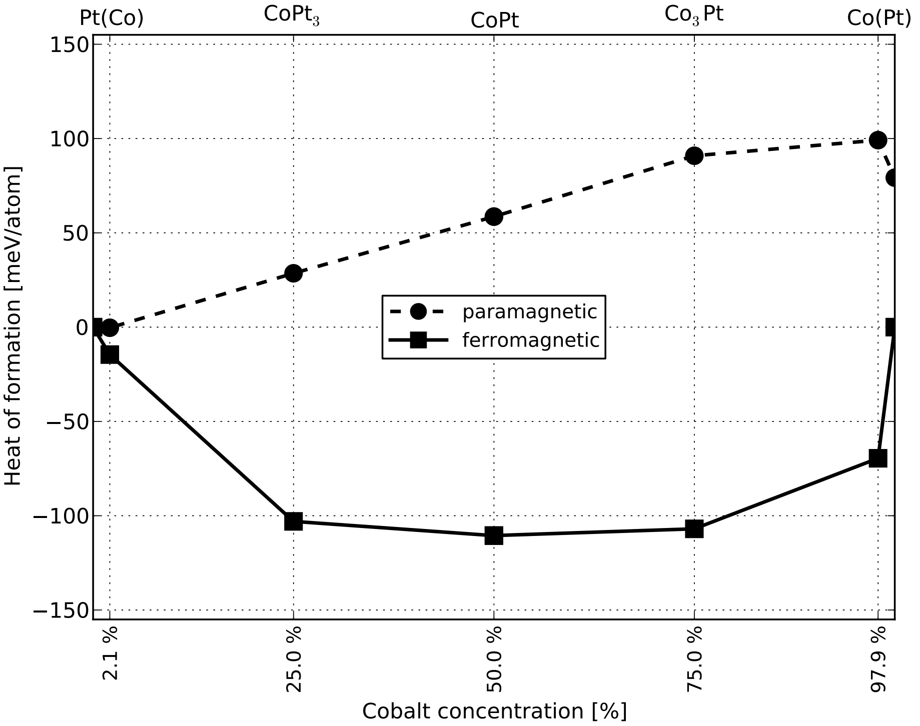

Figure 3.4: Heats of formation of Co-Pt systems with respect to cobalt concentration.

The results are reported in Fig. 3.4 from which it is straightforward to deduce that ferromagnetic phases are stabilized by the presence of magnetic effects ($\Delta H < 0$) while paramagnetic configurations have tendency for phase separation which is indicated by $\Delta H > 0$. This observation is consistent with results available in the literature [30]. However, while in the present work we observed phase separation tendency in non-magnetic systems, the authors of [30] report on relative ordered phase stabilities, more precisely, on very weak (yet negative) ΔH of non-magnetic systems when compared to magnetic calculations. The difference between both studies of non magnetic alloys is probably related to the different choice of reference for elemental Co, magnetic in our case, non magnetic in [30]. This points out that the results for non-magnetic systems strongly depend on the choice of the reference. Both calculations predict successfully that ferromagnetic $L1_0$ is the most stable phase and agree on the value of its heat of formation (-0.10 eV/at in [30] and -0.11 ev/at in the present work) with other *ab-initio* calculations [132, 133] and experimental value of −0.13 eV/at [134].

Contrary to ordered $L1_0$ and $L1_2$ Co-Pt alloys the question of diluted systems is not discussed elsewhere. Supercell scheme used in DFT calculations makes this problem more complicated due to the possible errors coming from relatively small supercell size and related to periodic boundary condition that all together yields high effective concentration of impurities and raises questions regarding the impact of the interactions between them. However one can see in Fig. 3.4 that the formation energies of diluted systems follow the same behavior with regard to magnetism, the effect is particularly well marked in strongly magnetic, almost pure cobalt systems.

The overall conclusion of this study is that, consistently with the results of [30], magnetism strongly reinforces order tendency in CoPt alloys.

3.1.3 Charge redistribution in modified chemical environment

Let us recall here that one important point in this work is to establish a reliable rule of charge distribution on sites and orbitals in CoPt alloys that could be implemented in a relevant tight-binding self-consistent procedure for CoPt alloys and then nanoalloys. In the case of a previous study of CoAu systems it was indeed shown that a strict local neutrality rule per species, sites and orbitals was followed whatever the concentration of the considered system [33]. Here we have to verify if this rule can be extended to CoPt systems and if yes on which range of concentration/composition in the alloy.

Mulliken analysis of charge on atoms in CoPt various bulk systems

We will consider here all the systems studied in the first part of this chapter namely ordered phases and diluted systems. For sake of simplicity all the systems were taken in the fcc crystalline structure where all sites in the infinite bulk have 12 nearest neighbors[2] The only difference comes from the varying chemical environment since in case of binary alloy the sites in the neighborhood of a given site can be occupied either by the atom of the same or opposite type. The number of nearest-neighbor sites occupied by a different atom than the one occupying given site i, that we will call here mixing rank M_i, will depend on particular chemical configuration as shown in the following table:

---

[2] This choice has been motivated by the fact that properties relevant to this work are only slightly affected by the tetragonal distortion, namely: changes of Mulliken populations are below the accuracy of the method (less than 0.01 e), magnetic moment differences are negligible and total energy of structure with tetragonal distortion is lower by less than 20 meV/atom, which is consistent with observations made by other authors i.e. [30].

M_i(Co)		paramagnetic				ferromagnetic			
		s [e]	p [e]	d [e]	$\sum$ [e]	s [e]	p [e]	d [e]	$\sum$ [e]
Co	0	0.59	1.07	7.34	9.00	0.59 $0.28\uparrow 0.31\downarrow$	1.09 $0.50\uparrow 0.59\downarrow$	7.32 $4.52\uparrow 2.80\downarrow$	9.00 $5.30\uparrow 3.70\downarrow$
Co(Pt)	1	0.62	1.08	7.35	9.05	0.60 $0.29\uparrow 0.31\downarrow$	1.12 $0.53\uparrow 0.60\downarrow$	7.32 $4.50\uparrow 2.82\downarrow$	9.05 $5.32\uparrow 3.73\downarrow$
Co_3Pt	4	0.58	1.24	7.32	9.14	0.59 $0.29\uparrow 0.30\downarrow$	1.26 $0.60\uparrow 0.66\downarrow$	7.27 $4.56\uparrow 2.71\downarrow$	9.12 $5.45\uparrow 3.68\downarrow$
CoPt	8	0.55	1.34	7.30	9.18	0.55 $0.28\uparrow 0.28\downarrow$	1.38 $0.68\uparrow 0.70\downarrow$	7.23 $4.62\uparrow 2.62\downarrow$	9.17 $5.57\uparrow 3.59\downarrow$
$CoPt_3$	12	0.49	1.36	7.27	9.12	0.51 $0.26\uparrow 0.25\downarrow$	1.41 $0.73\uparrow 0.68\downarrow$	7.20 $4.66\uparrow 2.54\downarrow$	9.12 $5.65\uparrow 3.47\downarrow$
Pt(Co)	12	0.50	1.34	7.27	9.11	0.52 $0.27\uparrow 0.25\downarrow$	1.43 $0.74\uparrow 0.69\downarrow$	7.17 $4.72\uparrow 2.45\downarrow$	9.12 $5.73\uparrow 3.39\downarrow$

Table 3.4: Charge distribution between orbitals on **cobalt** bulk sites.

configuration	$M_i(A)$	A concentration	location
A	0	100%	atom inside pure bulk
A(B)	1	$> 75\%$	atom next to the impurity
A3B	4	75%	$L1_2$ dominant component
AB	8	50%	any atom in stoichiometric $L1_0$
AB3	12	25%	$L1_2$ minority component
B(A)	12	$< 25\%$	impurity atom

This classification allows for systematic analysis of the local chemical environment modifications on charge redistribution. The results of the usual Mulliken analysis are summarized in Tabs. 3.4 and 3.5. In each system two neighboring sites occupied by different atoms have been chosen for analysis (in $L1_0$ and $L1_2$ structures this choice is unambiguous because of site equivalence stemming from the unit cell symmetries, in case of impurities one of the selected sites is always impurity and the other is one of its nearest-neighbors). This choice of sites will be used later as well.

In case of cobalt one can immediately notice that despite of dramatic change of the chemical environment the total site charge changes only by 0.14 e in the worst case, internal charge transfer between orbitals is also negligible and comparable to the accuracy of the method. Since local magnetic moment varies with concentration, there is, however charge transfer between spin orientations ~ 0.45 e.

The case of platinum is more complicated: as mixing rank grows the platinum site is slowly deprived of over 1 e of electronic charge, however, it is worth noticing that the charge that is transferred to the surrounding cobalt sites comes mostly from p orbital. There are as well, in rare cases (for platinum impurity only), some negative values which is one of the possible artifacts of Mulliken analysis (see e.g. [135] for discussion).

M_i(Pt)		paramagnetic				ferromagnetic			
		s [e]	p [e]	d [e]	$\sum$ [e]	s [e]	p [e]	d [e]	$\sum$ [e]
Pt	0	0.65	0.97	8.38	10.00	0.65 $0.32\uparrow 0.32\downarrow$	0.97 $0.48\uparrow 0.48\downarrow$	8.38 $4.19\uparrow 4.19\downarrow$	10.00 $5.00\uparrow 5.00\downarrow$
Pt(Co)	1	0.65	0.94	8.39	9.99	0.65 $0.33\uparrow 0.33\downarrow$	0.94 $0.47\uparrow 0.47\downarrow$	8.40 $4.25\uparrow 4.15\downarrow$	9.99 $5.04\uparrow 4.95\downarrow$
$CoPt_3$	4	0.70	0.85	8.40	9.96	0.70 $0.35\uparrow 0.35\downarrow$	0.84 $0.39\uparrow 0.45\downarrow$	8.42 $4.38\uparrow 4.04\downarrow$	9.96 $5.12\uparrow 4.85\downarrow$
CoPt	8	0.74	0.66	8.42	9.81	0.73 $0.36\uparrow 0.38\downarrow$	0.64 $0.27\uparrow 0.37\downarrow$	8.46 $4.42\uparrow 4.04\downarrow$	9.83 $5.04\uparrow 4.79\downarrow$
Co_3Pt	12	0.75	0.39	8.43	9.57	0.74 $0.35\uparrow 0.39\downarrow$	0.39 $0.14\uparrow 0.25\downarrow$	8.50 $4.42\uparrow 4.07\downarrow$	9.63 $4.92\uparrow 4.71\downarrow$
Co(Pt)	12	0.73	-0.27	8.46	8.92	0.72 $0.35\uparrow 0.37\downarrow$	-0.20 $-0.14\uparrow -0.06\downarrow$	8.51 $4.42\uparrow 4.09\downarrow$	9.03 $4.63\uparrow 4.40\downarrow$

Table 3.5: Charge distribution between orbitals on **platinum** bulk sites.

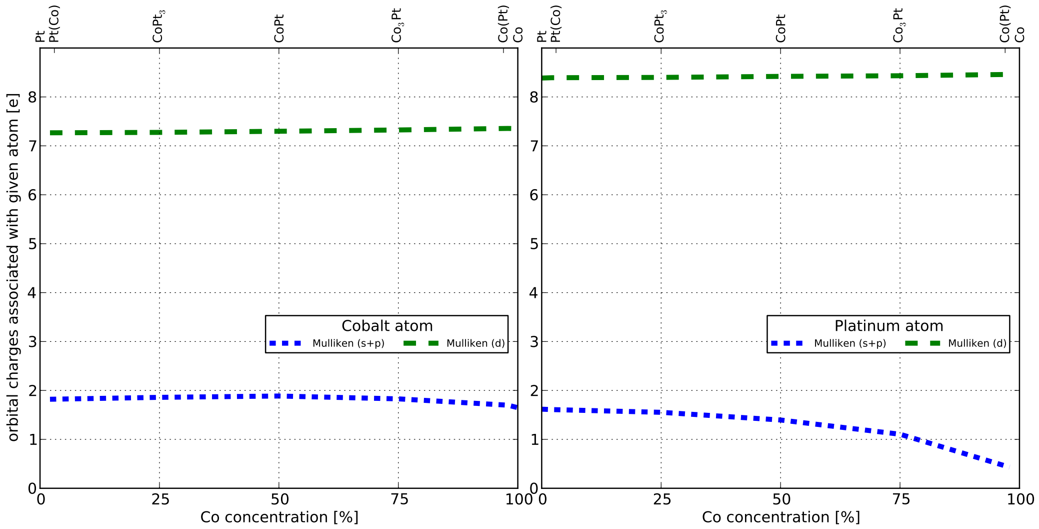

Figure 3.5: Comparison of s+p (blue) and d (green) orbital charges calculated with Mulliken method on cobalt (left) and platinum sites (right) for paramagnetic systems of different cobalt concentration (and, therefore, site mixing rank).

Comparison of methods for charge distribution: Mulliken *vs* Bader analysis

The results are summarized in Fig. 3.7 and Tab. 3.6. The total Mulliken charge exhibits similar trend as the charge calculated with Voronoi charge density partitioning. Bader and Voronoi variants agree for pure systems since of homogeneity and symmetry in this case makes Bader volumes equal to Voronoi. Because the effective "sizes" of Co and Pt atoms are different in mixed systems Voronoi analysis overestimates Co site charge and underestimates Pt site charge. One can observe, however, that regardless of the method the charge redistribution induced by mixing rank changes does not exceed 0.5 e except for diluted Pt system where it is almost 1.0 e and cannot be neglected.

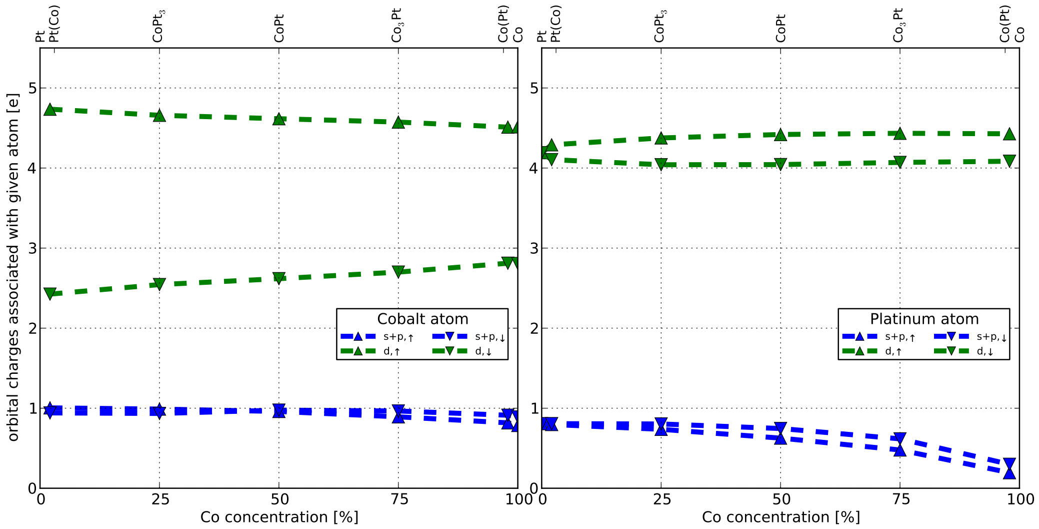

Figure 3.6: Comparison of s+p (blue) and d (green) orbital charges calculated with Mulliken method on cobalt (left) and platinum sites (right) for ferromagnetic systems of different cobalt concentration (and, therefore, site mixing rank).

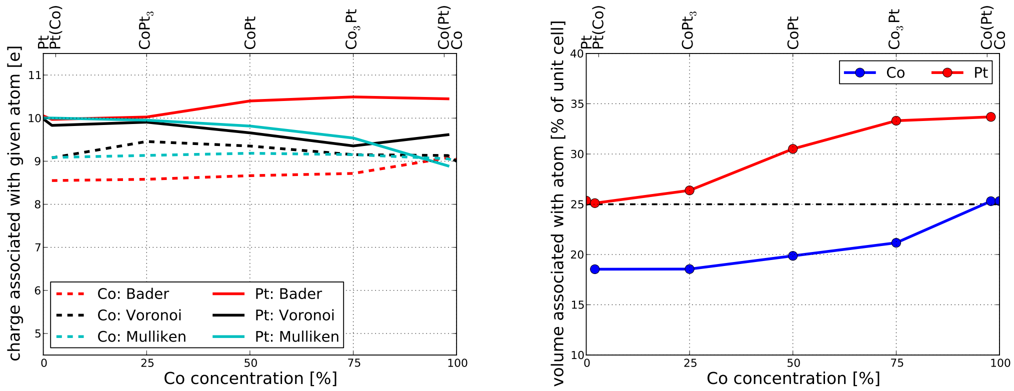

Figure 3.7: Comparison of charges on cobalt (dashed) and platinum (solid) sites calculated with Mulliken method (cyan) and from charge density with Bader (red) and Voronoi (black) approach for paramagnetic systems of different Co concentration (left). Bader volume associated with each site type as unit cell fraction with respect to cobalt concentration is also shown (right).

Insight into charge distribution in systems with different degree of ordering

In realistic experimental systems, like nanoalloys, the composition may be rather inhomogeneous with regard to bulk ordered phases. In order to get a qualitative idea on how could vary the charge distribution in more inhomogeneous systems we have simulated some disordered bulk systems and performed systematic analysis of the charge redistribution induced by changes of the mixing rank of the site which can be compared to the coordination effects. $L1_0$ structure consists of two equipotent sublattices of respective

Cobalt site

	Mulliken [e]	Bader [e]	Voronoi [e]
Co	9.00	9.04	9.00
Co(Pt)	9.05	9.08	9.13
Co_3Pt	9.15	8.72	9.15
CoPt	9.18	8.66	9.35
$CoPt_3$	9.13	8.58	9.46
Pt(Co)	9.09	8.55	9.08

Platinum site

	Mulliken [e]	Bader [e]	Voronoi [e]
Co(Pt)	8.89	10.45	9.62
Co_3Pt	9.54	10.49	9.36
CoPt	9.82	10.40	9.66
$CoPt_3$	9.95	10.03	9.91
Pt(Co)	10.00	9.97	9.83
Pt	10.00	10.05	9.98

Table 3.6: Comparison of site charges calculated with different methods.

atom types. The long range order parameter η can be defined as $\eta = 2 \cdot n_a/N_a - 1$ where N_a denotes number of sites of a-atom sublattice and $0 < n_a \leq N_a$ is a number of a atoms on a-atom sublattice. Therefore, $\eta = 1$ corresponds to perfectly ordered $L1_0$ phase and $\eta = 0$ to completely disordered systems. The typical size of the used cells is 4 × 4 × 4 which is reasonable to be handled with DFT calculations.

The results for charge distribution are shown on the left plot in Fig. 3.8. One can immediately notice, that the d-orbital charge is not affected by the mixing at all. In case of total charge there is a slight trend for Pt sites to acquire charge with increased mixing rank. For cobalt sites this tendency is reversed. However, even between the extreme cases ($M_i = 0$ and $M_i = 12$) the difference of the charges does not exceed 0.3 e with one, already discussed, exception of platinum site of $M_i = 12$ where the total charge is 1 e lower than on pure bulk sites. It is also worth pointing out, that for equivalent sites (occupied by the same atom and with exactly the same mixing rank) the differences of the charge are negligible, especially for the most important d-orbital charges.

3.1.4 Evolution of local magnetic properties as a function of chemical environment

The charge distribution allows also following the evolution of local spin magnetic moment in terms of chemical environment. We have therefore studied the evolution of

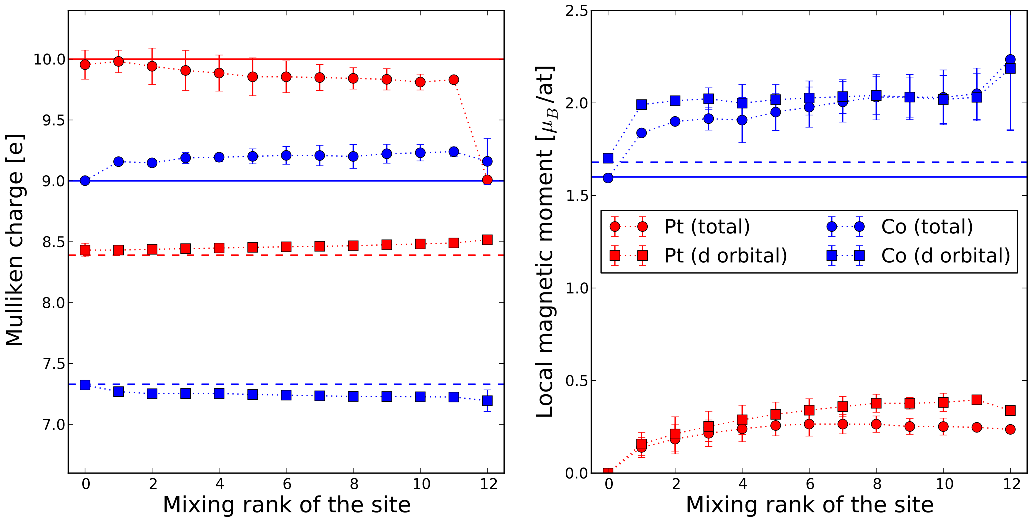

Figure 3.8: Comparison of the Mulliken total (circles) and d-orbital (squares) charges (left plot) and local magnetic moments (right plot) with respect to the site mixing rank for platinum (red) and cobalt (blue) sites. This is the average calculated over all bulk sites of all samples within CoPt slabs of different order parameter ranging from 0 to 1. Respective pure bulk values are marked with horizontal lines (dashed for d-orbital).

local spin magnetic moment with cobalt concentration from the Mulliken distributions by making the difference between local spin up and spin down charges at Co and Pt atomic sites in the different configurations, first in the set of ordered phases and diluted systems. Results for magnetic moment per site (Co and Pt) and per orbital contributions (d and s+p) are presented in Fig. 3.9. Polarization of platinum atoms in contact with Co atoms in the alloy increases with cobalt concentration until a relatively small critical concentration is reached and then is stabilized on the level of 0.26 μ_B/atom. At the same time local magnetic moments associated with particular cobalt atoms decrease but since their concentration grows the total magnetic moment increases with Co concentration which is consistent with experimental evidence (see Tab. 3.1, Tab. 3.2 and Tab. 3.3). Comparing the calculated magnetic moments to the one of pure cobalt one can deduce, that one alloying effect is to decrease total magnetic moment which is purely a concentration effect since the number of the most polarized atoms decreases when their concentration decreases. At the same time, on a local point of view, the alloying effect is to increase the local magnetic moment on cobalt sites while cobalt atoms are surrounded by more and more platinum atoms approaching in this way the configuration of the isolated Co which is the configuration of maximal magnetic moment. The combined s and p orbital contribution is order of magnitude smaller than d orbital contribution. In case of cobalt sites it slightly decreases the overall magnetic moment for systems with cobalt concentrations above 50% and increases it for platinum-rich systems. In case of platinum sites s+p contribution to the local magnetic moment is always negative and therefore decreases the overall local magnetic moment on these sites. This effect is most pronounced for high Co concentrations. Of course these latter considerations must be taken with much caution since we may have uncertainties in Mulliken analysis. Nevertheless the overall rationale on local magnetic properties does not change much while considering or not sp contribution since the predominant contribution to magnetism is coming from d electrons. These considerations can be extended to disordered systems while using the analysis in terms of mixing rank. The results are shown on the right plot in Fig. 3.8. They include CoPt slabs of different degrees of ordering going from completely disordered systems to perfectly ordered one. The results are also consistent with the experimental evidence (see e.g. [136] for the review). Finally, it is worth noting, that local magnetic moment of cobalt grows abruptly in mixed environment (starting from $M_i = 1$) and is almost constant until further increase at $M_i = 12$.

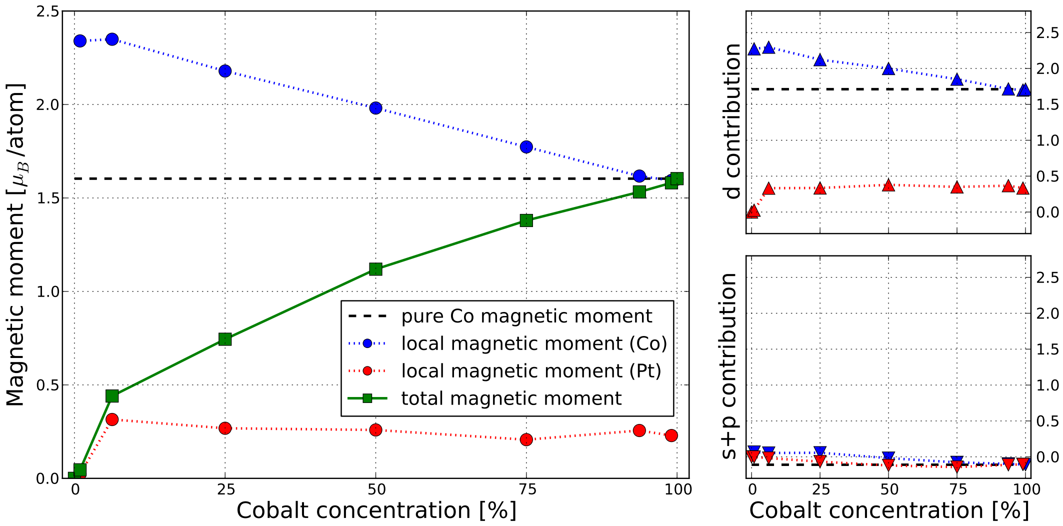

Figure 3.9: Average magnetic moments of Pt atoms (red), Co atoms (blue) and total magnetic moment (green) in mixed systems with respect to cobalt concentration (left). Two smaller plots on the right show d (upper) and s+p (lower) contributions.

The case of dilute systems is quite peculiar since contrary to pure FCC metals and $L1_0$ or $L1_2$ alloys the symmetry of atomic sites is broken by the presence of single impurity atom in the supercell. The analyses performed so far were concentrated on impurity atoms and their neighbor sites. This naturally leads to a question about spin on sites further away from impurity. This effect has been studied here and results are shown in Fig. 3.10 where it can be seen that the values of local magnetic moment converge rapidly to the corresponding pure bulk values as the distance from the impurity increases.

3.1.5 Evolution of densities of states with chemical environment

Calculations of mixed bulk systems performed for a wide range of element concentrations gave opportunity to study the modifications of the local density of states on a given site with respect to its local chemical environment. Local densities of state

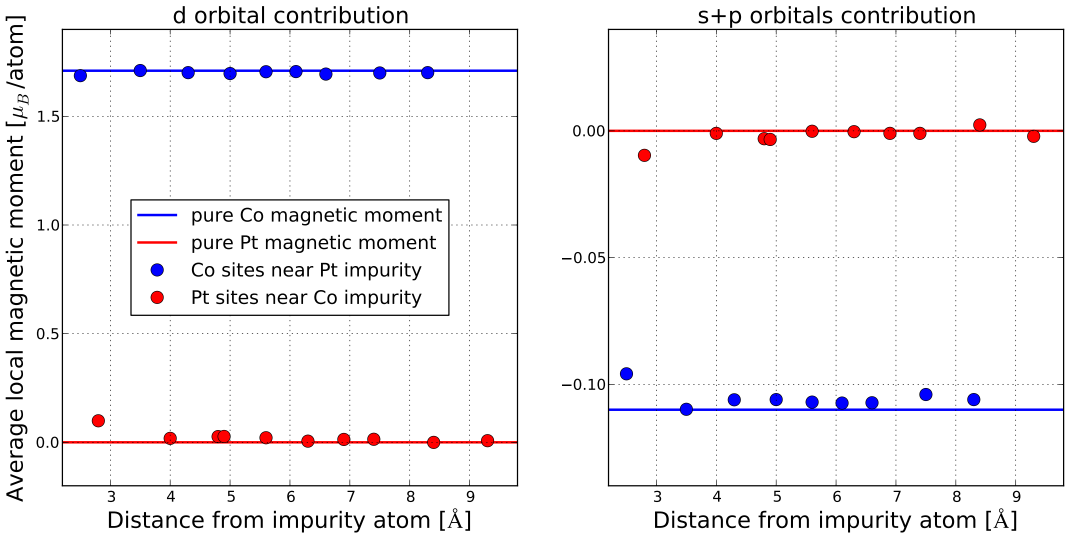

Figure 3.10: Average magnetic moment on Pt (red) and Co (blue) atoms in the dilute system system with, respectively, one Co or Pt impurity atom - d orbital (left) and s+p orbitals contributions (right). Solid lines correspond to the values for pure bulk.

projected on d orbital are presented in Fig. 3.11 (paramagnetic case) and Fig. 3.12 (ferromagnetic case). The reason for choosing only d band is that for transition metals d-electrons have the greatest impact on the catalytic (bond formation, oxidation states) and magnetic (spin polarization) properties, d-orbital predominantly contributes to the total LDOS and therefore also to the energetics. Several observations can be made. First of all the density of states of minority component, that is, on a site with high mixing rank, narrows as the mixing rank grows and the band width reaches its minimum in case of dilute systems (i.e. impurity atom). In paramagnetic case this results in elevated density of states within small energy range. Interestingly, in case of cobalt the peak of density emerges right below Fermi energy contrary to platinum where additional electronic states concentrate on lower energies. According to Stoner criterion [137] one can therefore expect higher magnetization on Co sites that will grow with their mixing rank (decreasing Co concentration) which is indeed the case (Fig. 3.9). Obviously the density of states of majority component converges with its concentration towards the reference of pure bulk density. One can also note that the LDOS is sensitive mostly to the local modifications of chemical environment (mixing rank): the density of states on impurity atom does not change with impurity concentration (which means, that the impurity atoms do not affect each other within the scheme of limited cell sizes where the impurity could interact with its image through periodic boundary conditions, see Fig. 3.13) and density of states on the nearest-neighbors of the impurity is very slightly modified compared to the pure element (Fig. 3.11, last row).

At sufficiently high Co concentration (starting from 25% in case of $CoPt_3$) it can be observed that CoPt alloys are strong ferromagnets with a full majority spin band (spin up). It can be seen that upon alloying effect, when Pt atoms are surrounded by Co atoms, they become polarized. Pt d-band spin up and spin down are modified and shifted one from each other. The hybridization between Co and Pt d states is clearly visible at around 1 eV above Fermi level where Pt spin down LDOS shows a well marked small peak while density of spin up is zero. This hybridization leads to a small induced local magnetism on Pt as it was already observed in the framework of Mulliken analyses.

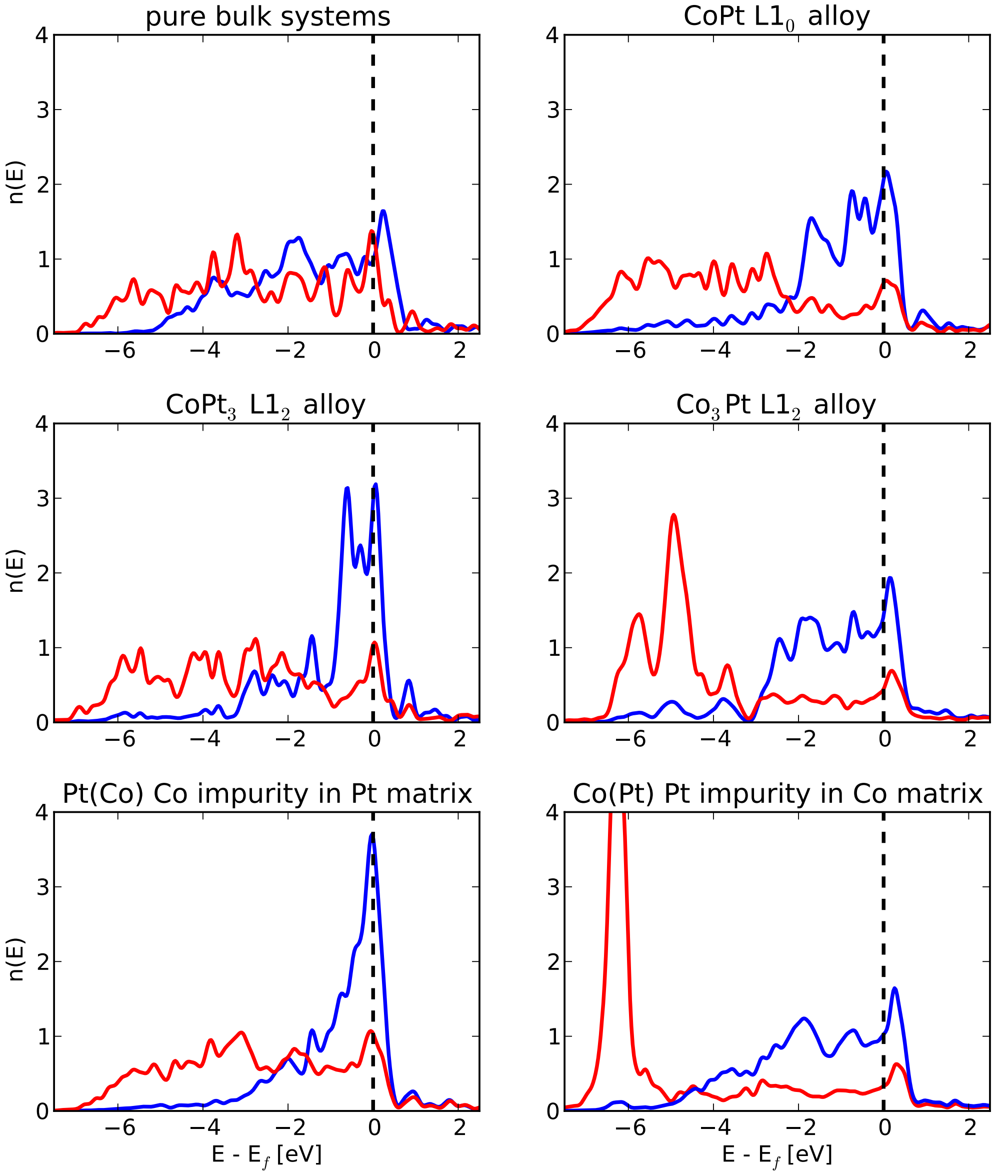

Figure 3.11: Local density of states (d band, paramagnetic case) of neighboring cobalt (blue) and platinum (red) sites. For comparison the corresponding pure element bulk LDOS are shown on the upper left plot.

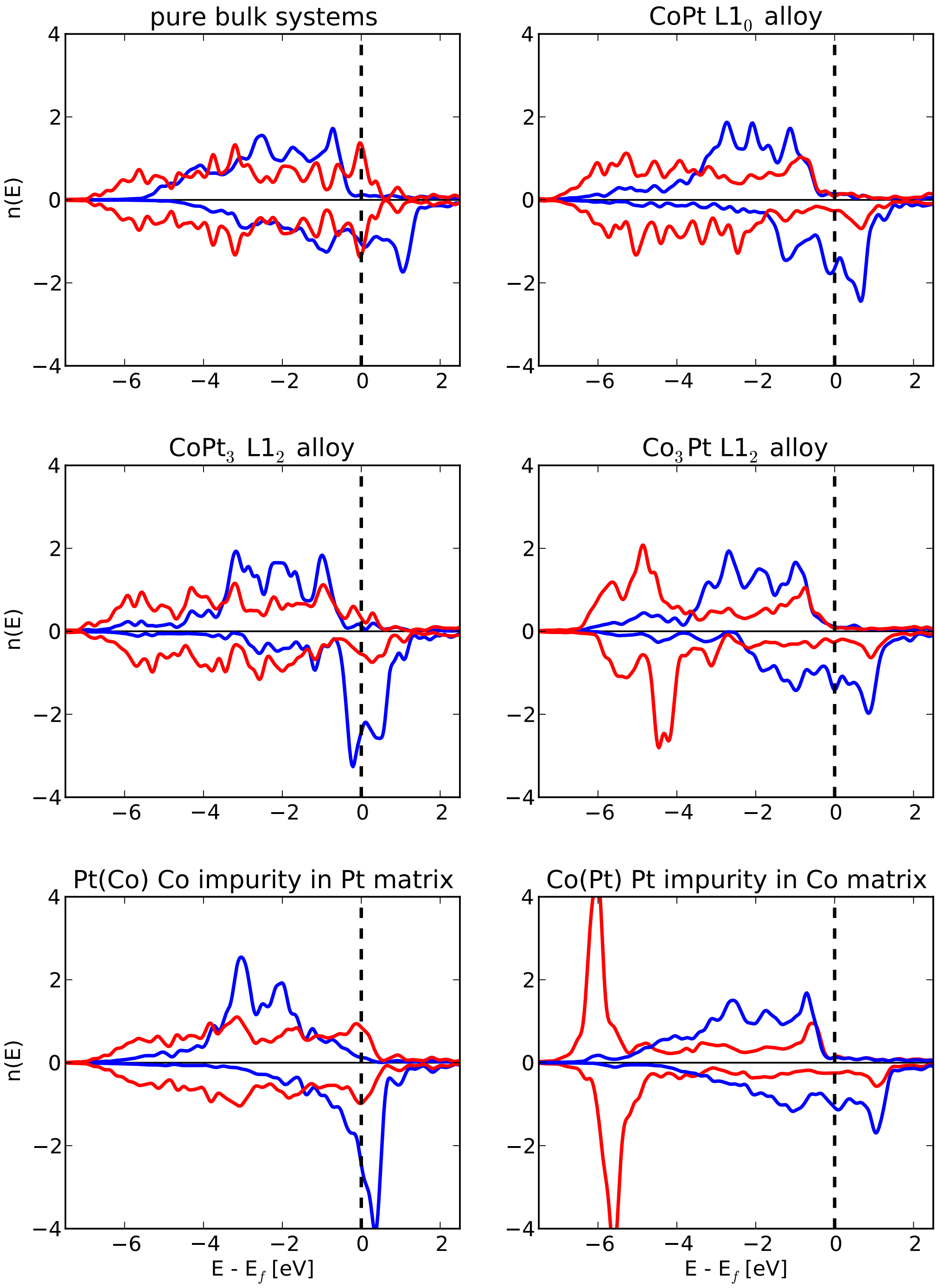

Figure 3.12: Local density of states (d band, ferromagnetic case) of neighboring cobalt (blue) and platinum (red) sites. For comparison the corresponding pure element bulk LDOS are shown on the upper left plot.

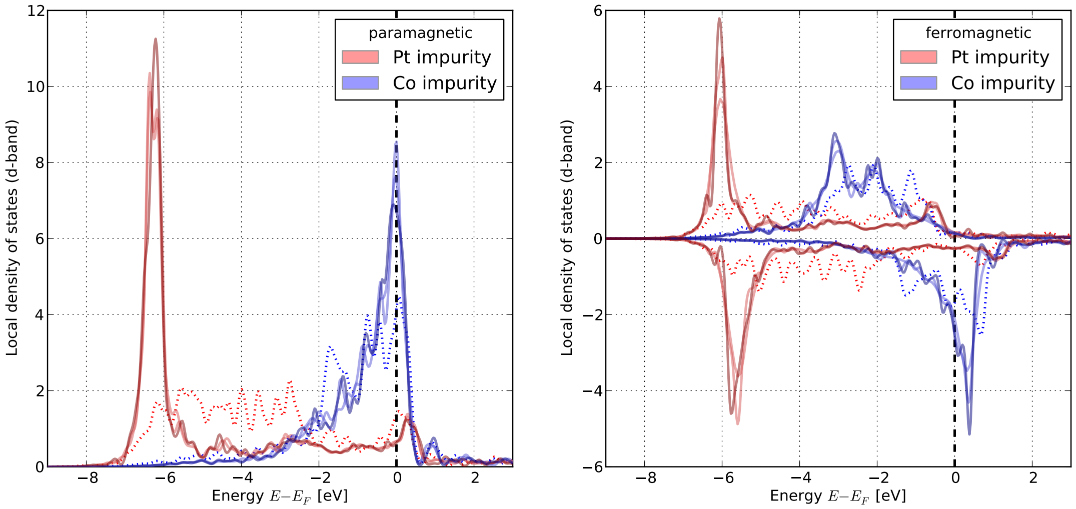

Figure 3.13: Electronic structure in diluted systems ($M_i = 12$). Local density of states (d band) on the impurity atom for various supercell sizes denoted by color intensity (47+1, 71+1 and 107+1 atoms). $L1_0$ CoPt LDOS is shown for comparison (dots).

3.2 Surfaces and thin films: the case of one Co overlayer on a Pt(111) substrate

Natural extension of the analyses performed for bulk systems was to combine both mixing and surface effects. One practical case was selected: cobalt monolayer on top of Pt(111) slab (Fig. 3.14). This system has the additional interest to be representative of systems of ultra thin films or nanostructured surface systems widely investigated both experimentally [138, 139, 140, 11] and within atomistic simulations [141, 142].

The calculations for the Pt(111)+Co system were performed with varying Pt(111) slab thickness (between 5 and 25 atomic layers) and three stacking variants, namely fcc, hcp and on-top. The outermost atomic layer was relaxed in direction perpendicular to the surface. By this study we wanted also to check the energy difference between fcc and hcp stackings of the adlayer knowing *a priori* that they are the most favorable and are possibly competing but what we don't know is the quantitative difference between them and the effect of magnetism. It is in fact a general question in growth of compact metallic structures which stacking is preferentially followed. This question cannot not be solved in principle by semi-empirical descriptions, like the second moment approximation of the tight-binding formalism, which are unable to differentiate quantitatively fcc stacking from hcp stacking.

3.2.1 Energetics

Systems with overlayers can be characterized by adsorption energy defined as difference between total energy of such system and sum of the energies of pure adsorbent and

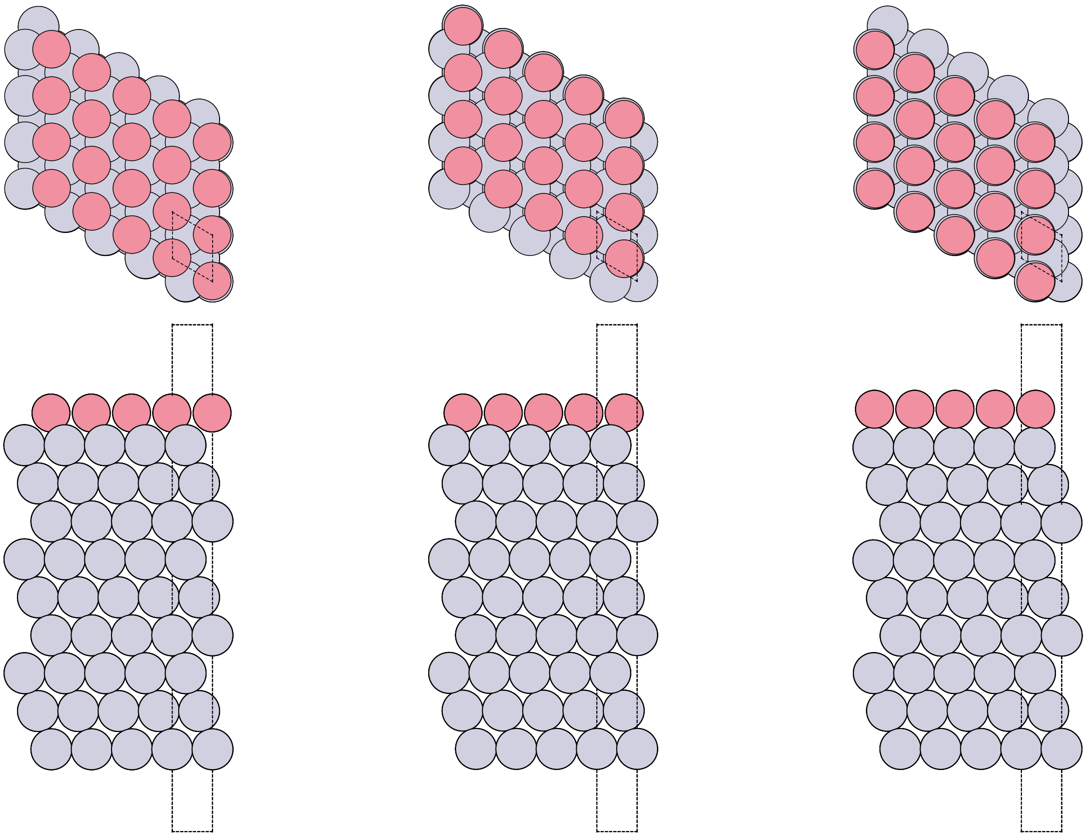

Figure 3.14: Co (purple) monolayer on top of Pt(111) surface with stacking variants: fcc (left), hcp (center) on-top (right). Fragment of (111) surface and slab cross-section.

free atoms adsorbate (vapor phase). E.g. in case of n Co atoms absorbed on a Pt(111) surface adsorption energy per one Co atom can be written in the following way:

$$E_{\text{ads}} = \left(E_{\text{tot}}[\text{Pt(111)+Co}] - E_{\text{tot}}[\text{Pt(111)}] - nE_{\text{free}}[\text{Co}]\right)/n \tag{3.2}$$

The adsorption energy E_{ads} of Co monolayer has been calculated for fcc, hcp and on-top stacking variants. Results obtained for different Pt(111) slab sizes are presented in Fig. 3.15 (left). On-top configuration (as well as bridge positions) is obviously much less favorable in metallic close-packed system. Nevertheless we considered this position in order to have a quantitative energy reference about the difference between most favorable and unfavorable adsorption sites. One can observe, that indeed $E_{\text{ads}}^{\text{fcc}} < E_{\text{ads}}^{\text{hcp}} \ll E_{\text{ads}}^{\text{on-top}}$ both for magnetic and non-magnetic calculations. The effect of magnetism is here only a rigid shift of the adsorption energies while the relative energies between the different stackings are unchanged. The energetical difference between fcc and hcp is, however, relatively small and therefore both variants should be observed experimentally with majority of fcc. As can be seen in the STM image in Fig. 3.15 (right) this is indeed the case and Pt(111) surface is covered mostly by fcc stacked Co with thin boundary regions where hcp stacking can be observed.

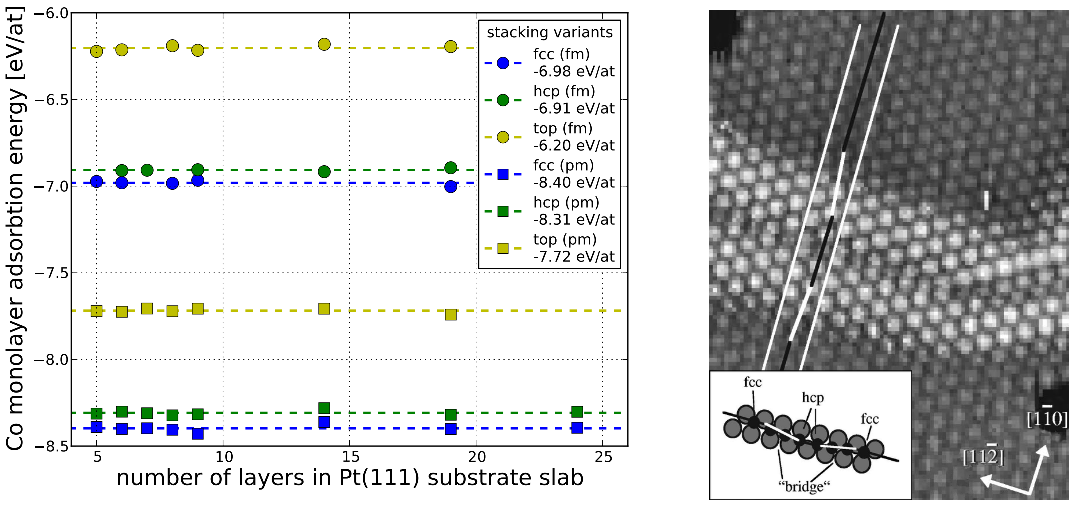

Figure 3.15: Co monolayer adsorption energy with respect to the Pt(111) slab thickness in ferromagnetic (circles) and paramagnetic (squares) case. Dashed line corresponds to the mean value. Results for fcc (blue), hcp (green) and on-top (yellow) variants are presented (left picture). Fragment of STM picture taken from [11] showing Pt(111) surface covered by thin Co layer with two stacking variants: fcc and hcp (right picture).

3.2.2 Charge analysis and local magnetic properties

Results obtained in case of surface sites in mixed systems allow to evaluate the impact of site coordination on the charge redistribution and local magnetic moments. Analysis of profiles shown in Fig. 3.16 leads to the conclusion that the charges are almost not affected by the mixing effects: the charges obtained for the Pt pure surface sites is nearly the same as charges in the presence of Co monolayer and the charges on Co layer are equal to the charges in bulk Co or pure Co surface. While there is no significant charge transfer one can notice well pronounced spin polarization change: magnetic moment of Co atoms in this case are considerably higher than those reported for pure surface and pure bulk sites. In order to better disentangle site coordination effect versus alloying effect on local magnetic properties the value of the spin local magnetic moment on a Co impurity placed into a Pt bulk matrix has been added in Fig. 3.16. As expected one can see that the local magnetic moment is increasing from bulk Co to pure Co surface due to bond breaking at the surface i.e. due to the reducing site coordination. Then having the Co adlayer on top of a Pt substrate instead of a Co one leads to an additional increase, this time much higher showing the importance of alloying effect. However here, to the alloying effect should be also added the effect of epitaxy since the Co adlayer is strained to the lattice parameter of Pt much larger than the Co natural bulk lattice leading to a magnetic behavior even closer to an atomic-like one. The importance of alloying over bond breaking is rather supported by considering the case of a Co impurity into a Pt matrix (no bond breaking in this case) where the spin local magnetic moment reaches its maximum with a slightly higher value than in the case of Co/Pt(111) making the two cases rather similar with regard to local magnetic properties. The latter comparison shows definitely that alloy effect prevails on site coordination effect in the enhancement of magnetic moment. Platinum atoms in the vicinity of cobalt are also slightly polarized but this effect vanishes after roughly 3 atomic layers. These observations, in particular the values of local magnetic moments and its geometrical distribution on sites are in excellent agreement with available experimental data [139, 136].

In order to get more insight into charge redistribution on surface sites of different mixing rank one can analyze charge in the case of the surface of slabs with different degrees of order. Let us recall here that the slabs used in this case are built of stacked (100) planes (i.e. at the surface Z_i=8) while the previous study of Co/Pt(111) was involving surfaces with (111) orientation. Results are reported in Fig. 3.17. Comparison with analogous relationship analyzed earlier in the bulk (Fig. 3.8) reveals no significant charge modification neither between sites of different mixing rank nor for those with different coordination number.

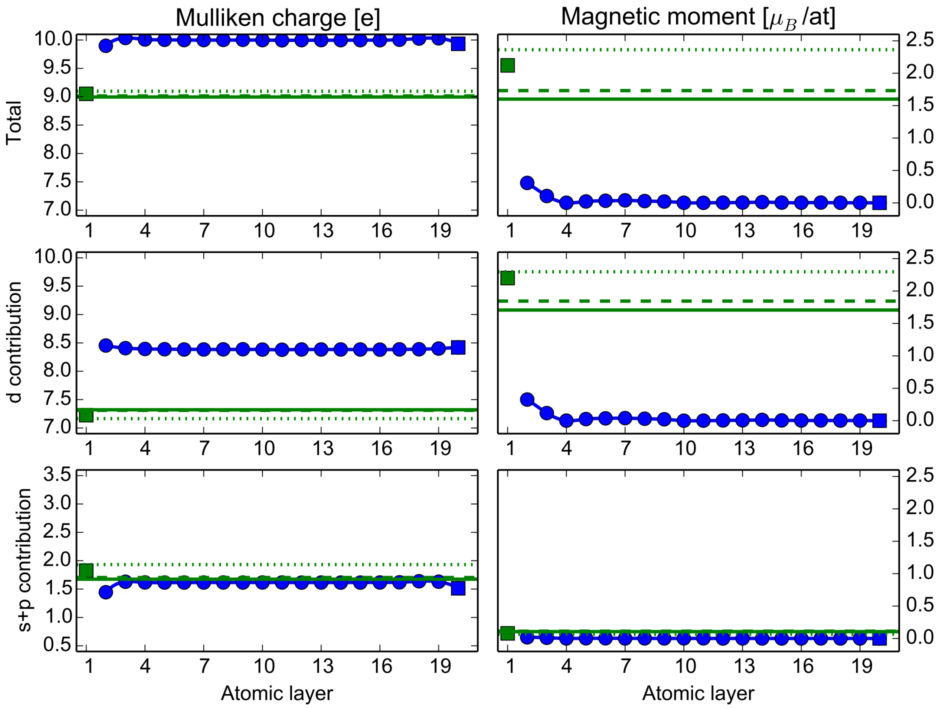

Figure 3.16: Charge and magnetic moment (total and broken down by d and s+p contributions) evolution across Pt(111) slab (19 layers, blue) with Co fcc-stacked adsorbate (monolayer, green). Surface sites are marked by squares. Solid, dashed and dotted line denotes respectively values for Co bulk, surface and impurity sites. Stacking variant has no impact on these results (fcc stacking is shown).

Local magnetic moment increases both in case of lower coordination and with higher mixing rank. In case of Co sites the increase due to the coordination effect is from 1.61 μ_B/atom in pure bulk to 1.78 μ_B/atom on Co(0001) surface) and due to the grow-

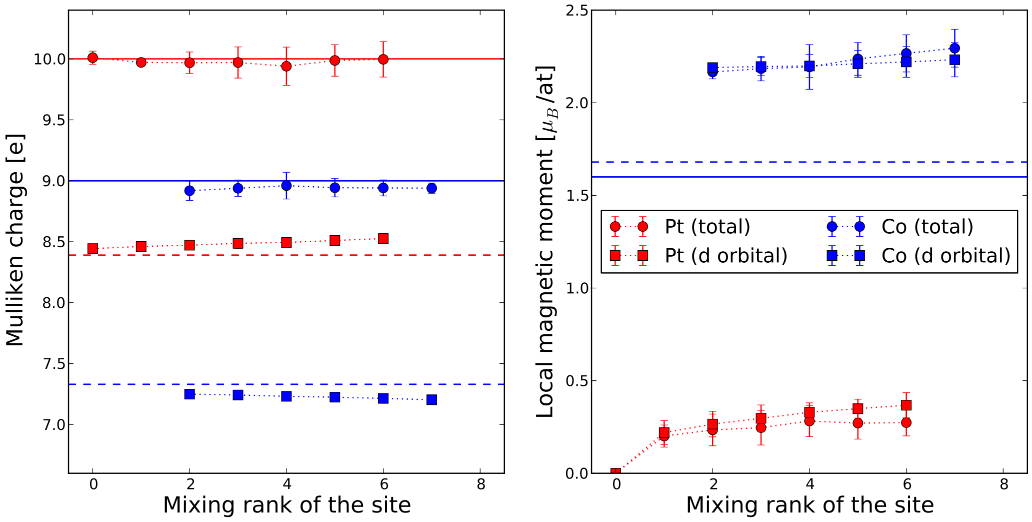

Figure 3.17: Comparison of the Mulliken total (circles) and d-orbital (squares) charges (left plot) and local magnetic moments (right plot) with respect to the site mixing rank for platinum (red) and cobalt (blue) sites. This is the average calculated over all surface (Z=8) sites of all considered samples within CoPt slabs of different order parameter η ranging from 0 to 1 (in the case of $\eta = 1$ the surface is supposed to be terminated by Pt). Respective pure bulk values are marked with horizontal lines (dashed for d-orbital). A similar analysis for bulk sites has been presented earlier in Fig. 3.8.

ing mixing rank - up to 2.36 μ_B/atom in the case of Co impurity and 2.14 μ_B/atom in case of Co monolayer on Pt(111) where both effects are present (Fig. 3.16). Polarization of spins on Pt sites is related to their non-zero mixing rank. It is, however, more pronounced on low-coordinated sites, i.e. local magnetic moment on Pt-terminated (100) surface of L1$_0$ CoPt is 30% higher than on Pt impurity into a Co matrix.

3.2.3 Densities of states

So far the effects of coordination and mixing on the local density of states were studied separately. The results discussed in this section allow to account for the interplay between them. Before going into the most complicated case of mixed clusters it is worthwhile to analyze the influence of the substrate on the surface layer in simpler systems. Pt(111) system with Co monolayer allows to observe how the presence of the Co-Pt interface influences the local electronic structure. In the Fig. 3.18 the difference between pure Co surface and the Co monolayer on Pt(111) substrate are clearly visible - the density of states in the latter case is narrower and more polarized (increased magnetic moment). Density of states of Pt(111) surface covered by Co monolayer is slightly polarized as well. In case of platinum the LDOS narrowing on pure surface sites with respect to the sites in the bulk can be considered a coordination effect since the band width of platinum sites in mixed environment near to the Co-Pt interface is not modified. As we noted earlier similarities between the case of Co/Pt(111) and the case of Co impurity into a Pt matrix, the densities of states of the latter case are reported again in Fig. 3.18. Then it can be actually seen that the Co/Pt(111) case is somewhat similar to the dilute Pt(Co) bulk case, although in the case of Co/Pt(111) the narrowing of the Co band is now related to the bond breaking at the surface. This comparison confirms the validity to consider both systems as similar upon their local magnetic properties.

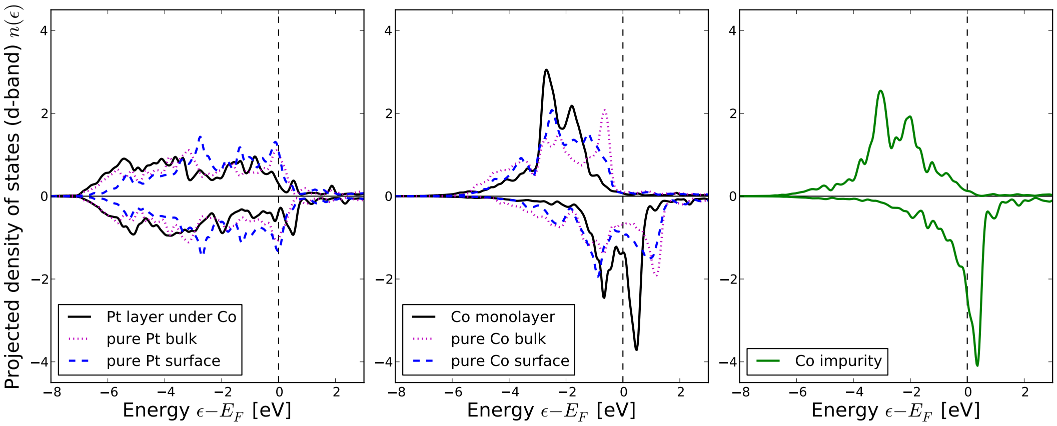

Figure 3.18: Local density of states of platinum (left) and cobalt (middle) sites in the presence of Co-Pt interface between Co monolayer and Pt(111) slab (solid black) and, for reference, on pure surface (dashed blue) and inside pure slab (magenta dots). The case of a Co impurity placed into a Pt matrix is represented on the right graph (green plot).

3.3 Nanoalloys: cuboctahedral and icosahedral clusters

Further extension of the studies presented in last two sections is to investigate mixed systems with not only single surface, but also less coordinated sites like edges and vertices and to observe the charge redistribution, local magnetic moment alteration and local densities of state within broader range of possible environments of the atomic site. To this aim we have performed calculations on mixed clusters up to 561 atoms. Two configurations were selected: cuboctahedral with $\mathrm{L1_0}$ chemical ordering and icosahedral composed of alternating shells of Co and Pt (Fig. 3.19). The number of Co and Pt sites is not equal and, therefore, two variants of slightly different stoichiometry (ranging from 44 to 56%) are always possible. For detailed description of geometrical features of each structure refer to the relevant section of chapter 2. We will consider here two characteristic shapes and chemical arrangements namely icosahedra with concentric alternating shells of Co and Pt and cuboctahedra showing a $L1_0$ like arrangement with alternating (100) planes of Co and Pt. This choice was motivated by the DFT study presented in [61]. Note that here atomic relaxations were not taken into account which would have led to too time consuming calculations for the considered set of clusters.

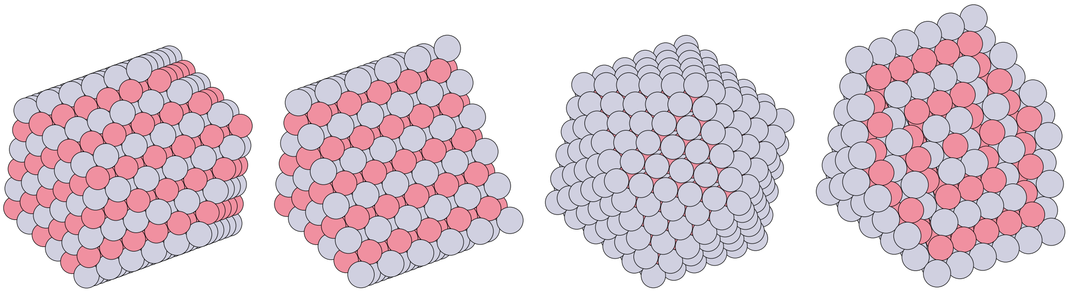

Figure 3.19: Mixed cluster morphologies (from left to right): cuboctahedral $L1_0$ (with cross-section) and icosahedral onion-like (with cross-section). The cluster size is 561 at.

3.3.1 Charge analysis and local magnetic properties

Following the procedure adopted in previous sections we have analyzed the charges and local magnetic moments with respect to the site coordination and mixing rank (Fig. 3.20). The disordered systems were not considered here. The calculated charges are within numerical accuracy in agreement with respective pure bulk values which is a very important result for the implementation of charge neutrality rule in TBA calculations. The notable exceptions are the least coordinated cobalt sites (edges/vertices), however, the charge variation does not exceed 0.5 e even in the extreme cases (i.e. low-coordinated cobalt sites). In case of local magnetic moment the results for platinum sites exhibit behavior similar to the one already observed in case of bulk (Fig. 3.8) and surface sites (Fig. 3.17) - the magnetic moment emerges with non-zero mixing rank and then saturates. Decreasing site coordination number only very slightly enhances the local magnetic moment. Conversely, while local magnetic moment of highly coordinated cobalt sites is in agreement with values obtained in bulk systems with the same mixing rank, the decreasing site coordination (denoted by smaller points on the right plot in Fig. 3.20) substantially enhances the observed local magnetic moment leading to total values by over 0.5 μ_B/atom higher in extreme cases ($M_i < 5$).
The local electronic properties (LDOS) on various sites will be discussed in greater detail along with the TBA results in the next chapter where they will be also used for comparison to assess the accuracy of the latter method.

3.4 Conclusions

Although some uncertainties are arising from the more or less arbitrary charge analyses, we can conclude here on the overall study that a local neutrality has been obtained per site, species and orbital. Some limits of the strict generality are found since there is a slight charge transfer between spin orientations related to the changes of the magnetic moment and in the case of platinum the charge distribution starts to deviate from neutrality in the diluted CoPt systems. However for the cases most interesting for applications and especially for surfaces and clusters, it shall be sufficient to use the neutrality rule in further TBA calculations. Apart from this most important result a number of other informative observations were made: having successfully reproduced

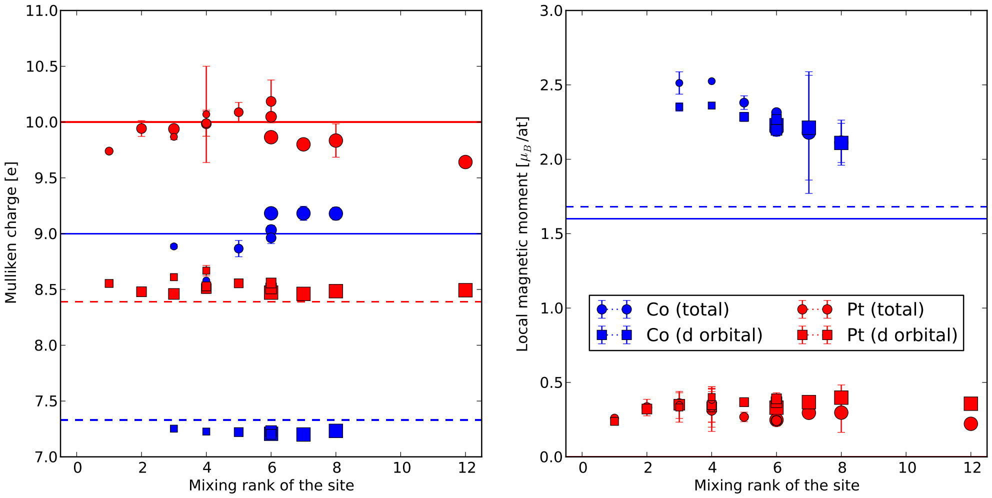

Figure 3.20: Mulliken charge redistribution (left) and local magnetic moment (right) on small clusters with respect to to the mixing rank of the site for platinum (red) and cobalt (blue) sites. Marker size correspond to the coordination number. Each point was calculated as an average over all equivalent sites (in terms of occupancy, coordination number and mixing rank) for all considered cluster morphologies, sizes and stoichiometries.

the basic properties of mixed bulk systems we have also addressed the importance of magnetism on the CoPt ordered phase stability proving for broad range of concentration that magnetic interactions are responsible for the structure stabilization. The calculated heats of formation are in very good agreement with other calculations and measurements. Disordered systems were also analyzed leading to an important evidence regarding the evolution tendencies of the average charge and the local magnetic moments. It has been found that in almost all cases, even with high mixing rank the charge distribution does not differ from the one observed in a pure bulk, which is especially well marked in the most important case of d-orbital charges. We have also systematically investigated the tendencies of local magnetic moment evolution with respect to the mixing rank and the modification of these tendencies with a decreasing site coordination number. We have found, that in the case of Pt sites local magnetic moment is mainly induced by the non-zero mixing rank and in some cases is slightly enhanced on low-coordinated sites, while in the case of Co sites the local magnetic moment grows considerably with the mixing rank and with decreasing coordination number. This result was obtained with decent statistics allowing to eliminate the effects stemming from the geometrical differences in the atomic arrangement and atomic configuration of more distant coordination zones resulting in the same mixing rank. Part of this work has been recently published in Electrochimica Acta [143]. An important feature of the present study was also the systematic evaluation of local magnetic moments with respect to the environment of a given site where we were able to reach very good level of compliance with the experimental values in the case of the thin Co layer deposited on Pt(111) surface. In this system we have also successfully recovered the experimentally observed preference for the fcc stacking of Co layer with a possibility of a co-existence with the hcp variant which was energetically less favorable. As the most important conclusion remains, however, the evidence obtained to support the choice of the local neutrality rule in the case of mixed and low-coordinated sites that will be used in the calculations in the next chapter.

Chapter 4

TBA calculations of realistic systems

The results of ab-initio DFT calculations discussed in the previous chapters allow not only justifying the charge redistribution related assumptions (mainly the local neutrality rule per site, species and orbital) but also verifying the validity of the Tight Binding method by direct comparison with DFT results as presented in this chapter. This verification, performed for the local densities of state within a broad selection of most typical systems will be discussed in the second section of this chapter after having given some additional features on the application of the TB methodology to nanoalloys. Application of the self-consistent Tight Binding method actually allows extending the scope of calculations to clusters of “realistic“ sizes as used in experiments, ranging from few tens to few thousands of atoms. The results of quantitative analysis of the local electronic structure’s features that are most important for the interpretation of local properties (as for instance band shifts for catalysis or density at Fermi level for magnetism) will be presented in the following section. Data like. ε_d should provide guidance to the interpretation of core level shifts measurements using X-Ray photoemission spectroscopy (XPS) in nanoalloys, a widely used technique in the field of catalysis for instance. Then last section is devoted to the fundamental question of order tendency in nanoalloys by still using the example of CoPt. In this case the work is dedicated to the determination of the two pertinent parameters characterizing order in an AB nanoalloy namely the *diagonal disorder* parameter $\delta_{d,0} = \varepsilon_d^A - \varepsilon_d^B$ (difference between gravity centers of the d-bands, ε_d) and *off-diagonal disorder* parameter $\delta_{nd} = W_d^A - W_d^B$ (difference between d-band widths, W_d). These values have been shown to allow deriving ordering tendencies in all bulk transition metal alloys [37]. We further intend here to derive a law for the evolution of these parameters as a function of the size of clusters and to provide a tool for predicting ordering tendency in nanoalloys as a function of size which is an essential step for scientists willing to control the atomic arrangements in the fabrication of specific clusters for targeted properties. Most of the work presented in the following is the object of an article recently published in Physical Review B [144].

4.1 Additional features for the use of tight-binding: from alloys to nanoalloys

For an alloy A_cB_{1-c}, the chemical configuration is defined from the set of site occupation factors p_i^a such as $p_i^a = 1$ if site i is occupied by an atom of type a ($a = A, B$) and $p_i^a = 0$ otherwise. Then the corresponding Hamiltonian is written in the basis of atomic orbitals λ at sites i, $|i, \lambda\rangle$:

$$\begin{aligned}H(p_i^a) &= \sum_{a=A,B}\sum_{i,\lambda} p_i^a |i,\lambda\rangle \varepsilon_{i\lambda}^a \langle i,\lambda| \\ &+ \sum_{a,b=A,B}\sum_{i,j\neq i,\lambda,\mu\neq\lambda} p_i^a p_j^b |j,\mu\rangle (\beta_{ij}^{\lambda,\mu})^{ab} \langle i,\lambda| \end{aligned} \tag{4.1}$$

which involves the effective atomic levels $\varepsilon_{i\lambda}^a$ and the hopping integrals $(\beta_{ij}^{\lambda,\mu})^{ab}$. In this framework ε_d^a is the atomic d orbital level for an atom of the type a ($a = A, B$) in its own bulk and the hopping integral between two d-orbitals on neighboring sites drives the d bandwidth (W_d^a) [145]. The first term gives rise to the so-called *diagonal disorder* effect coming from the difference $\delta_{d,0} = \varepsilon_d^A - \varepsilon_d^B$ whereas the second one accounts for the possible effect of *off-diagonal disorder* due to the difference in d bandwidth: $\delta_{nd} = W_d^A - W_d^B$. These two parameters $\delta_{d,0}$ and δ_{nd} actually drive the redistribution of the electronic states with respect to those of pure elements and therefore both the new properties of the (nano)alloy and its preference for ordering or phase separation at low temperature. Based on these parameters, well known from compilations in the literature [102], systematic studies within the TB approach were previously carried out for deriving ordering tendencies in all bulk transition metal alloys [37] and general trends in d-band and core level shifts [146], the latter being tightly related e.g. to catalytic properties. The next step of the present work is to combine site coordination effects (atomic structure) and alloying effects (chemical structure) in a single model for nanoalloys in the experimental size range (up to thousands of atoms). The essential quantity to study is the local density of states (LDOS), $n(E)$. The method of calculation has been described in first chapter and its main features are just recalled here. In all cases $sp-d$ hybridization is taken into account by using the basis of atomic orbitals $\lambda(s, p, d)$. Each partial LDOS $n_{i\lambda}(E)$ is obtained from the continued fraction expansion of the Green function $G(E) = (E - H)^{-1}$ whose coefficients are directly related to the moments of the density of states. These coefficients are calculated within the recursion method [36] implemented with a self-consistent treatment of charge transfer induced by both coordination changes and alloying effects. The technique makes use of a local charge neutrality rule *per site*, *per orbital* and *per chemical species*, well known for surface effects as already discussed. Now it is extended to CoPt alloys from DFT calculations of this work. Here a new application of this TB approach for nanoalloys is proposed where both alloying and structural effects are included in the same procedure. In practice ten pairs of exact coefficients are considered in order to obtain sufficiently detailed LDOS. The main difficulty is then to determine the effective atomic level $\varepsilon_{i\lambda}$ for each inequivalent site i, while ensuring the charge self-consistency on this site. This requires, after indexing all inequivalent sites i and species a, that these levels are shifted for each orbital λ with respect to those in the bulk by a value $\delta\varepsilon_{i\lambda}^a$ following:

$$\varepsilon_{i\lambda}^a = \varepsilon_{0\lambda}^a + \delta\varepsilon_{i\lambda}^a \tag{4.2}$$

in order to satisfy a given rule (here the local neutrality rule) on the different band fillings per orbital and per species $N_{i\lambda}^a$, which are obtained by integration of the partial local densities of states up to the Fermi level E_F:

$$N^a_{i\lambda} = \int_{-\infty}^{E_F} n^a_{i\lambda}(E)dE \tag{4.3}$$

The total band filling (number of valence electrons) at site i, occupied by an atom of type a is then determined by summing over all orbitals such as $N^a_i = \sum_\lambda N^a_{i\lambda}$.

In the self-consistency cycle, $\delta\varepsilon^a_{i\lambda}$ is varied until charge per Co or Pt atom and orbital at each site reaches the target bulk value by fixing the common Fermi level either at the position of that in the matrix (only in the dilute case for a bulk system) or by varying it at each step to keep the total charge for any other alloy system (bulk alloy or nanoalloy).

If interested in relative stability of different chemical configurations one has in general to calculate the band contribution to the energy of the considered systems to be compared. This can be performed by simply integrating the LDOS calculated as described above, without forgetting to subtract the double counted terms due to the level shift issued from the self consistent procedure:

$$E^a_{i\lambda} = \int_{-\infty}^{E_F} En^a_{i\lambda}(E, \delta\varepsilon^a_{i\lambda})dE - N^a_{i\lambda}\delta\varepsilon^a_{i\lambda} \tag{4.4}$$

where $N^a_{i\lambda}$ is the number of electrons per orbital in bulk a material, unchanged in any other site (surface, alloy, cluster) following the adopted local neutrality rule. The sum over all orbitals will give the band energy for site i and the further sum over all sites i will give the contribution of a atoms to the total band energy.

The remaining parameters of the model are the hopping integrals between orbitals of neighboring sites, $(\beta^{\lambda,\mu}_{ij})^{ab}$. If $a = b$ the values are directly taken from the compilation of D. A. Papaconstantopoulos [102] designed for elemental solids. For the specific case of Co, the parameters for the structural fcc paramagnetic phase were applied, in agreement with the fcc structure of the clusters considered hereafter. If $a \neq b$ the arithmetic average of $\beta^{\lambda,a}$ and $\beta^{\lambda,b}$ is used. Magnetism was not explicitly included in the TB calculations but some considerations about it will be given in the last section of this chapter.

From the obtained *spd* LDOS, the most meaningful partial $d-$LDOS will be extracted and then the main characteristic quantities deduced: d-band center ε_d, d-band width W_d, diagonal and off-diagonal disorders. The values of ε^a_d and W^a_d can be calculated directly from the relevant density of states $n_d(E)$ using the following formulas:

$$\varepsilon_d = \frac{\int_{-\infty}^{+\infty} n_d(E)\, E\, dE}{\int_{-\infty}^{+\infty} n_d(E)\, dE} \qquad \text{- the first raw moment of } n(E) \tag{4.5}$$

$$W_d = \sqrt{8\ln 2 \cdot \frac{\int_{-\infty}^{+\infty} (E-\varepsilon_d)^2\, n_d(E)\, E}{\int_{-\infty}^{+\infty} n_d(E)\, dE}} \qquad \text{- full width at half maximum} \tag{4.6}$$

4.2 Compatibility of the TBA and DFT results

The validity of this TB method must be first supported by more fundamental *ab initio* calculations on the basic bulk phase alloys since the description of ordering behavior of complex nanoalloys is necessarily related to the bulk phase diagrams. We shall thereby verify the relative stability of the usual bulk alloy phases against possible competing ones. On the other hand the method must be proved to provide reliable local densities of states on which all interpretations in terms of local properties (as for instance band shifts for catalysis or density at Fermi level for magnetism) are related. For both purposes *ab initio* complementary DFT calculations were performed with the SIESTA-GGA method used in the previous chapters.

4.2.1 Comparison of relative stability energies

The low temperature experimental phase diagram of CoPt is characterized by three main ordered phases [147, 8], the fcc L1_2 ($Co_{0.25}Pt_{0.75}$ and $Co_{0.75}Pt_{0.25}$) and the fct (tetragonalized with regards to fcc) L1_0 phase at equiconcentration. However, while considering in this work only the fcc crystalline structure, two ordered phases have to be considered at c=0.25 concentration, in what is concerned relative stability, namely L1_2 (Cu_3Au type) and also DO_{22} (Al_3Ti type). For c=0.5 if L1_0 has to be the most stable it should be checked that the TB model well predicts this stability against other phases like the bcc B_2 one. In this context we have calculated the relative stability energy ΔE_{stab} of the different ordered structures, at c=0.25 and c=0.5, both with DFT and TB methods. Within the latter only band energy, *i.e* the explicit term issuing from the electronic structure, has been considered using e.g. 4.4 and summing partial contributions of Co and Pt while accounting for their respective concentration in the considered systems. The results are presented in Tab. 4.2.1.

Alloy composition ΔE_{stab} [eV/atom]	$Co_{0.75}Pt_{0.25}$ $E_{L1_2} - E_{DO_{22}}$	$Co_{0.5}Pt_{0.5}$ $E_{L1_0} - E_{B_2}$	$Co_{0.25}Pt_{0.75}$ $E_{L1_2} - E_{DO_{22}}$
DFT (magnetic)	0.001	-0.247	-0.007
DFT (non magnetic)	0.003	-0.337	-0.012
TB (non magnetic)	0.028	-2.635	-0.128

Table 4.1: Relative stability energy ΔE_{stab} (eV/atom) between several bulk CoPt ordered alloys at different concentrations. DFT calculations were performed with (magnetic) and without (non magnetic) spin polarization.

There is a full consistency between DFT and TB concerning the sign of the obtained values of ΔE_{stab} and the hierarchy of the obtained relative energies. Absolute TB values of ΔE_{stab} are however different by about one order of magnitude than DFT ones. More surprising is the apparent degeneracy between the L1_2 and DO_{22} ordered structures obtained both in DFT and TB although the experimental phase diagram shows only the $L1_2$ structure around $c = 0.25$ (or $c = 0.75$) with the Co_3Pt L1_2 phase being less marked [29]. However, it should be kept in mind that the structural difference between the $L1_2$ and DO_{22} consists only of the insertion of an anti-phase boundary between two fcc unit cells leading to a periodic ordering on two fcc cells instead of one, making the two structures rather similar. Therefore the related energies of these two phases should not differ too much. This is deduced from a description of their density of states in terms of their moments, the DOS of the $L1_2$ and DO_{22} structures having six identical moments [148]. In the same sense, recent almost exhaustive calculations of bulk Co-Pt structures by R. V. Chepulskii and S. Curtarolo resulted in very close values for Co_3Pt $L1_2$ and DO_{22} phases [133].

4.2.2 Direct comparison of the densities of state

Since all the analyses of the electronic structure will be based on the local density of states the most straightforward way of comparing TBA and DFT results is to superimpose respective LDOS curves normalized with $E_F = 0$ as shown in Figs. 4.1, 4.2 and 4.3 and comment the results through the prism of charge transfers discussed in previous chapters.

In the case of systems compared in Fig. 4.1 the best agreement occurs obviously in the case of pure materials (first two plots). For mixed systems one can observe small discrepancies, but the tendencies in evolution of the LDOS shapes with changing concentration are well reproduced. Most notable exception is diluted platinum systems for which the position of the main peak of platinum atom density of states obtained from TBA calculations is considerably shifted towards Fermi level compared to the reference DFT result. This can be correlated with relatively high charge redistribution observed earlier in this particular system.

The most important step is, however, to verify the LDOS-es calculated within TBA method in the case of low coordinated sites on cluster surface. Local densities of state on selected site classes have been collected in the Fig. 4.2. The most important features are very well reproduced, the only exceptions are already observed in case of CoPt $L1_0$ bulk, slightly broader Pt band for sites inside cluster and misplaced peaks of Pt LDOS calculated on mixed edge located at the intersection of mixed (100) and (111) surfaces. On sites where charge redistribution strictly adheres to the local neutrality rule (see LDOS of pure Pt surfaces) the agreement is clearly better. There is also a good agreement in terms of averaged cluster PDOS (Fig. 4.3).

These comparisons justify the reliability of self-consistent TB model in determining accurately the distribution of electronic states on inequivalent sites of nanoalloys and bulk systems. At the same time it allows identifying its limits when the single form of self-consistency condition through the local neutrality rule is employed. However, even if some deviations from the neutrality rule have been observed in a few cases in the calculations, but also in some experiments [149, 150, 151], our choice for nanoalloys remains to join a single law in order to bring the overall behavior of transition metal alloys under a single description which was already shown, in the case of bulk alloys, to be sufficient to describe d-band shifts and obtain a good agreement with photoemission experiments [146].

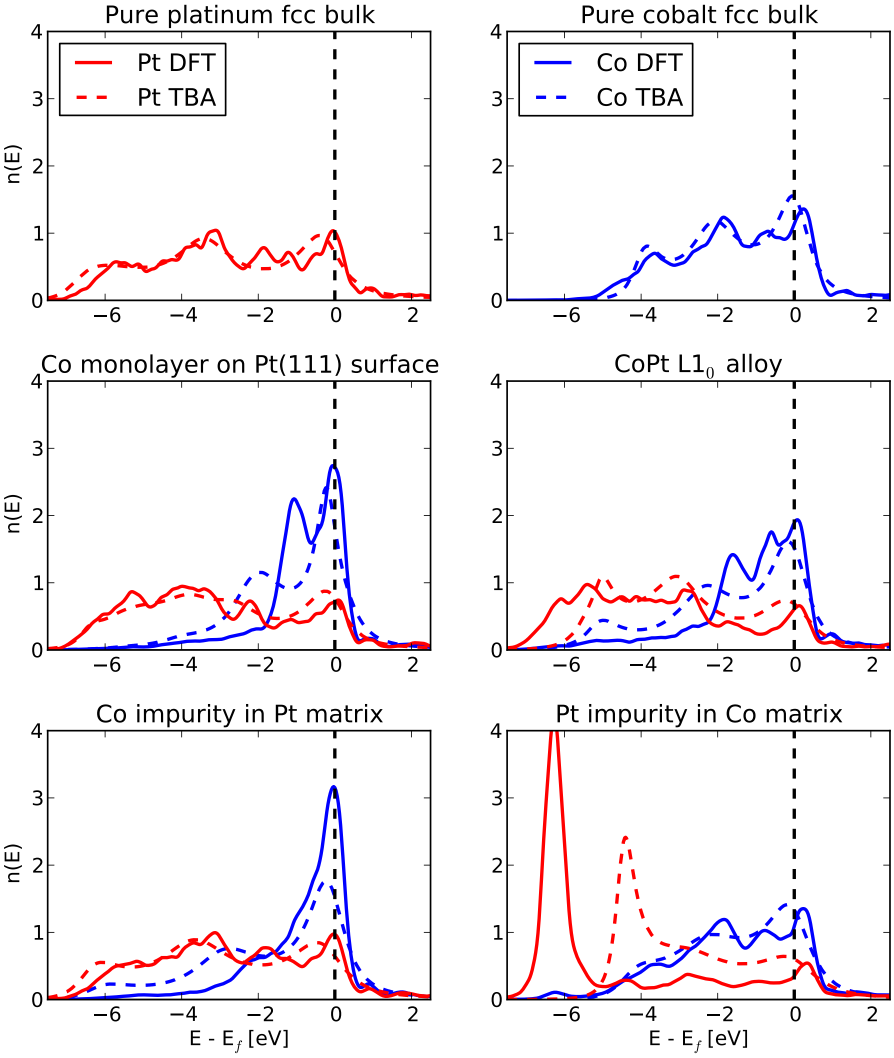

Figure 4.1: Comparison of the LDOS obtained from paramagnetic TBA (dashed lines) and DFT (solid lines) calculations for cobalt (blue) and platinum (red) sites in pure and mixed infinite systems (bulk and interfaces).

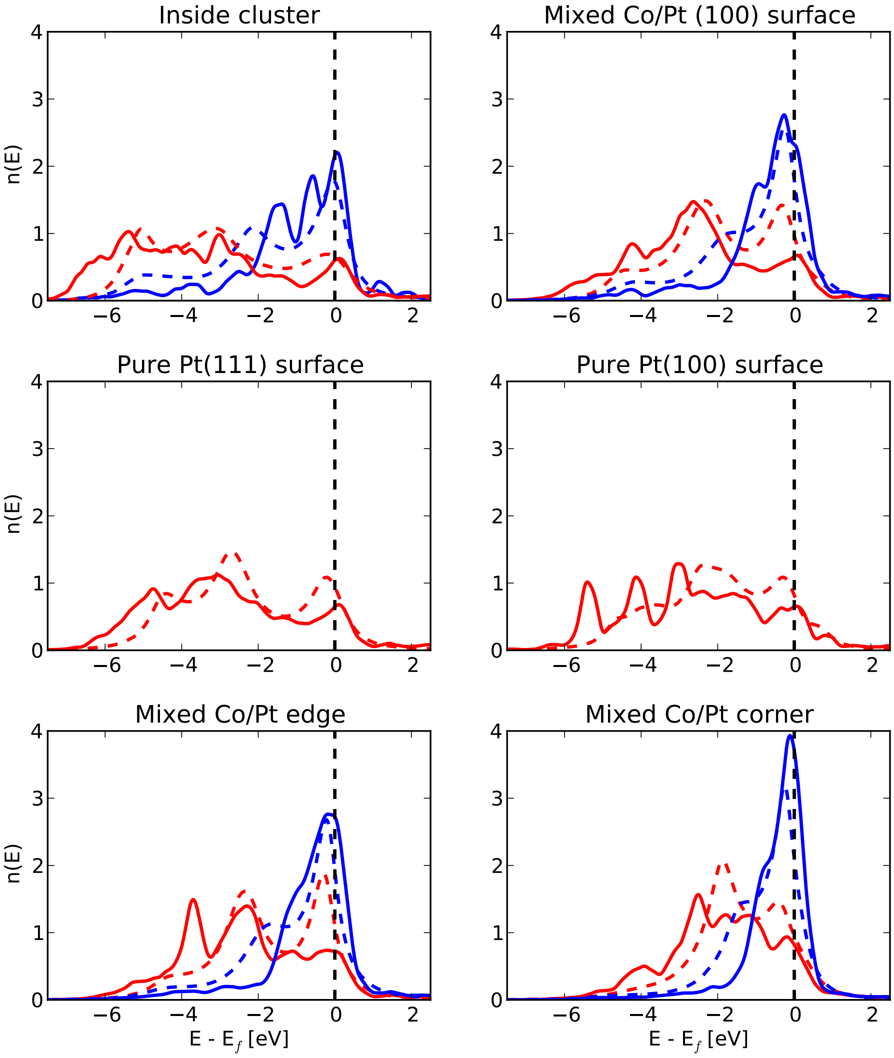

Figure 4.2: Comparison of the LDOS obtained from paramagnetic TBA (dashed lines) and DFT (solid lines) calculations for various cobalt (blue) and platinum (red) sites in cuboctahedral clusters of 309 atoms with $L1_0$ ordering.

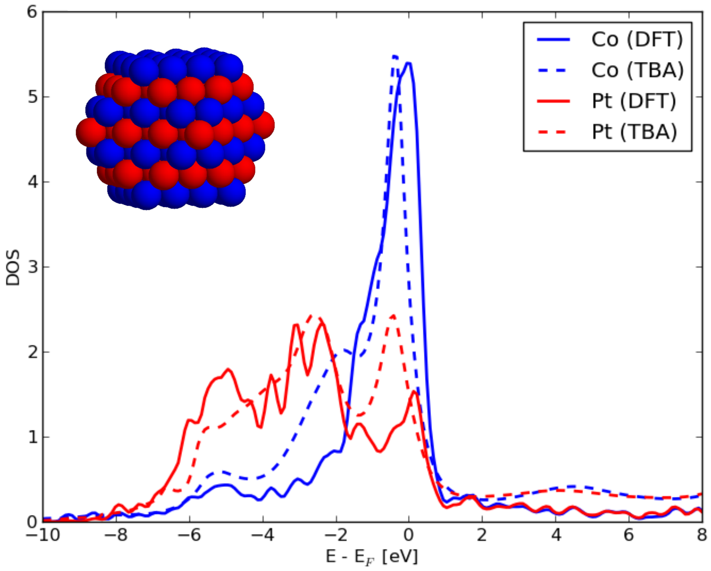

Figure 4.3: Averaged DOS (sp-d, non magnetic) in a cuboctahedral CoPt $L1_0$-like cluster of 147 atoms. Solid lines correspond to DFT calculations and dashed ones to TB calculations. The insertion shows the corresponding atomic structure. Color code for both curves and structure in insertion is blue for Co and red for Pt.

4.3 Mixed clusters: analysis of d-band position and width

Pure clusters have been more extensively studied in the past with the TB method [117, 152]. Therefore they were not studied here in detail and this work was rather focused on the mixed clusters which are the most interesting in the current fields of applications where alloying effects are employed in order to obtain new properties either magnetic or catalytic. Studies available in the literature [153, 61, 154] show that several shapes and chemical arrangements are possible for those clusters, including polyicosahedral onion-like structures typical for small clusters, decahedra and truncated octahedra with L1_0-like structure that are stable for larger sizes. In the present study the chosen model shape for fcc clusters of sufficiently big size is the cuboctahedral one.

Here we will therefore build a model nanoalloy as a cuboctahedral piece of a bulk fcc $L1_0$ structure. Surfaces of such n-shell clusters in platinum- or cobalt-rich variants are composed of sufficiently large set of inequivalent sites to be considered as representative of realistic systems. The electronic properties of the low-coordinated sites in mixed chemical environment will be compared with analogous sites in pure clusters in order to differentiate chemical and geometrical effects. Fig. 4.4 shows partial d-LDOS for all the inequivalent sites of both a pure Pt and a CoPt cluster. Effective bandwidth decreases with decreasing site coordination (from facets to edges and vertices) and increasing site mixing rank (between sites with the same coordination *e.g.* edge in the pure Pt and in mixed cluster). This is an expected effect that was also observed in the DFT calculations not only for clusters but also for pure and mixed surfaces. Change of the chemical environment of the site also heavily modifies LDOS near the Fermi level which could be related to changes in local magnetic properties.

Since the shifts of the d-band and the d-band width depend on the site coordination it is interesting to investigate the nature of this dependency. Fig. 4.5 shows d-band centers of gravity of platinum and cobalt sites with respect to its coordination number Z for extreme cluster sizes: small (147 atoms) and three times larger in terms of diameter (2869 atoms) both for pure clusters and for binary CoPt system. One can immediately notice nearly linear shift of the ε towards higher energies (both for Pt and for Co) with decreasing site coordination and energetical separation of the d-band centers between pure and mixed systems. It is worth pointing out, that LDOS is almost not affected by the cluster size which supports the statement that electronic structure on given site is a local effect and therefore depends only on modifications of local environment of that site.

The effect of coordination-driven d-band energy level shift is related to the narrowing of the d-band with additional condition of constant charge stemming from the local neutrality rule and nearly constant filling at the Fermi level (upper edge to the band does not move) which leads to concentration of the electronic states just below E_F for decreased site coordination and/or increased site mixing rank. Therefore similar linear tendencies can be observed for the width of the d-band defined as the centered second moment of the LDOS scaled by the same constant which relates the second moment to the actual band width in the bulk - it decreases with decreasing coordination number as can be seen in Fig. 4.6.

In summary the behavior of the d-levels upon alloying in nanoclusters can be estimated by a linear variation law as a function of coordination Z to which an alloying term estimated by a rigid shift is added, allowing separating the structural and chemical effects. The above considerations can be therefore analytically summarized by writing down the atomic d-level ε_Z^a for $a = Co, Pt$:

$$\varepsilon_Z^a = \varepsilon_0^a + \Delta\varepsilon_{\text{alloy}}^a + \Delta\varepsilon_{\text{site}}^a (Z - 12) \tag{4.7}$$

The linear fit (see Fig. 4.5) leads to the following values of the constants: for the alloying term, $\Delta\varepsilon_{\text{alloy}}^{\text{Pt}} = +0.6 \pm 0.15$ eV, $\Delta\varepsilon_{\text{alloy}}^{\text{Co}} = -0.3 \pm 0.1$ eV and for the geometrical term, $\Delta\varepsilon_{\text{site}}^{\text{Pt}} = -0.16$ eV, $\Delta\varepsilon_{\text{site}}^{\text{Co}} = -0.085$ eV.

As a rather similar behavior is found for d-band width, a same linear equation can be derived for d-band width by just replacing ε^a by W^a, with here $\Delta W_{\text{alloy}}^{\text{Pt}} = -1.0 \pm 0.25$ eV, $\Delta W_{\text{alloy}}^{\text{Co}} = +0.6 \pm 0.1$ eV, $\Delta W_{\text{site}}^{\text{Pt}} = -0.4$ eV, and $\Delta W_{\text{site}}^{\text{Co}} = -0.22$ eV. Further approximation of the alloying terms by the values of the actual bulk alloy, which is justified in view of our results, should allow a generalization of these formulations to

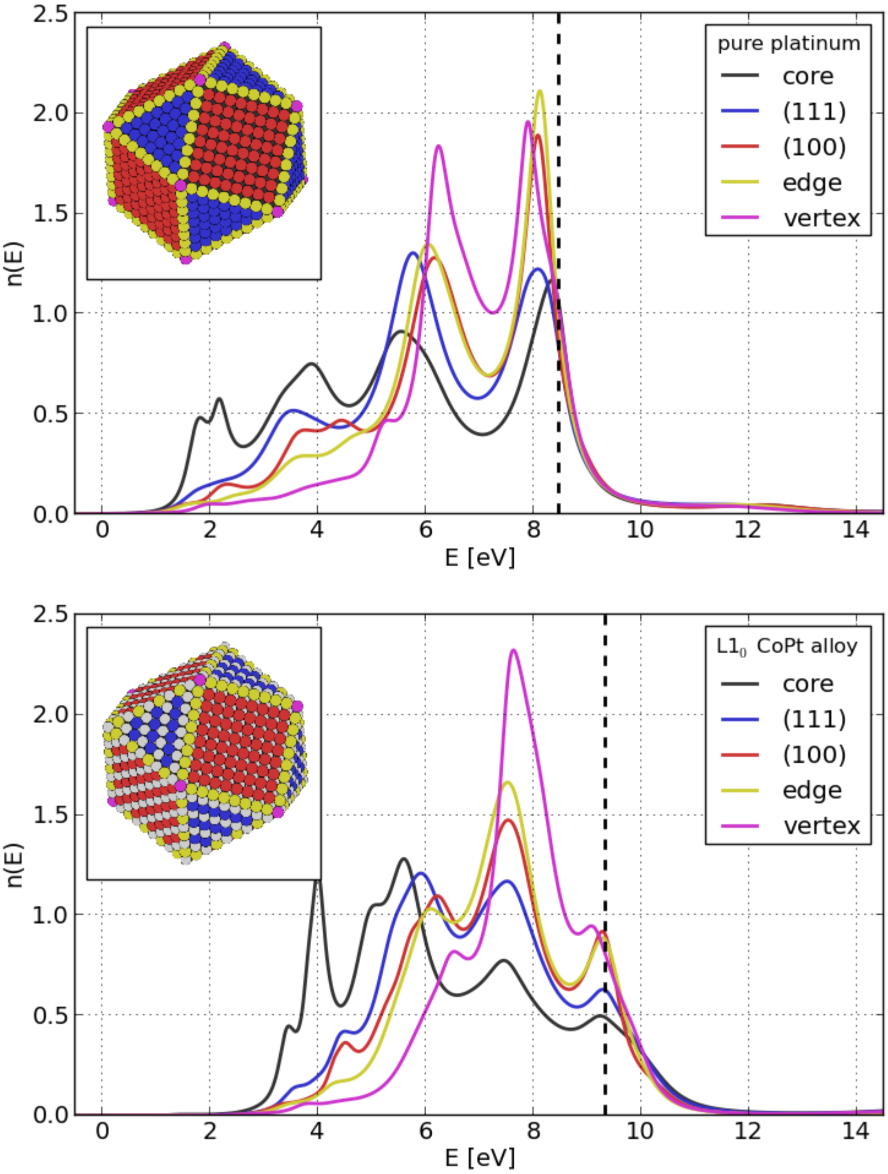

Figure 4.4: Partial d-LDOS on the geometrically inequivalent sites on a cuboctahedral Pt (a) and CoPt $L1_0$-like (b) cluster of 2869 atoms. The insert shows the corresponding atomic structures, in which the sites have been colored upon their environment (coordination, chemical).

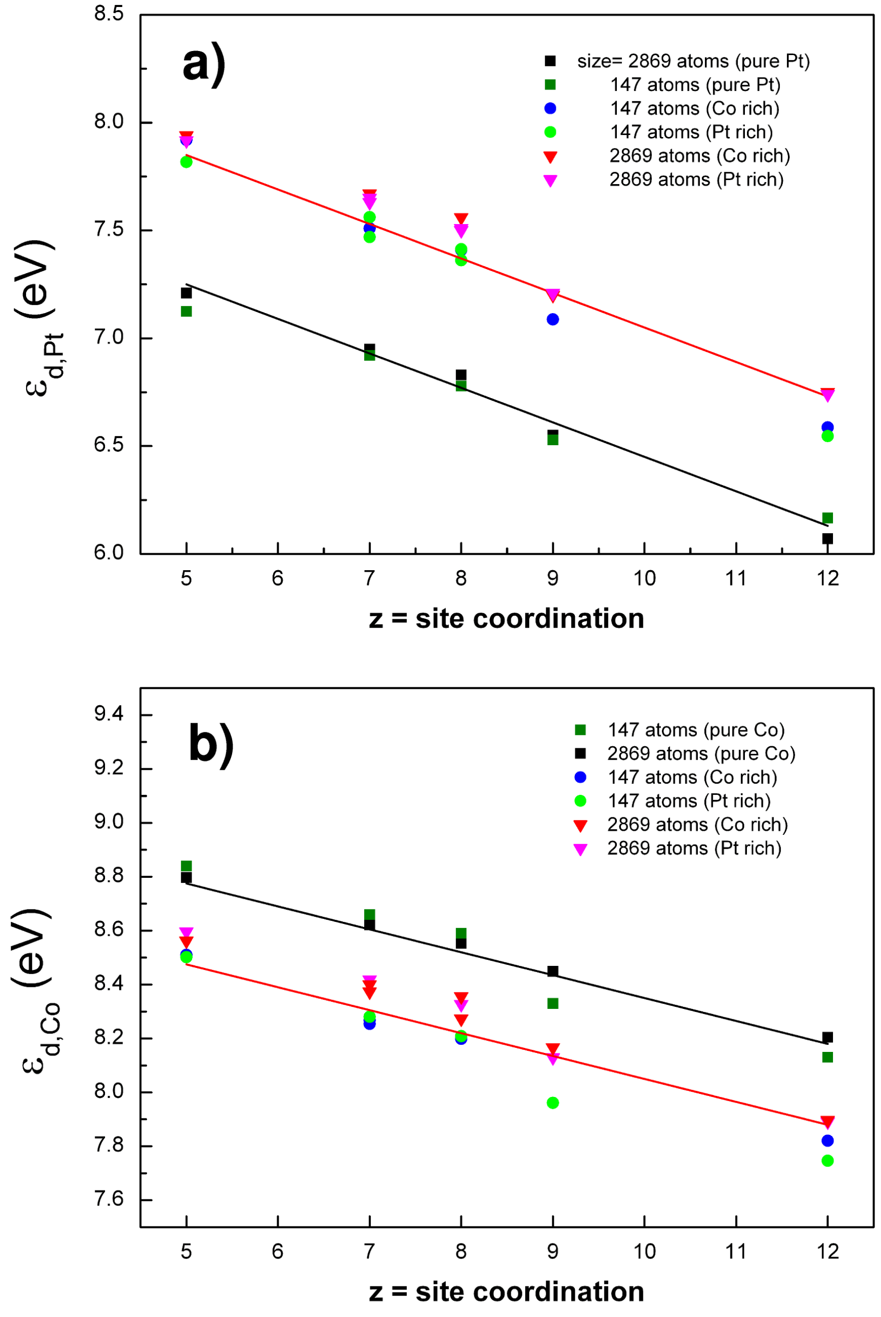

Figure 4.5: Center of gravity of d-band for the geometrically inequivalent Pt (a) and Co (b) sites of cuboctahedral CoPt $L1_0$ like clusters compared respectively to pure Pt and Co clusters. Two sizes are considered: $N_{tot} = 147$ and $N_{tot} = 2869$. Straight lines correspond to linear fits (see text). Label “Co rich” (“Pt rich“) refers to concentration in Co (Pt) > 0.5.

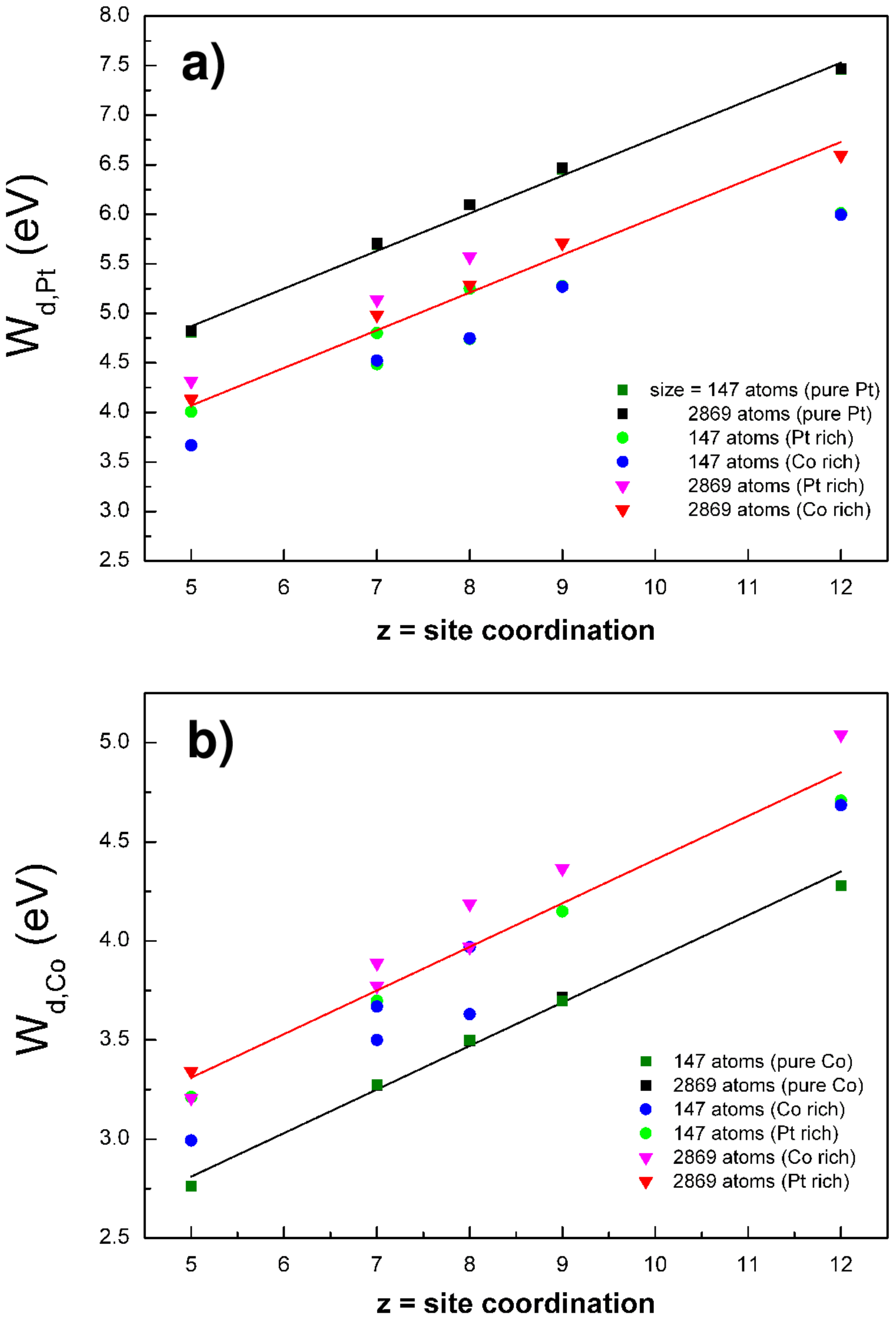

Figure 4.6: Width of the d-band for the geometrically inequivalent Pt (a) and Co (b) sites of cuboctahedral CoPt $L1_0$ like clusters compared respectively to pure Pt and Co clusters. Two sizes are considered: $N_{tot} = 147$ and $N_{tot} = 2869$. Straight lines correspond to linear fits (see text). Label “Co rich” (“Pt rich“) refers to concentration in Co (Pt) > 0.5.

any bimetallic nanoalloy. Then, for a n shells cuboctahedron, one is able to write an analytic formula for the dependence of the average atomic d-levels as a function of the cluster size:

$$\varepsilon_n^a = \varepsilon_0^a + \Delta\varepsilon^a_{\text{alloy}} + \Delta\varepsilon^a_{\text{site}} \sum_{Z=5,7,8,9} x_Z^a \frac{N_Z}{N_{tot}}(Z-12) \tag{4.8}$$

where $N_{tot}(= 1 + \frac{n}{3}(10n^2 + 15n + 11))$ is the total number of atoms, and the summation over Z means summing over the different under-coordinated sites, the respective numbers of which is N_Z: $N_{Z=5} = 12$ vertices, $N_{Z=7} = 24(n-1)$ edge atoms, $N_{Z=8} = 6(n-1)^2$ atoms for the (100) facet, $N_{Z=9} = 4(n-1)(n-2)$ atoms for the (111) facet. $x_Z^a = c_Z^a/c^a$ is the ratio between the partial a-concentration at a site of coordination Z and c^a the global a concentration in the whole cluster. Here again, a similar equation can be used to describe the size-dependence of the effective d-bandwidth by just replacing ε^a by W^a.

4.4 Ordering trends in nanoalloys

From the results of the previous section, we are now able to return to the question of the ordering tendency in nanoalloys the ultimate goal being to be able to predict this tendency for any transition metal nanoalloy as a function of its size. Following the previous work on bulk alloy [37], the ordering tendency for a cluster of order n will be linked to the differences $\delta_d^n = \varepsilon_n^{Co} - \varepsilon_n^{Pt}$ and $\delta_{\text{nd}}^n = W_n^{\text{Co}} - W_n^{\text{Pt}}$ obtained either by averaging all the Pt and Co LDOS in the cluster, respectively, or using the previously derived linear law. Averaging over all possible configurations in each case gives the law of variation for δ_d^n as a function of the size of the cluster, which writes analytically as:

$$\begin{aligned}\delta_d^n &= \delta_{d,0} + \Delta\varepsilon^{\text{Co}}_{\text{alloy}} - \Delta\varepsilon^{\text{Pt}}_{\text{alloy}} \\ &+ \sum_{Z=5,7,8,9} (x_Z^{\text{Co}}\Delta\varepsilon^{\text{Co}}_{\text{site}} - x_Z^{\text{Pt}}\Delta\varepsilon^{\text{Pt}}_{\text{site}})\frac{N_Z}{N_{tot}}(Z-12)\end{aligned} \tag{4.9}$$

This equation simplifies for a completely disordered alloy, or for a perfect $L1_0$ system if one averages Co and Pt centered clusters (as it is done here), since in these cases $x_Z^a = 1$. One is then able to draw a diagram of this analytical law and to compare the resulting curve with the values obtained by averaging respectively all the Pt and Co LDOS in ordered clusters of different sizes. This is plotted in Fig. 4.4, in which we can see that bulk values are definitely reached around 2000 atoms (or in term of diameter as used in Fig. 4.4, $N^{\frac{1}{3}} \approx 12$). The presented analytical model is based on approximations implying that only d-band shifts of the surface atoms are modified and where only prefactors are fitted to local values. Therefore an overall quantitative agreement with the values resulting from the LDOS averaging cannot be expected as it would be the case of an actual fit of these values.

It is worth noticing that there is no basis to consider the increase of diagonal disorder parameter with the cluster size a general rule. Indeed the sign of the Z-dependent term in the equation 4.9 is driven by the difference $\Delta\varepsilon_{\text{site}}^{\text{Co}} - \Delta\varepsilon_{\text{site}}^{\text{Pt}}$, which depends on the system under study, and can be deduced for any nanoalloy from the simple calculation of this dependence for both pure components. Finally a similar equation can be used to describe the n-dependence of the *off-diagonal disorder* parameter, replacing δ_d by δ_{nd} and ε^a by W^a, the variation of which will also depend on the nature of the alloy through the sign of $\Delta W_{\text{site}}^{\text{Co}} - \Delta W_{\text{site}}^{\text{Pt}}$.

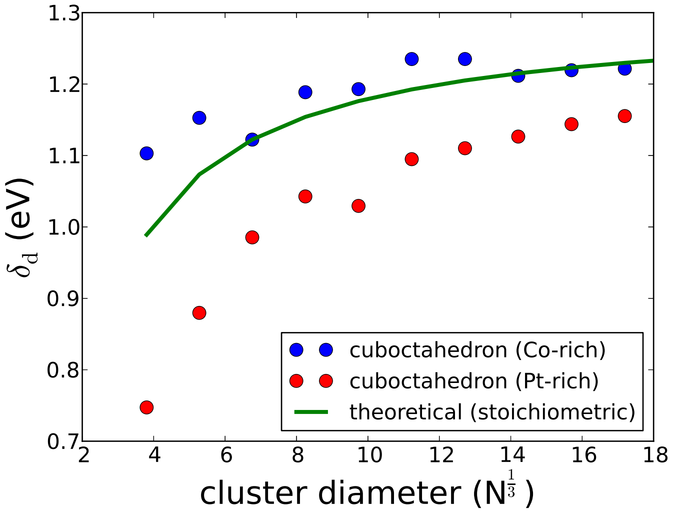

Figure 4.7: Variation of the *diagonal disorder* parameter in nanoalloys, δ_d^n, as a function of $N^{\frac{1}{3}}$ (representative of the diameter of a cluster containing N atoms). The continuous line represents the theoretical values given by equation (4.9). Red and blue circles represent values deduced from averaged LDOS respectively for the so-called Pt rich and Co rich ordered cuboctahedral clusters (see Fig. 4.5).

Once the behavior of the two main parameters $(\delta_d^n, \delta_{nd}^n)$ which drive the electronic structure of a nanoalloy of size n is known, let us show how the mapping previously derived to predict ordering tendency for bulk alloys [37] can be extended to the case of nanoalloys. A relevant way to visualize the alloying effects in clusters *vs* bulk effects is to build a mapping of ordering and demixing domains in the parameter space spanned by δ_{nd} and d-band electronic filling N_e for different values of δ_d and for the concentration of interest, here $c = 0.5$. Results are presented in Fig. 4.4. Contrary to Ref. [37], here we focus on a single set of values corresponding to an average value of d-bandwidth related to CoPt and equal to 6 eV. The most significant effect is that for $\delta_d = 2.0$ eV (black curve) only one large and centered domain appears meaning in particular that the corresponding alloys with $N_e > 8$ and $N_e < 2$ should show strictly demixing tendency. However reducing δ_d to at least 1.0 eV reveals new ordering domains at higher electronic filling allowing again order tendency for late transition metal alloys. It remains to introduce the cluster points in this bulk map, by postulating that it can be done by just moving the bulk point according to the values of $\delta_d^n, \delta_{nd}^n$ issued from the previous laws. In addition, consistently with the charge neutrality rule, these points will be always positioned at the electronic filling of $N_e = 8.5$ characteristic of CoPt at equiconcentration. In order to cover both possible size and morphological effects we have considered two limiting sizes (147 and 2869 atoms) and two morphologies adding icosahedra to the previously investigated cuboctahedra. As can be seen from the the corresponding specific points in Fig. 4.4, all the systems fall at the frontier of the upper ordering domains.

A general behavior of the evolution of electronic structure in CoPt nanoalloys can be tentatively deduced from these results. Actually, a global evolution is obtained when going from bulk alloy to clusters with a large decrease of the absolute value of *off-diagonal disorder*. Further decrease of *diagonal disorder* is found when decreasing the size of the clusters from 2869 atoms to 147 atoms. Since icosahedral and cuboctahedral shapes are leading to similar results it can be concluded that the structure has a weak effect on the ordering tendency. It is also worth noticing that even though the points are not falling directly in the upper ordering domains their displacements as a function of size strictly follows the shift towards lower absolute values of δ_{nd}, indicating that order tendency does not change for any CoPt nanoalloy. The possible role of magnetism was not yet invoked although, as recently proposed by S. Karoui and coworkers [30], in a spin polarized description of the CoPt LDOS, the majority spin up band is completely full and does not participate to the cohesion of the alloy so that an effective average electronic filling of 6.6 d electrons should be attributed to CoPt systems. In this case all the points of Fig. 4.4 would be shifted down into the larger ordering domains, meaning that once again the bulk ordering tendency is not only preserved but even enhanced in the cluster.

4.5 Conclusions

In summary, the presented methodology has been shown to be an accurate way to describe and predict the main local characteristics of nanoalloys, namely their mixing behavior and the redistribution of the energy electronic states from the single knowledge of the electronic structure of their pure constituents, using a self-consistent TB approach in the direct space. Local effects can be quantified through linear laws as a function of the site coordination, by disentangling structural and chemical effects. Such a methodology is extendable to any other alloy since it has been shown to give a unified description of the local electronic structure both at surfaces of pure materials and in pure bulk alloys. Thus, analytic laws have been derived which yield on one hand the variation of both the d atomic level and the effective d bandwidth and on the other hand, the variation of *diagonal* and *off-diagonal disorder* parameters, as a function of the cluster size. The ordering trends in nanoalloys can then be estimated from the bulk stability maps by just shifting the corresponding $(\delta_{\mathrm{d}}, \delta_{\mathrm{nd}})$ points according to these analytic laws. This method has no limit neither in the size, nor in the structural asymmetric features, allowing the presence of surfaces, low coordinates sites, defects like vacancies or stacking faults. Of course the method would deserve some improve-

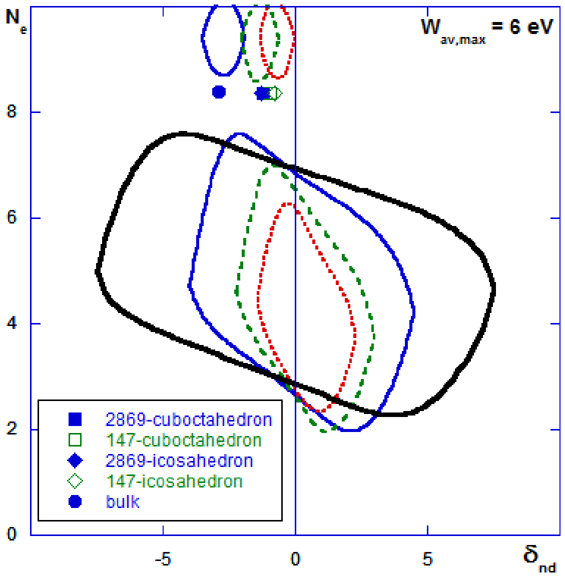

Figure 4.8: (N_e, δ_{nd}) ordering domains represented in the parameter space spanned by δ_{nd} and N_e for different values of δ_d and for alloys at equiconcentration. Ordering domains are delimited by black, blue, dotted green and dotted red lines corresponding respectively to $\delta_d = 2.0, 1.0, 0.5, 0.25$ eV, the area outside these domains corresponding to demixing tendency. This plot is related to an average bandwidth of pure constituents of $W_{\mathrm{av,max}} = 6.0$ eV. The points correspond to bulk and 2869 and 147 atoms clusters.

ments like an explicit introduction of magnetism and also the elastic effects through an explicit distance dependence of the parameters.

CHAPTER 5

General conclusions and perspectives

This work proposed an accurate way to predict the characteristics of realistic-size nanoalloys (mixing behavior, redistribution of electronic states) by means of the self-consistent Tight Binding approach supported by the *ab initio* Density Functional Theory calculations. Since DFT is a method applicable only to relatively small systems it is used for comparison and to verify the correctness of the local neutrality assumption. The local neutrality assumption is applied later as a self-consistency rule in systematic TBA calculations of larger and more complex systems inaccessible directly by DFT. The subject of the analysis was mainly the local electronic structure on various inequivalent sites systematically classified in terms of their local environment (site occupation, coordination number and mixing rank). This methodology has been verified and successfully applied in the case of CoPt system and is extendable to other binary systems without actual size limitations related to numerical complexity of calculations. Even in its simplest form the model showed its usefulness.

After extensive discussion of DFT and TBA approaches, both in terms of their theoretical foundations and practical application, the work was focused on DFT results of Co and Pt elemental systems. We hawe calculated a set of basic structural and energetic properties (lattice constants, c/a ratio of hexagonal structure, magnetic moments, bulk moduli, surface energies and energetics of small clusters) that showed an overall reasonable agreement with the literature and this allowed to conclude on general validity of the method within the chosen parametrization. The local neutrality rule in the case of low-coordinated sites in pure metallic systems (pure surfaces and single - component clusters) was also verified which allowed to get more insight into the effect of site coordination on the local electronic structure separately from the alloying effects. These effects were taken into account in the subsequent analysis of DFT calculations of mixed Co-Pt systems where the charge transfers between orbitals of the two atom species was carefully studied both inside the bulk with only concentration-dependent chemical effect related to the mixing rank of the site and in more intricate cases of surfaces and small clusters where the effects of the site coordination and chemical environment are combined. On the overall study a local neutrality has been obtained per site, species and orbital. Some limitations of the strict generality were also identified, namely a slight charge transfer between the spin orientations related to the changes of magnetic moment and deviation from neutrality in diluted CoPt systems. In the case of platinum admixture the charge redistribution exceeds the tolerance level. However, for most cases and concentrated alloys, the most interesting for applications, neutrality rule is a valid assumption and can be applied in further TBA calculations. Basic properties of mixed CoPt systems were also studied and the comparison with the experimental values in case of $L1_0$ CoPt showed a very good agreement in terms of lattice constants, bulk modulus and magnetic moments. A very interesting observation could be made for the formation energies of ordered alloys ($L1_0$ and $L1_2$ phases). In ferromagnetic calculations this formation energy is always negative which means that the system exhibits a preference for ordering contrary to the paramagnetic case where the formation energy is found slightly positive. A systematic analysis of the heats of formation with respect to concentration allows to conclude that ordered phases are stabilized by magnetic effects with regard to paramagnetic configurations showing much higher energies of formation. This is consistent with the results available in the literature [30].

The TBA calculations were performed first for a number of selected simple structures in order to compare the results with DFT calculations (pure fcc bulk, $L1_0$ CoPt, dilute systems and Co monolayer on Pt(111)). These preliminary TBA results showed a good qualitative agreement of the LDOS (in terms of shape, band width and position of the center of gravity) with the DFT results at least for concentrated systems (diluted systems deviated from the range of application of the neutrality rule). The comparison between the DFT and TBA was then extended to a small typical cuboctahedral cluster of CoPt with an $L1_0$-ordered arrangement and a very reasonable agreement was found while superimposing the average DOS of Co and Pt. This agreement between the results obtained by means of the two methods justified the extension of the analysis upon more realistic cluster sizes (from few tens to several thousands of atoms) and configurations inaccessible directly by *ab initio* approaches. Only a few model configurations were considered including pure and $L1_0$-ordered mixed cuboctahedral clusters. LDOS on sites with different chemical environment and coordination numbers were analyzed in detail. Systematic analysis of those changes as a function of site coordination evidenced linear variation law of d-band center and d-band width. Linear fits were performed for given size and configuration variant and the same analysis was performed for Co d-band with analogous conclusions regarding the linearity of the trends. It is worth noticing that the observed trends do not change with the variation of cluster size within the considered range of sizes. An interesting feature is also the fact that the observed linear trends are universal (in terms of the slope) for both mixed and pure clusters (the latter being simply vertically shifted) which effectively allows to decouple the effects of the alloying (chemical environment) and the effects related to the geometry (site coordination). Since the slope of the linear trend is preserved the effect of the cluster size contributes only to the rigid vertical shift of the observed trends allowing to predict an average atomic d-level given the cluster size. These observations prove that the basic features of LDOS (d-band center and d-band width) can be predicted by simple laws on the basis of two terms: a structural term represented by the linear function of the site coordination and a chemical term as a rigid shift.

Following the previous work on ordering trends in the transition metal alloys [37] the present Thesis proposes a new way to predict the ordering tendency for any transition metal nanoalloy as a function of its size. The prediction is grounded on the basic properties of DOS either directly calculated in the TBA framework for given structure or estimated with linear laws. Once the behavior of these two main DOS parameters that drive the electronic structure of a nanoalloy of size n is known, it is possible to create a map of ordering regions. All clusters were therefore analyzed within this parametrization and the results are summarized in the form of a two-dimensional map spanned over the disorder parameter space. One can observe the sensitivity of the parameters with respect to the cluster size, shape (we introduced icosahedra in this case as they were not studied previously in such detail as the cuboctahedra) and stoichiometry variant (Co- or Pt-rich clusters) as well as the evolution of the cluster location on the map. Using the data available in the literature one can determine ordering domains and predict the ordering preference of a cluster solely by considering its location on the map.

Perspectives

The TBA scheme of calculations can be further extended by the inclusion of colinear spin magnetism. At the absence of the spin-orbital coupling the spin up and spin down electron populations can be treated separately within a single Fermi level E_F for both spin variants. The spin-wise LDOS can be obtained by shifting the center of mass of the paramagnetic LDOS. For small shifts the magnetic moment introduced in this way will be proportional to this shift and the value of the paramagnetic density of states at E_F. Considerations of the competition between the potential and kinetic energies with respect to the disproportion of spin populations leads to the Stoner criterion which states that such a shift can be energetically favorable in systems with narrow bands and large density of states at E_F. This allows to predict ferromagnetic behavior solely from non-magnetic calculations. It is also possible to find the self-consistency relation necessary to determine these shifts, see [155] for discussion. Another extension would be to account for the variation of β integrals with respect to the changes of interatomic distances r_{ij} which can be done by introducing the effective distance-dependant hopping integral:

$$\beta_{ij}^{\lambda\mu} = \beta_0^{\lambda\mu} e^{-q\left(\frac{r_{ij}}{r_0}-1\right)} \tag{5.1}$$

where β_0 is the previously considered hopping integral and r_0 is the nearest-neighbor distance. In this framework a more explicit repulsive contribution to the total energy could also be added. In terms of the *ab initio* calculations the increasing computing performance of modern computers allows to perform more systematic studies and to carry out accurate calculations for previously inaccessible systems. However, the tight-binding formalism remains a fundamental framework for understanding the physics of the alloy systems more profoundly on the basis of the knowledge of simple parameters like the diagonal and non-diagonal ones or the electronic filling of bands.

Bibliography

[1] A. Jaafar. Ph.D. thesis (2010).

[2] S. Dennler. Ph.D. thesis (2004).

[3] C. Kittel. *Introduction to Solid State Physics.* John Wiley & Sons (1996).

[4] G. Y. Guo and H. H. Wang. *Gradient-Corrected Density Functional Calculation of Elastic Constants of Fe, Co and Ni in bcc, fcc and hcp Structures.* Chinese Journal Of Physics, **38**(949) (2000).

[5] B. Strauss, F. Frey, W. Petry, J. Trampenau, K. Nicolaus, S. M. Shapiro and J. Bossy. *Martensitic phase transformation and lattice dynamics of fcc cobalt.* Physical Review B (Condensed Matter), **54** 6035–6038 (1996).

[6] J. Crangle. *LIX. The magnetic moments of cobalt-copper alloys.* Philosophical Magazine, **46**(376) 499–513 (1955).

[7] R. Wyckoff. *Crystal Structures, t. 1* (1963).

[8] C. Leroux, M. C. Cadeville, V. Pierron-Bohnes, G. Inden and F. Hinz. *Comparative investigation of structural and transport properties of L10 NiPt and CoPt phases; the role of magnetism.* Journal of Physics F: Metal Physics, **18** 2033–2051 (1988).

[9] R. M. Martin. *Electronic Structure: Basic Theory and Practical Methods.* Cambridge University Press (2004).

[10] E. Artacho, J. D. Gale, A. Garcia, J. Junquera, R. M. Martin, P. Ordejon, D. Sanchez-Portal and J. M. Soler. *SIESTA 2.0.2 User's Guide* (2008).

[11] E. Lundgren, B. Stanka, M. Schmid and P. Varga. *Thin films of Co on Pt(111): Strain relaxation and growth.* Physical Review B, **62** 2843–2851 (2000).

[12] M. H. Kryder. *Magnetic recording beyond the superparamagnetic limit.* In *IEEE International Magnetics Conference*, page 575. Seagate Research (2000).

[13] T. Miyazaki, O. Kitakami, S. Okamoto, Y. Shimada, Z. Akase, Y. Murakami, D. Shindo, Y. Takahashi and K. Hono. *Size effect on the ordering of L10 FePt nanoparticles.* Physical Review B, **72**(14) 144419 (2005).

[14] D. Alloyeau, C. Ricolleau, C. Mottet, T. Oikawa, C. Langlois, Y. Le Bouar, N. Braidy and A. Loiseau. *Size and shape effects on the order–disorder phase transition in CoPt nanoparticles.* Nature Materials, **8** 940–946 (2009).

[15] M. Watanabe. chapter New CO-tolerant catalyst concepts, page 408. Wiley (2010).

[16] U. A. Paulus, A. Wokaun, G. G. Scherer, T. J. Schmidt, V. Stamenkovic, V. Radmilovic, N. M. Markovic and P. N. Ross. *Oxygen Reduction on Carbon-Supported Pt-Ni and Pt-Co Alloy Catalysts.* The Journal of Physical Chemistry B, **106**(16) 4181–4191 (2002).

[17] N. Chi, K.-Y. Chan and D. L. Phillips. *Electrocatalytic oxidation of formic acid by Pt/Co nanoparticles.* Catalysis Letters, **71**(1/2) 21–26 (2001).

[18] V. S. Murthi, R. C. Urian and S. Mukerjee. *Oxygen Reduction Kinetics in Low and Medium Temperature Acid Environment: Correlation of Water Activation and Surface Properties in Supported Pt and Pt Alloy Electrocatalysts.* The Journal of Physical Chemistry B, **108**(30) 11011–11023 (2004).

[19] H. R. Colon-Mercado and B. N. Popov. *Stability of platinum based alloy cathode catalysts in PEM fuel cells.* Journal of Power Sources, **155**(2) 253–263 (2006).

[20] K. J. J. Mayrhofer, B. B. Blizanac, M. Arenz, V. R. Stamenkovic, P. N. Ross and N. M. Markovic. *The Impact of Geometric and Surface Electronic Properties of Pt-Catalysts on the Particle Size Effect in Electrocatalysis.* The Journal of Physical Chemistry B, **109**(30) 14433–14440 (2005).

[21] V. Stamenkovic, B. S. Mun, K. J. J. Mayrhofer, P. N. Ross, N. M. Markovic, J. Rossmeisl, J. Greeley and J. K. Norskov. *Changing the Activity of Electrocatalysts for Oxygen Reduction by Tuning the Surface Electronic Structure.* Angewandte Chemie, **118**(18) 2963–2967 (2006).

[22] F. Tournus, K. Sato, T. Epicier, T. J. Konno and V. Dupuis. *Multi-L10 Domain CoPt and FePt Nanoparticles Revealed by Electron Microscopy.* Physical Review Letters, **110**(5) (2013).

[23] J.-I. Park and J. Cheon. *Synthesis of Solid Solution and Core-Shell Type Cobalt-Platinum Magnetic Nanoparticles via Transmetalation Reactions.* Journal of the American Chemical Society, **123**(24) 5743–5746 (2001).

[24] T. O. Ely, C. Pan, C. Amiens, B. Chaudret, F. Dassenoy, P. Lecante, M.-J. Casanove, A. Mosset, M. Respaud and J.-M. Broto. *Nanoscale Bimetallic CoxPt1-x Particles Dispersed in Poly(vinylpyrrolidone): Synthesis from Organometallic Precursors and Characterization.* The Journal of Physical Chemistry B, **104**(4) 695–702 (2000).

[25] L. Castaldi, K. Giannakopoulos, A. Travlos, D. Niarchos, S. Boukari and E. Beaurepaire. *Superparamagnetic and ferromagnetic CoPt nanoparticles deposited on silicon dioxide.* Journal of Physics: Conference Series, **10**(1) 155 (2005).

[26] C. J. O'Connor, J. A. Sims, A. Kumbhar, V. L. Kolesnichenko, W. L. Zhou and J. A. Wiemann. *Magnetic properties of FePtx/Au and CoPtx/Au core-shell nanoparticles.* Journal of Magnetism and Magnetic Materials, **226**(2) 1915–1917 (2001).

[27] X. Sun, Z. Y. Jia, Y. H. Huang, J. W. Harrell, D. E. Nikles, K. Sun and L. M. Wang. *Synthesis and magnetic properties of CoPt nanoparticles.* Journal of Applied Physics, **95**(11) 6747–6749 (2004).

[28] J.-I. Park, M. G. Kim, Y.-w. Jun, J. S. Lee, W.-r. Lee and J. Cheon. *Characterization of Superparamagnetic Core-Shell Nanoparticles and Monitoring Their Anisotropic Phase Transition to Ferromagnetic "Solid Solution" Nanoalloys.* Journal of the American Chemical Society, **126**(29) 9072–9078 (2004).

[29] H. Ebert, S. Bornemann, J. Minár, P. H. Dederichs, R. Zeller and I. Cabria. *Magnetic properties of Co- and FePt-clusters.* Computational Materials Science, **35**(3) 279–282 (2006).

[30] S. Karoui, H. Amara, B. Legrand and F. Ducastelle. *Magnetism: the driving force of order in CoPt, a first-principles study.* Journal of Physics: Condensed Matter, **25**(5) 6005 (2013).

[31] A. Jaafar, C. Goyhenex and G. Tréglia. *Role of sp–d hybridization in the formation of stacking defects at metal surfaces.* Surface Science, **602** 2681–2688 (2008).

[32] S. Sawaya, J. Goniakowski, C. Mottet, A. Saúl and G. Tréglia. *Charge redistribution at Pd surfaces: Ab initio grounds for tight-binding interatomic potentials.* Physical Review B (Condensed Matter), **56** 74081–12166 (1997).

[33] A. Jaafar, C. Goyhenex and G. Tréglia. *Rules for tight-binding calculations in bi-metallic compounds based on density functional theory: the case of Co-Au.* J Phys Condens Matter, **22**(50) 505503 (2010).

[34] J. M. Soler, E. Artacho, J. D. Gale, A. García, J. Junquera, P. Ordejón and D. Sánchez-Portal. *The SIESTA method for ab initio order-N materials simulation.* Journal of Physics: Condensed Matter, **14** 2745–2779 (2002).

[35] J. P. Perdew, K. Burke and M. Ernzerhof. *Generalized Gradient Approximation Made Simple.* Physical Review Letters, **77** 3865–3868 (1996).

[36] R. Haydock, V. Heine and M. J. Kelly. *Electronic structure based on the local atomic environment for tight-binding bands. II.* Journal of Physics C: Solid State Physics, **8** 2591–2605 (1975).

[37] J. Los, C. Mottet, G. Tréglia and C. Goyhenex. *Ordering trends in transition metal alloys from tight-binding electronic structure calculations.* Physical Review B, **84** (2011).

[38] M. Born and R. Oppenheimer. *Zur Quantentheorie der Molekeln.* Ann. Phys. (Leipzig), **84**(20) 457 (1927).

[39] R. J. Bartlett and J. F. Stanton. *Applications of Post-Hartree-Fock Methods: A Tutorial.* Reviews in Computational Chemistry, **5** 65 (1994).

[40] P. Hohenberg and W. Kohn. *Inhomogeneous Electron Gas.* Physical Review, **136** 864–871 (1964).

[41] M. Levy. *Electron densities in search of Hamiltonians.* Physical Review A (General Physics), **26** 1200–1208 (1982).

[42] E. H. Lieb. *Density functionals for coulomb systems.* International Journal of Quantum Chemistry, **24**(3) 243–277 (1983).

[43] J. P. Perdew and K. Schmidt. *Jacob's ladder of density functional approximations for the exchange-correlation energy.* AIP Conference Proceedings, **577** 1 (2001).

[44] W. Kohn and L. J. Sham. *Self-Consistent Equations Including Exchange and Correlation Effects.* Physical Review, **140** 1133–1138 (1965).

[45] E. Wigner. *On the Interaction of Electrons in Metals.* Physical Review, **46** 1002–1011 (1934).

[46] D. M. Ceperley and B. J. Alder. *Ground State of the Electron Gas by a Stochastic Method.* Physical Review Letters, **45** 566–569 (1980).

[47] S. H. Vosko, L. Wilk and M. Nusair. *Accurate spin-dependent electron liquid correlation energies for local spin density calculations: a critical analysis.* Canadian Journal of Physics, **58** 1200 (1980).

[48] J. P. Perdew and A. Zunger. *Self-interaction correction to density-functional approximations for many-electron systems.* Physical Review B (Condensed Matter), **23** 5048–5079 (1981).

[49] F. Herman, J. P. van Dyke and I. B. Ortenburger. *Improved Statistical Exchange Approximation for Inhomogeneous Many-Electron Systems.* Physical Review Letters, **22** 807–811 (1969).

[50] P. S. Svendsen and U. von Barth. *Gradient expansion of the exchange energy from second-order density response theory.* Physical Review B (Condensed Matter), **54** 95234–17413 (1996).

[51] A. D. Becke. *Density-functional exchange-energy approximation with correct asymptotic behavior.* Physical Review A (General Physics), **38** 3098–3100 (1988).

[52] J. P. Perdew, J. A. Chevary, S. H. Vosko, K. A. Jackson, M. R. Pederson, D. J. Singh and C. Fiolhais. *Atoms, molecules, solids, and surfaces: Applications of the generalized gradient approximation for exchange and correlation.* Physical Review B (Condensed Matter), **46** 6671–6687 (1992).

[53] C. Lee, W. Yang and R. G. Parr. *Development of the Colle-Salvetti correlation-energy formula into a functional of the electron density.* Physical Review B (Condensed Matter), **37** 785–789 (1988).

[54] E. H. Lieb and S. Oxford. *Improved lower bound on the indirect Coulomb energy.* International Journal of Quantum Chemistry, **19**(3) 427–439 (1981).

[55] S.-K. Ma and K. A. Brueckner. *Correlation Energy of an Electron Gas with a Slowly Varying High Density.* Physical Review, **165** 18–31 (1968).

[56] L. Kleinman and T. Tamura. *Ma-Brueckner correlation energy.* Physical Review B (Condensed Matter), **40** 4191–4193 (1989).

[57] J. P. Perdew and K. Burke. *Comparison shopping for a gradient-corrected density functional.* International Journal of Quantum Chemistry, **57**(3) 309–319 (1996).

[58] D. Rappoport, N. R. M. Crawford, F. Furche and K. Burke. chapter Approximate Density Functionals: Which Should I Choose? John Wiley & Sons, Ltd (2009).

[59] M. E. Gruner. *Antiferromagnetism and segregation in cuboctahedral FePt nanoparticles.* Journal of Physics D: Applied Physics, **41** 4015 (2008).

[60] M. Ernst Gruner. *Core-shell morphologies of FePt and CoPt nanoparticles: An ab initio comparison.* Journal of Physics: Conference Series, **200** 2039 (2010).

[61] M. E. Gruner, G. Rollmann, P. Entel and M. Farle. *Multiply Twinned Morphologies of FePt and CoPt Nanoparticles.* Physical Review Letters, **100** 87203 (2008).

[62] C. J. Cramer and D. G. Truhlar. *Density functional theory for transition metals and transition metal chemistry.* Physical chemistry chemical physics : PCCP, **11**(46) 10757–10816 (2009).

[63] J. Paier, M. Marsman and G. Kresse. *Why does the B3LYP hybrid functional fail for metals?* The Journal of chemical physics, **127**(2) 024103 (2007).

[64] Z. Szekeres, P. Mezey and P. Surjan. *Diagonalization-free initial guess to SCF calculations for large molecules.* Chemical Physics Letters, **424** 420–424 (2006).

[65] A. R. Leach. *Molecular Modelling: Principles and Applications.* Pearson Prentice Hall (2001).

[66] C. G. Broyden. *A class of methods for solving nonlinear simultaneous equations.* Mathematics of Computation, **19**(92) 577–577 (1965).

[67] G. P. Srivastava. *Broyden's method for self-consistent field convergence acceleration.* Journal of Physics A: Mathematical and General, **17** L317–L321 (1984).

[68] P. Pulay. *Convergence acceleration of iterative sequences. the case of scf iteration.* Chemical Physics Letters, **73** 393–398 (1980).

[69] J. Junquera. *Efficient density-functional calculations with atomic orbitals: a hands-on course on the SIESTA code* (2007).

[70] D. R. Hamann, M. Schlüter and C. Chiang. *Norm-Conserving Pseudopotentials.* Physical Review Letters, **43** 1494–1497 (1979).

[71] G. B. Bachelet, D. R. Hamann and M. Schlüter. *Pseudopotentials that work: From H to Pu.* Physical Review B (Condensed Matter), **26** 4199–4228 (1982).

[72] D. Vanderbilt. *Optimally smooth norm-conserving pseudopotentials.* Physical Review B (Condensed Matter), **32** 8412–8415 (1985).

[73] P. A. Christiansen, Y. S. Lee and K. S. Pitzer. *Improved ab initio effective core potentials for molecular calculations.* Journal of Chemical Physics, **71** 4445–4450 (1979).

[74] G. P. Kerker. *Non-singular atomic pseudopotentials for solid state applications.* Journal of Physics C: Solid State Physics, **13** L189–L194 (1980).

[75] N. Troullier and J. L. Martins. *Efficient pseudopotentials for plane-wave calculations.* Physical Review B (Condensed Matter), **43** 1993–2006 (1991).

[76] S. Goedecker, M. Teter and J. Hutter. *Separable dual-space Gaussian pseudopotentials.* Physical Review B (Condensed Matter), **54** 1703–1710 (1996).

[77] A. Postnikov. *Siesta caminando.* `http://www.home.uni-osnabrueck.de/apostnik/Lectures/SIESTA-tuto.pdf`.

[78] L. Kleinman and D. M. Bylander. *Efficacious Form for Model Pseudopotentials.* Physical Review Letters, **48** 1425–1428 (1982).

[79] A. Garcia. *ATOM User Manual.* `http://fisica.ehu.es/ag/siesta-extra/atom.pdf`.

[80] F. D. Murnaghan. *The Compressibility of Media under Extreme Pressures.* Proceedings of the National Academy of Sciences of the United States of America, **30** 244–247 (1944).

[81] F. Birch. *Finite Elastic Strain of Cubic Crystals.* Physical Review, **71** 809–824 (1947).

[82] R. Bujakiewicz-Koroska and Y. Natanzon. *First Principles Calculations Of Elastic Constants For Defected Na1/2Bi1/2TiO3.* Integrated Ferroelectrics, **108**(1) 21–36 (2009).

[83] J. Meister and W. H. E. Schwarz. *Principal Components of Ionicity.* The Journal of Physical Chemistry, **98**(33) 8245–8252 (1994).

[84] R. S. Mulliken. *Electronic Population Analysis on LCAO[Single Bond]MO Molecular Wave Functions. I.* The Journal of Chemical Physics, **23**(10) 1833–1840 (1955).

[85] R. F. W. Bader. *Atoms in Molecules - A Quantum Theory.* Oxford (1990).

[86] G. Henkelman, A. Arnaldsson and H. Jónsson. *A fast and robust algorithm for Bader decomposition of charge density.* Computational Materials Science, **36** 354–360 (2006).

[87] E. Sanville, S. D. Kenny, R. Smith and G. Henkelman. *Improved grid-based algorithm for Bader charge allocation.* Journal of Computational Chemistry, **28** 899–908 (2007).

[88] W. Tang, E. Sanville and G. Henkelman. *A grid-based Bader analysis algorithm without lattice bias.* Journal of Physics: Condensed Matter, **21** 4204 (2009).

[89] R. P. Feynman. *Forces in Molecules.* Physical Review B, **56**(4) 340–343 (1939).

[90] P. Pulay. *Ab initio calculation of force constants and equilibrium geometries in polyatomic molecules.* Molecular Physics, **17**(2) 197–204 (1969).

[91] J. Moreno and J. M. Soler. *Optimal meshes for integrals in real- and reciprocal-space unit cells.* Physical Review B (Condensed Matter), **45** 80017–13898 (1992).

[92] D. D. Johnson. *Modified Broyden's method for accelerating convergence in self-consistent calculations.* Physical Review B (Condensed Matter), **38** 75783–12813 (1988).

[93] F. Bloch. Ph.D. thesis (1928).

[94] H. Jones, N. F. Mott and H. W. Skinner. *A Theory of the Form of the X-Ray Emission Bands of Metals.* Physical Review, **45** 379–384 (1934).

[95] J. C. Slater and G. F. Koster. *Simplified LCAO Method for the Periodic Potential Problem.* Physical Review, **94** 1498 (1954).

[96] D. A. Papaconstantopoulos and M. J. Mehl. *The Slater Koster tight-binding method: a computationally efficient and accurate approach.* Journal of Physics: Condensed Matter, **15** 413 (2003).

[97] F. Ducastelle. *Modules élastiques des métaux de transition.* J. Physique, **31** 1055 (1970).

[98] F. Cyrot-Lackmann and F. Ducastelle. *Self-Consistent Theory of Clusters in Disordered Alloys.* Physical Review Letters, **27** 429–431 (1971).

[99] J. P. Gaspard and F. Cyrot-Lackmann. *Density of states from moments. Application to the impurity band.* Journal of Physics C: Solid State Physics, **6** 3077–3096 (1973).

[100] V. John, I. Angelov, A. A. Öncül and D. Thévenin. *Techniques for the reconstruction of a distribution from a finite number of its moments.* Chemical Engineering Science, **62**(11) 2890–2904 (2007).

[101] L. G. M. de Souza, G. Janiga, V. John and D. Thévenin. *Reconstruction of a distribution from a finite number of moments with an adaptive spline-based algorithm.* Chemical Engineering Science, **65**(9) 2741–2750 (2010).

[102] D. A. Papaconstantopoulos. *Handbook of Electronic Structure of elemental Solids.* Plenum (1986).

[103] H. Shiba. *A Reformulation of the Coherent Potential Approximation and Its Applications.* Progress of Theoretical Physics, **46** 77–94 (1971).

[104] F. Bechstedt, D. Reichardt and R. Enderlein. *Self-Consistent Tight-Binding Method for Total Energy Calculations of Tetrahedral Semiconductors Including Surfaces and Defects.* Physica status solidi (B), **131** 643–657 (1985).

[105] W. A. Harrison and J. Tersoff. *Tight-binding theory of heterojunction band lineups and interface dipoles.* Journal of Vacuum Science & Technology B: Microelectronics and Nanometer Structures, **4** 1068–1073 (1986).

[106] J. A. Majewski and P. Vogl. *Simple model for structural properties and crystal stability of sp-bonded solids.* Physical Review B (Condensed Matter), **35** 9666–9682 (1987).

[107] O. L. Alerhand and E. J. Mele. *Surface reconstruction and vibrational excitations of Si(001).* Physical Review B (Condensed Matter), **35** 5533–5546 (1987).

[108] H. L. Skriver and N. M. Rosengaard. *Self-consistent Green's-function technique for surfaces and interfaces.* Physical Review B (Condensed Matter), **43** 9538–9549 (1991).

[109] M.-H. Tsai, O. F. Sankey and J. D. Dow. *Charge transfer in ab initio real-space molecular dynamics.* Physical Review B (Condensed Matter), **46** 66660–10467 (1992).

[110] A. A. Demkov, J. Ortega, O. F. Sankey and M. P. Grumbach. *Electronic structure approach for complex silicas.* Physical Review B (Condensed Matter), **52** 1618–1630 (1995).

[111] M. Elstner, D. Porezag, G. Jungnickel, J. Elsner, M. Haugk, T. Frauenheim, S. Suhai and G. Seifert. *Self-consistent-charge density-functional tight-binding method for simulations of complex materials properties.* Physical Review B, **58** 7260–7268 (1998).

[112] C. Goyhenex. *Revised tight-binding second moment potential for transition metal surfaces.* Surface Science, **606** 325–328 (2012).

[113] V. Rosato, M. Guillope and B. Legrand. *Thermodynamical and structural properties of f.c.c. transition metals using a simple tight-binding model.* Philosophical Magazine A, **59** 321–336 (1989).

[114] G. Allan and M. Lannoo. *Vacancies in transition metals Formation energy and formation volume.* Journal of Physics and Chemistry of Solids, **37**(7) 699–709 (1976).

[115] P. H. Citrin, G. K. Wertheim and Y. Baer. *Core-Level Binding Energy and Density of States from the Surface Atoms of Gold.* Physical Review Letters, **41** 1425–1428 (1978).

[116] D. Spanjaard. *Surface core level spectroscopy of transition metals: A new tool for the determination of their surface structure.* Surface Science Reports, **5** 1 (1985).

[117] C. Mottet. Ph.D. thesis (1997).

[118] V. N. Staroverov, G. E. Scuseria, J. Tao and J. P. Perdew. *Tests of a ladder of density functionals for bulk solids and surfaces.* Physical Review B, **69** 75102 (2004).

[119] C. S. Wang, B. M. Klein and H. Krakauer. *Theory of magnetic and structural ordering in iron.* Physical Review Letters, **54** 1852–1855 (1985).

[120] G. Guo. *Relativistic effects on the structural and magnetic properties of iron.* Solid State Communications, **79** 121–124 (1991).

[121] M.-C. Desjonquères and D. Spanjaard. *Concepts in Surface Physics.* Springer (1996).

[122] A. R. Miedema, F. R. de Boer, R. Boom, W. C. M. Mattens and A. K. Niessen. *Cohesion in Metals: Transition Metal Alloys.* North Holland (1988).

[123] S. Karoui. Ph.D. thesis (2013).

[124] A. L. Mackay. *A dense non-crystallographic packing of equal spheres.* Acta Crystallographica, **15**(9) 916–918 (1962).

[125] B. Hammer, Y. Morikawa and J. K. Nørskov. *CO Chemisorption at Metal Surfaces and Overlayers.* Physical Review Letters, **76** 2141–2144 (1996).

[126] P. Nava. *Density Functional Theory Calculations on Palladium Clusters and on an AgInS Semiconductor Compound.* Cuvillier Verlag (2005).

[127] A. V. Myshlyavtsev and P. V. Stishenko. *Relative stability of icosahedral and cuboctahedral metallic nanoparticles.* pages 1–7 (2013).

[128] C. E. Dahmani. Ph.D. thesis (1985).

[129] V. Pierron-Bohnes and et al. *to be published.*

[130] K. H. J. Buschow. *Handbook of magnetic materials*, volume 13. Elsevier Science & Technology Books (2001).

[131] W. Grange, I. Galanakis, M. Alouani, M. Maret, J.-P. Kappler and A. Rogalev. *Experimental and theoretical x-ray magnetic-circular-dichroism study of the magnetic properties of Co50Pt50 thin films.* Physical Review B, **62**(2) 1157–1166 (2000).

[132] A. Alam, B. Kraczek and D. D. Johnson. *Structural, magnetic, and defect properties of Co-Pt type magnetic-storage alloys: Density Functional Theory study of thermal processing effects.* Physical Review B, **82**(2) 24435 (2010).

[133] R. V. Chepulskii and S. Curtarolo. *Revealing low-temperature atomic ordering in bulk Co-Pt with the high-throughput ab-initio method.* Applied Physics Letters, **99** 1902 (2011).

[134] R. Hultgren, P. D. Desai, D. T. Hawkins, M. Gleiser and K. K. Kelley. *Selected Values of the Thermodynamic Properties of Binary Alloys.* Wiley (1973).

[135] M. A. Zwijnenburg, C. van Alsenoy and T. Maschmeyer. *Factors Affecting Ionicity in All-Silica Materials: A Density Functional Cluster Study.* The Journal of Physical Chemistry A, **106**(51) 12376–12385 (2002).

[136] U. Pustogowa, J. Zabloudil, C. Uiberacker, C. Blaas, P. Weinberger, L. Szunyogh and C. Sommers. *Magnetic properties of thin films of Co and of (CoPt) superstructures on Pt(100) and Pt(111).* Physical Review B, **60**(1) 414–421 (1999).

[137] E. C. Stoner. *Collective Electron Specific Heat and Spin Paramagnetism in Metals.* Proceedings of the Royal Society A: Mathematical, Physical and Engineering Sciences, **154**(883) 656–678 (1936).

[138] P. Grütter and U. T. Dürig. *Growth of vapor-deposited cobalt films on Pt(111) studied by scanning tunneling microscopy.* Physical Review B (Condensed Matter), **49** 2021–2029 (1994).

[139] S. Ferrer, J. Alvarez, E. Lundgren, X. Torrelles, P. Fajardo and F. Boscherini. *Surface x-ray diffraction from Co/Pt(111) ultrathin films and alloys: Structure and magnetism.* Physical Review B (Condensed Matter), **56** 9848–9857 (1997).

[140] J. S. Tsay and C. S. Shern. *Diffusion and alloy formation of Co ultrathin films on Pt(111).* Journal of Applied Physics, **80** 3777–3781 (1996).

[141] C. Goyhenex and G. Tréglia. *Theoretical determination of two critical sizes for strain relaxation during Co/Pt(111) heteroepitaxy.* Surface Science, **446**(3) 272–282 (2000).

[142] C. Goyhenex, H. Bulou, J. P. Deville and G. Tréglia. *Compressive strain versus tensile strain.* Applied Surface Science, **177**(4) 238–242 (2001).

[143] M. V. Lebedeva, V. Pierron-Bohnes, C. Goyhenex, V. Papaefthimiou, S. Zafeiratos, R. R. Nazmutdinov, V. Da Costa, M. Acosta, L. Zosiak, R. Kozubski, D. Muller and E. R. Savinova. *Effect of the Chemical Order on the Electrocatalytic Activity of Model PtCo Electrodes in the Oxygen Reduction Reaction* (2013).

[144] L. Zosiak, C. Goyhenex, R. Kozubski and G. Tréglia. *Disentangling coordination and alloy effects in transition-metal nanoalloys from their electronic structure.* Physical Review B, **88**(1) (2013).

[145] F. Ducastelle. *Order and Phase Stability in Alloys* (1991).

[146] C. Goyhenex and G. Tréglia. *Unified picture of d-band and core-level shifts in transition metal alloys.* Physical Review B, **83** (2011).

[147] J. M. Sanchez, J. L. Moran-Lopez, C. Leroux and M. C. Cadeville. *Magnetic properties and chemical ordering in Co-Pt.* Journal of Physics C: Solid State Physics, **21**(33) L1091–L1096 (1988).

[148] A. Bieber, F. Ducastelle, F. Gautier, G. Tréglia and P. Turchi. *Electronic structure and relative stabilities of L12 and D022 ordered structures occuring in transition metal alloys.* Solid State Communications, **45**(7) 585–590 (1983).

[149] R. J. Cole, N. J. Brooks and P. Weightman. *Determination of charge transfer in the CuxPd1-x alloy system.* Physical Review B (Condensed Matter), **56** 1185676–1112182 (1997).

[150] P. A. Korzhavyi, A. V. Ruban, I. A. Abrikosov and H. L. Skriver. *Madelung energy for random metallic alloys in the coherent potential approximation.* Physical Review B (Condensed Matter), **51** 5773–5780 (1995).

[151] Y. S. Lee, J. Y. Rhee, C. N. Whang and Y. P. Lee. *Electronic structure of Co-Pt alloys: X-ray spectroscopy and density-functional calculations.* Physical Review B, **68** 235111 (2003).

[152] C. Mottet, G. Tréglia and B. Legrand. *Electronic structure of Pd clusters in the tight-binding approximation: influence of spd-hybridization.* Surface Science, **352-354** 675–679 (1996).

[153] G. Rossi, R. Ferrando and C. Mottet. *Structure and chemical ordering in CoPt nanoalloys.* Faraday Discussions, **138** 193 (2008).

[154] P. Entel and M. E. Gruner. *Large-scale ab initio simulations of binary transition metal clusters for storage media materials.* Journal of Physics Condensed Matter, **21**(6) 064228 (2009).

[155] G. Tréglia, C. Goyhenex, C. Mottet, C. Legrand and F. Ducastelle. chapter Electronic Structure of Nanoalloys: A Guide of Useful Concepts and Tools, pages 159–195. Springer-Verlag (2012).